THREE DIMENSIONAL RADIOISOTOPE IMAGING

USING GAMMA RAY COINCIDENCE SCANNING

by

STEPHEN RUDIN

A dissertation submitted to the Graduate Faculty
in Physics in partial fulfillment of the
requirements for the degree of Doctor of Philosophy,
The City University of New York.

1975

This manuscript has been read and accepted for the Graduate Faculty in Physics in satisfaction of the dissertation requirement for the degree of Doctor of Philosophy.

8/18/75
date

Chairman of Examining Committee

8/22/75
date

Executive Officer

Professor Paul N. Goodwin

Professor H. Lancman

Professor Kenneth Rubin

Professor Edward Siegel

Professor Sal J. Vacirca
Supervisory Committee

The City University of New York

ACKNOWLEDGMENTS

I should like to express my gratitude to Prof. H. E. Hart for introducing me to the problem of three dimensional coincidence scanning, for providing support for the project, and for encouraging independent effort yet being available for frequent consultations and discussions throughout the course of the work.

In addition, I wish to acknowledge the assistance of many people in the various stages of this work. Consultations with the following people at Brookhaven National Laboratories during the initial stages were appreciated: Drs. James Robertson, Bob Chase, V. Radeka, and Jim Richards. I am indebted to the late Dr. A. A. Sherman for supplying some of the equipment at the very beginning of the study. Also I thank Mr. Steve Gorchoff and Mr. Joe Kisch for assistance with the photographic processing of the figures and Mrs. Mona P. Cohen for her skill and ingenuity involving the final typescript. A special note of appreciation must go to Dr. P. A. Bardfeld of Montefiore Hospital and Medical Center for his continuing encouragement and cooperation.

Finally, it is a pleasure to thank my wife Ann for having among her enumerable virtues great patience and good humor.

TABLE OF CONTENTS

LIST OF TABLES

LIST OF FIGURES

CHAPTER I

INTRODUCTION

The aim in clinical radioisotope scanning has been to obtain diagnostic information from the distribution of radioisotopes in tissue. A gamma ray emitting isotope either in ionic form or tagged to a radiopharmaceutical is administered. Its concentration in the organ being studied forms a three dimensional distribution of radioactivity.

Although each radionuclide in the distribution may emit radiation in any direction, commonly only those gamma rays emitted in a finite solid angle about a preferred direction are detected during the course of an imaging procedure. The exact locations of the radionuclides are usually not determined. Instead, a two dimensional image approximating the projection of the three dimensional radioisotope distribution is obtained.* In Chapter II the two dimensional scan evaluation criteria of spatial resolution and statistical quality are reviewed. A description on the use of magnifying collimators in improving spatial resolution is given as an application.

In order to obtain depth information a number of views are usually taken in different directions. In brain scanning, anterior, posterior, left and right laterals, and perhaps vertex views are taken. Nevertheless small lesions can be missed in all of these views because each view may principally represent the integrated contribution of the much

* For a short review of nuclear medicine imaging instrumentation see the article by Beck (37) or for a more comprehensive source see the text edited by Gottschalk and Beck (38).

larger amount of radioisotope present in the normal background material rather than the total radioisotope (or lack of radioisotope) in the abnormal lesion. Ultimately, it would seem that optimal display of information concerning a three dimensional object requires the equivalent of a three dimensional matrix.

In Chapter III a review is presented of three dimensional or tomographic imaging techniques classified in terms of smearing, reconstructional, or direct spatial methods. In reviewing smearing methods, a summary of the present status of magnifying collimator rotational tomography is given. The review of direct spatial methods serves as a framework for Focusing Collimator Coincidence Scanning (FCCS). The overall purpose of this work is to study the physical imaging properties of this particular technique with a view to determining whether further development for clinical usage is indicated. Chapter IV summarizes the theory of FCCS. Chapter V contains the results of preliminary experiments. Chapter VI gives a general theoretical framework for evaluating three dimensional scans. Chapter VII contains the results of quantitative two probe three dimensional resolution measurements and Chapter VIII demonstrates how the results may be extrapolated to make FCCS clinically useful.

Appendices are also provided: Appendix A outlining the nuclear electronics used; Appendix B describing the construction of the computer controlled x-y scanning platform; and Appendices C and D containing more detailed analysis of mathematical properties used in the text.

CHAPTER II

TWO DIMENSIONAL SCANNING EVALUATION CRITERIA

A. Spatial Resolution in the Limit of Infinite Counts

1. Point Spread Function (PSF) and Isoresponse Curves

In the limit of infinite counts, fluctuation due to the statistical nature of nuclear counting may be neglected. The imaging properties of a system in this limit may be determined by considering the system's response to a point source at different positions within a homogeneous medium, the so-called point spread function (PSF). For a typical rectilinear scanner with a focusing multi-channel collimator the point spread function (PSF) is cylindrically symmetric around the projection or longitudinal direction. In addition, it is characteristically slowly varying in the longitudinal direction and relatively rapidly varying in the transverse directions. That is to say, as a point source is moved away from the focal point of the collimator the count rate decreases much more rapidly for displacements transversally than for those longitudinally. If one were to connect points of equal response in the field of view of the collimator one would get a family of isoresponse curves such as appears in Fig. 1. In designing a scanning system the width of the PSF may be optimally chosen to match the lesion to be detected (1).

2. Modulation Transfer Function (MTF)

Another complete characterization of the resolution response of a scanning system can be obtained by considering the two dimensional projection of the three dimensional radioisotope distribution to be an

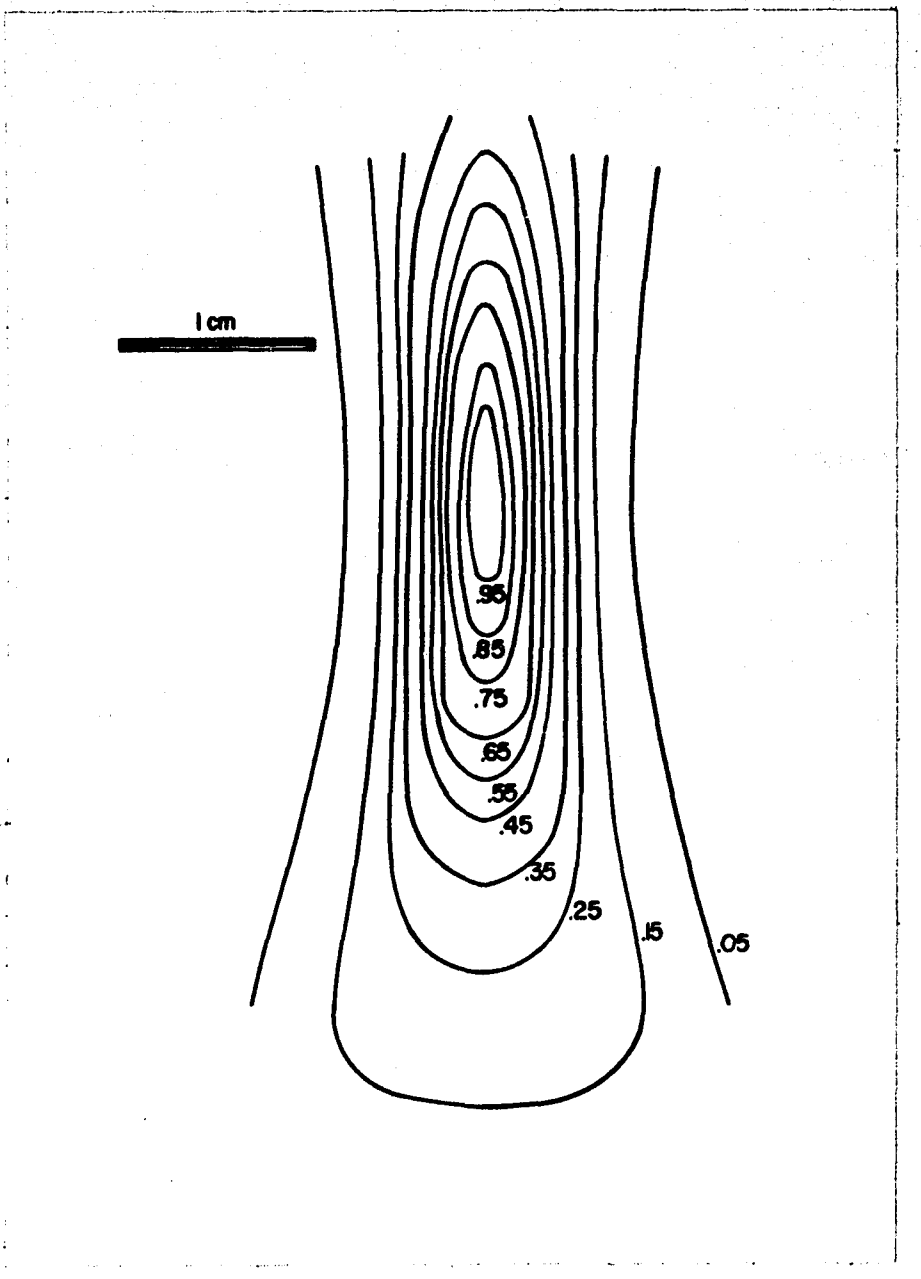

Figure 1. Isoresponse curves for a point source. The collimator would be some distance away toward the top of the figure with collimator channels focused down toward the 95% region.

infinite vector space, where the basis set of orthonormal functions is the set of sinusoidally varying spatial functions, B_2.

$$B_2 = \left\{ \exp(i\,\omega_x x),\ \exp(i\,\omega_y y) \right\} \tag{2.1}$$

Thus all images are made up of linear combinations of these functions. The spatial frequency response of the system can be shown to provide a complete measure of the spatial resolution of the system. Since all spatial frequencies are equally represented within a point source, the fourier transform of the point spread function describes how well each spatial frequency is detected. This frequency response is called the modulation transfer function (MTF).

$$MTF(\omega_x,\omega_y) = \int_{-\infty}^{\infty}\int_{-\infty}^{\infty} dx\,dy\,PSF(x,y)\exp\left[i(\omega_x x+\omega_y y)\right] \ . \tag{2.2}$$

If the PSF is circularly symmetric as is the case for most rectilinear scanners, then for spatial frequencies, ω, in any single direction, MTF (ω) is the same as MTF $(\omega_x, 0)$ and equations (2.3) hold:

$$\begin{aligned} MTF\ (\omega) &= MTF\ (\omega_x,0) \\ &= \int_{-\infty}^{\infty} dx \left[\int_{-\infty}^{\infty} dy\,PSF(x,y) \right] \exp(i\omega_x x) \\ &= \int_{-\infty}^{\infty} dx\ \ LSF(x)\ \exp(i\omega_x x), \end{aligned} \tag{2.3}$$

where

$$LSF(x) = \int_{-\infty}^{\infty} dy\ PSF(x,y). \tag{2.3a}$$

LSF is the line spread function. For this special case of circular symmetry, it is often experimentally more convenient to measure the LSF which then completely determines the resolution characteristics. It is easy to show for this case that if either PSF, LSF, or MTF is known then the other two can be derived (2).

If the PSF is not symmetric then theoretically the LSFs for all directions in the plane would have to be found in order to get a complete set of non-orthonormal functions.

3. Factors Affecting Spatial Resolution

For nuclear medical imaging devices the spatial resolution can be considered to be made up of four sets of factors: a) collimator-geometric parameters, b) collimator-septal-penetration parameters, c) scattering characteristics of the tissue and collimator, and d) the intrinsic system parameters. The first three sets of parameters have been discussed extensively by Beck (2-5). The collimator-geometric parameters such as thickness, channel diameter and for the rectilinear scanner, focal distance have an obvious effect on resolution. Collimator penetration or transmission of radiation through the collimator septa clearly reduces the resolution. The effect obviously becomes more important, the higher the gamma ray energy. The effect of scatter is a complicated effect depending upon gamma ray energy, scattering material and the geometry of the source with respect to the detector. Finally, the intrinsic resolution parameters pertain to the crystal detector and associated electronics. The intrinsic resolution plays no essential role in limiting the spatial resolution of a rectilinear scanner. For a gamma camera, however, the spatial resolution of the system is significantly

effected by the intrinsic resolution.

B. Magnifying Collimators

In order to illustrate the importance of intrinsic resolution in gamma camera performance, consider the effect of a slightly focused or converging collimator (6). In Fig. 2B, if r is the distance between two barely resolvable point sources, then by using a converging collimator as in Fig. 2A, the image is magnified and the two points may now be easily resolved. Conversely, a diverging collimator, although having a larger viewing field, would adversely effect the resolution, Fig. 2C. If the LSF is assumed to be gaussian for the sake of analytic simplicity as in Eq. (2.4), then Eq. (2.5) can be derived using Eq. (2.3).

$$LSF(x) = \frac{1}{4\pi r_{PM}} \exp - \left[x^2/r^2_{PM} \right] \tag{2.4}$$

$$R_M = \frac{MTF(\omega/M)}{MTF\ (\omega)} = \exp \left[(\omega^2 r^2_{PM}/4)(1-1/M^2) \right] \tag{2.5}$$

In the above equations r_{PM} is a resolution width characteristic of the intrinsic blurring due to the photomultiplier tube and associated circuitry, ω is 2π times the spatial frequency, M is the magnification factor and R_M is the ratio of the MTFs with and without magnification. It is clear from Eq. (2.5) that magnification improves the intrinsic resolution by reducing the effect of the fixed optical, statistical and electronic blurring of the gamma ray camera. For a small magnification

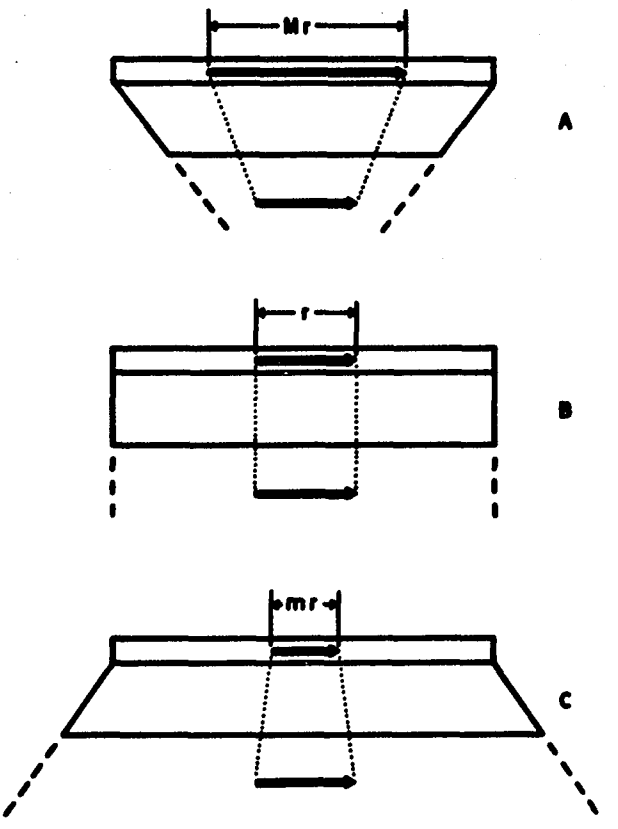

Figure 2. Comparison of A) magnifying, B) parallel-channeled and C) diverging gamma camera collimators in imaging sources separated by a distance r. M is the magnification factor and m is the minification factor.

Eq. (2.5) reduces to equation (2.5a).

$$R_M = \exp\left[(\omega^2 r_{PM}^2/2)(M-1)\right] \qquad (2.5a)$$

The MTF then improves exponentially with magnification and spatial frequency squared. Figure 3 shows the clinical result of the use of a magnifying collimator in improving the detectability of lesions.

C. The Effect of Finite Counts - Information Density

In order for a radioisotope scan to have clinical usefulness the contrast variations representing organ structure must not be overly blurred by the statistical fluctuations characteristic of counting nuclear events. Thus if N is the background counts collected per unit of area or the "information density" and it is required that a contrast change of P percent be detected with a high degree of probabilty, then the statistical fluctuation in N, i.e. $\sqrt{N}$, must be a few times less than (0.01) PN depending upon the degree of certainty required (7). In order to be able to detect finer gradations of contrast, the information density or ID must be increased. For a rectilinear scanner which moves in a raster-like pattern the ID equals (count rate) / [(line spacing) x (speed)] . For typical ^{99m}Tc lung or liver scans a maximum ID of 2500 counts/cm^2 is obtained where the picture element size (line spacing multiplied by collection distance along the scan line) is about 3mm^2. For a device with ten film density gradations or ten colors, the above ID represents a standard deviation of greater than one density gradation or one color per picture element.

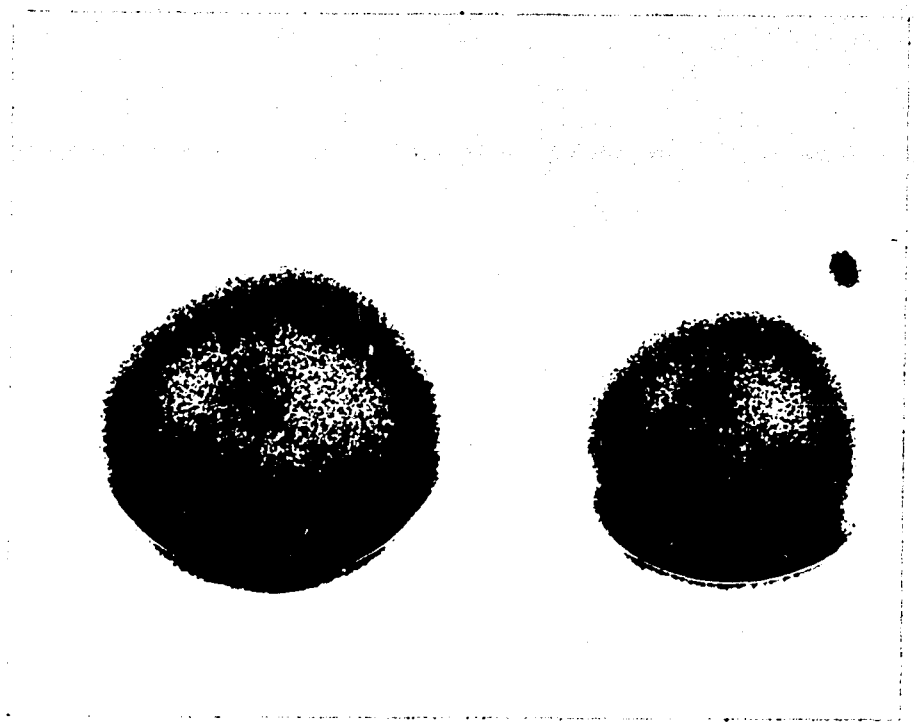

Figure 3. Comparison of clinical brain scans done with a magnifying collimator (enlarged image) and a parallel-channeled collimator (6).

CHAPTER III

REVIEW OF TOMOGRAPHIC IMAGING TECHNIQUES

The ideal display of image information about a three dimensional source or object must be a three dimensional image. In the past many methods have been tried in order to image successive slices of the object or patient being examined. This field is commonly referred to as tomography. In this work, the terms tomography and three dimensional imaging are used synonomously.

Some of the radioisotope techniques involving image smearing are similar in principle to tomographic radiological techniques.* These methods have had only limited effectiveness. The very recently developed reconstructional techniques of radiology are still experimental so far as their use in nuclear medicine. The least developed technique up until recently has been the direct spatial methods. A review of the above three dimensional imaging techniques follows.

A. Smearing Techniques

Common to all smearing techniques is the characteristic that no information received by the detector system from all slices in the source is rejected initially. Many of the smearing technqiues are similar to standard tomographic x-ray techniques where the x-ray source, patient, and film or detector are moved in precise relation to one another either in a linear, circular or more complicated hypocycloidal motion. In this process the image of only one source plane remains in one to one correspondence throughout the motion, but the images of all other planes are smeared

*For a brief review of these techniques see the Introduction in the book Tomographic Imaging in Nuclear Medicine (8-11).

or blurred, This blurred information, however, does contribute to the noise level above which the signal from the focal plane must appear.

1. Rotational Tomography

Figure 4 illustrates the geometry of tomography using circular smearing. In rotational tomography, a straight bore parallel channel collimator is used where the channels are all slanted of the order of 20^{o} with respect to the axis of the gamma camera crystal. In the beginning of the scan source points 1, 3 and 2, 4 map onto points 1 and 2 on the crystal respectively. As the scan proceeds the collimator is rotated and the source is translated circularly so that there is always a one-to-one correspondence between points 1 and 2 of the source with 1 and 2 of the image. For example, at the rotation angle of 180^{o} indicated by dotted lines in Fig. 4, points 1 and 2 in the focal plane are still mapped onto 1 and 2 of the image; however, source points 3 and 4 out of the focal plane are smeared into a circular image.

There are several disadvantages with this method and clinical evaluation has not been favorable (8).

(a) Reverse artifacts or ghosts can appear on image planes above or below planes where there are hot or cold spots (9).

(b) Noise due to counts from off focal sources can obscure details of the focal plane image.

(c) The method strictly speaking exhibits differences in transverse resolution as a function of longitudinal depth rather than exhibiting true longitudinal spatial resolution. This can be seen easily by the fact that the depth of a uniform plane surface source whose normal is in the longitudinal or Z direction, cannot be determined.

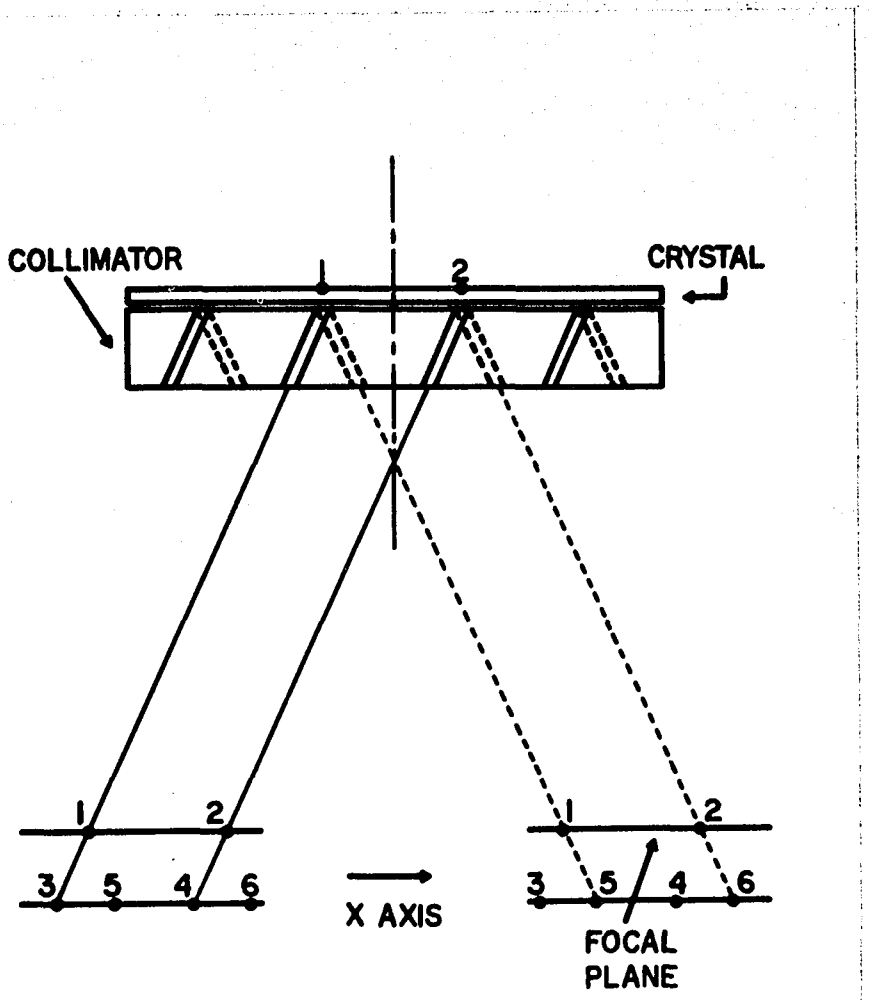

Figure 4. Rotational tomography using an angled parallel channeled collimator and a gamma camera. For both the two rotational positions 180^{o} apart represented by dark and dotted lines respectively, only points 1 and 2 in the focal plane are imaged onto points 1 and 2 on the crystal.

The counts recorded from such a planar source are independent of depth (3).

(d) Finally, the method which uses a standard gamma camera as a detector and a multi-hole collimator exhibits those limitations of the non-tomographic scanning devices associated with intrinsic blurring, geometric parameters, septal penetration and scatter in the medium.

2. Analogous X-ray Radiographic Tomographic Methods - Tomoscanner

In order to reduce the artifacts in rotational tomography, more complicated motion smearing has been suggested. Elliptical, hypocycloidal and spiral smearing has been proposed. None of these has been tried successfully with the gamma camera because of the massive electromechanical housings required to follow these motions; however, the Anger tomoscanner approaches disc tomography (9). For this device a focusing collimator is used where the focal point is approximately centered in the organ of interest as with conventional non-tomographic rectilinear scanners. However, the detector head is a modified gamma camera with decreased position detection capability. As the scanner head moves in a rectilinear fashion the event position as well as the scanner position are recorded. A computer is then used to reposition the events so that information from one plane of a given depth remains in focus while all others are smeared. Since the collimator has channels with all angles of inclination between the most angulated channels nearest the sides of the collimator, disc tomography is approached. Although the first disadvantage of rotational tomography is thus overcome, the remaining difficulties still remain. In addition, the intrinsic resolution of the

tomoscanner crystal and electronics is probably worse than that of a conventional camera, since a smaller diameter crystal and fewer photomultiplier tubes are used.

3. *Magnifying Rotational Tomography*

We have suggested a modification of rotational tomography, Fig. 5, which decreases the limitation of intrinsic gamma camera resolution yet which may not have the artifact problems of parallel channel rotational tomography (10). This technique requires the use of a focusing or magnifying collimator whose focal point is beyond the patient at a distance depending upon the magnification required. The collimator rotates while the patient is translated in a circle or more complicated pattern in which case a computer would be used to reposition and superimpose the images for various rotational angles. The result of this technique is an image which is magnified at the crystal thus effectively improving intrinsic resolution just as in the non-tomographic technique of Chapter II, Part B. In addition, the channel inclination angles sampled in order to form an image, cover a wide range (depending upon the magnification) and thus reduce the possibility of the artifacts which occur when only the one channel inclination angle of parallel channel rotational tomography is used.

4. Zone Plate Cameras

The zone plate or, in general, coded aperture camera is a smearing technique which does not require motion of the patient or detector. A special collimator with no channels, but instead a pattern such as a Fresnel zone plate (11) is used. An incoherent hologram is

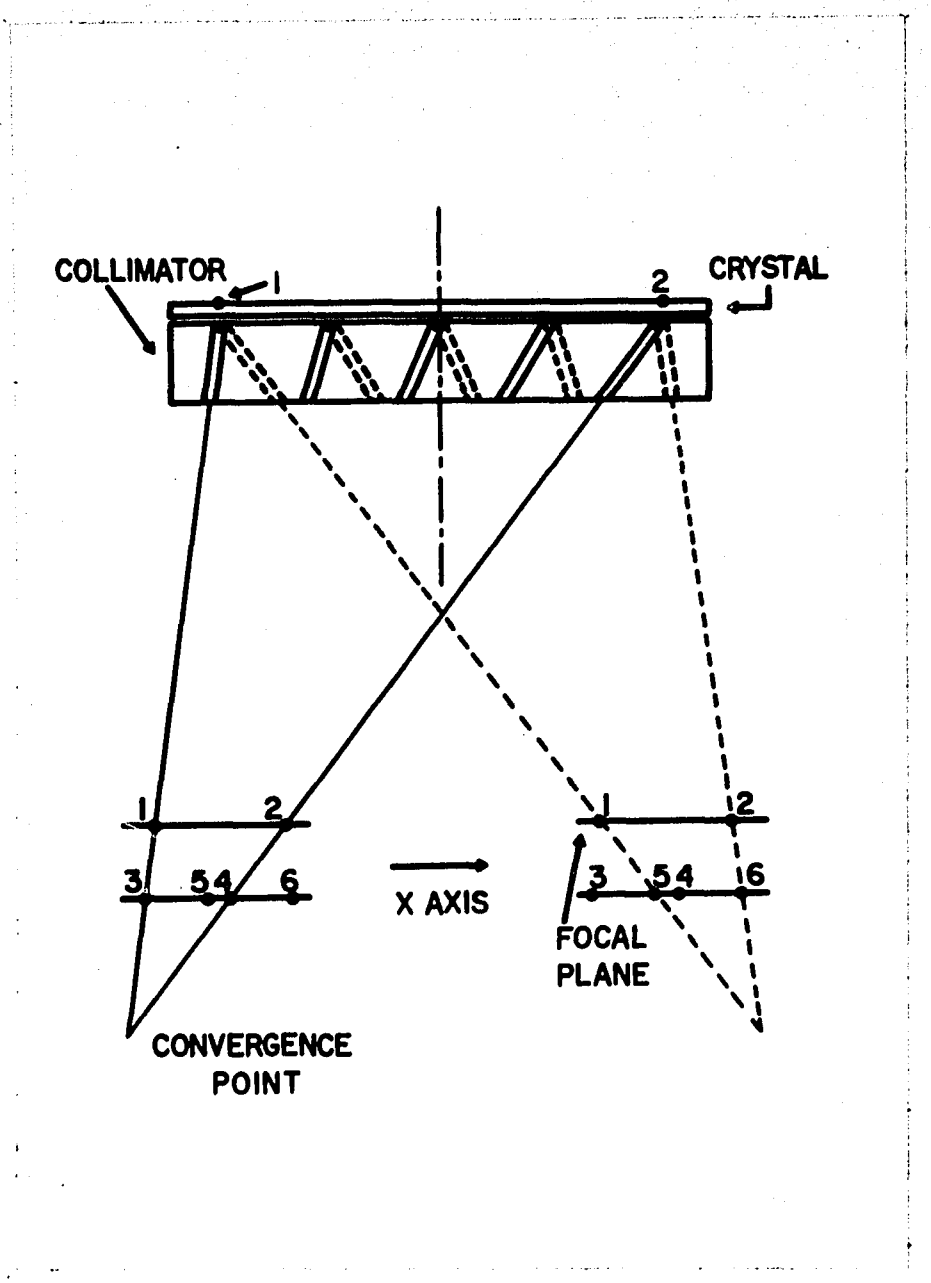

Figure 5. Magnifying rotational tomography using an angled focusing collimator. The same as Fig. 4 except that the image is magnified at the crystal thus reducing the effect of intrinsic camera blurring.

produced by the gamma rays from the radioisotope distribution passing through the coded aperture. This hologram is recorded either on x-ray film after intensification or by a gamma camera. Finally an optical system perhaps employing a laser is used to reconstitute the image. The potential advantages of this system are (i) the collimater sensitivity is much greater than conventional multi-hole camera collimators and (ii) the hologram contains supposedly inherently tomographic information because the greater the source depth the larger will be the coded aperture's shadow. The disadvantages of the method, however, are many. (a) Although no motion artifacts are involved, there are other artifacts and ghosts depending upon the coded aperture. (b) Noise is a major problem and limits the size of the organ to be imaged. Only small organs such as the thyroid have been successfully imaged in clinical trials of this type of device. (c) The technique cannot image a uniform plane surface source whose normal is in the longitudinal Z direction; therefore, the inherent tomographic capabilities of the method are questionable. (d) Collimator and camera characteristics are limiting factors. The effects of scatter in the medium and penetration of the aperture have not been fully worked out and might be significant considering the fact that no energy selection is used in some of these devices. Also, the use of camera detectors introduces the intrinsic resolution limitation onto the formation of the hologram images where fine detail is essential. To get around this difficulty, x-ray film with intensifying screens have been used; however, lack of sensitivity of the film-screen combination then becomes a problem. In general, coded aperture cameras have had very

limited success in standard projection scanning and almost none in tomographic scanning.

B. Reconstructional Methods

For both the section scanning and positron camera techniques considered here, a computer is used to reconstruct the image from recorded events. With the great success of the EMI device (15) and similar x-ray transmission section scanning devices in diagnostic radiology the reconstructional approach holds good promise for application in nuclear medicine.

Certain fundamental difficulties, however, remain in applying this method to radioisotope emission scanning.

1. Section Scanning

In section scanning a series of scans are taken transverse to the body axis at various angles using either a gamma camera (12) or a rectilinear scanner (13, 14). Each of these scans represents a projection of the source at each angle. By using these projections as the raw data the activity concentrations in the source can be reconstructed using a computer just as for the transmission devices such as for the EMI scanner (15) the series of transmission scans at various angles can be used to reconstruct the tissue density variations within a slice in the patient.

The section scanning technique may be considered in terms of the four sets of difficulties found with the smearing techniques of the previous section. (a) Motion artifacts should not occur unless there is patient movement; however, (b) computer artifacts and noise can be generated by the reconstructional technique depending upon which one is

used (12, 16). (c) The method, however, is undeniably tomographic in nature since a viewing slice in space is selected even before data is recorded. The depth of a plane surface source whose normal is in the longitudinal Z direction can easily be determined by section scanning techniques. (d) The difficulties characterizing standard nuclear imaging devices also are true of section scanning since these devices are exactly the ones that have been used to obtain the raw data for the technique.

The combination of (b) computer created noise and (d) the inability of standard nuclear imaging devices to obtain adequate spatial resolution and statistics are then the main difficulties with section scanning at this point in time. The technique is actively being researched and some of these limitations may be eventually overcome or surmounted with the use of higher activities of short-lived radioisotopes, faster gamma imaging devices and better reconstructional computer programs.

2. Positron Cameras

One way to neutralize the effect of attenuation in the source upon images is to use positron annhilation radiation. If two gamma cameras are placed on opposite sides of a source then the path connecting two coincident events occuring on both cameras must also go through the source of the annhilation radiation. A computer can then be used to reconstruct the collection of these lines into an image of the source. Although the raw data is independent of attenuation in the source, the information inherently is limited in tomographic value because the source

of two annhilation gamma rays could have been located anywhere along the line determined by the two scintillations. In addition, the high incidence of false coincidences due to slow camera electronics and poor efficiency for detecting 0.511 MeV gamma rays has resulted in positron cameras with constricted areas of detection (17) and hence less tomographic character. A recent development has been the possible use of a positron camera as the imaging device in section scanning (16,18-21). For such a device the tomographic effect would be achieved by rotating after successive projections are taken and because positron annhilation radiation only is being considered there need be no attenuation correction difficulties.

C. Direct Spatial Techniques

In the direct spatial techniques mentioned below, source-location information (in three dimensions) is based upon a process either involving coincident multi-gamma emissions or an x-ray absorption and emission which enables the direct determination of the source position in space.

1. Positron Time-Of-Flight

When positron annhilation occurs, two 0.511 MeV gamma rays are emitted in almost opposite directions. If two detectors on either side of the source could detect not only the position of the emitted gamma ray as it strikes the detector but also the exact time, then the location of the source could be found. The time difference between the detected events would determine just where along the line of the two gamma rays the source had to be. In order to get a depth resolution of 1 cm, however, the timing circuits would have to be capable of

resolving events separated by 300 ps in time. Such resolve times can be achieved using plastic and perhaps semi-conductor detectors; however, the energy resolution and/or efficiency of these detectors is deficient. Some attempts are being made in pursuing this method (22); however, the severe instrumentation limitations may not be easy to overcome.

2. Fluorescent Excitation

If a narrow beam of x-rays or gamma rays of sufficient energy are sent into an object containing an element whose absorption edge is just below the energy of the impinging radiation, the likelihood that such radiation will be absorbed photoelectrically will be high. The atom having undergone this absorption will then almost immediately emit a characteristic x-ray. If a detector with a narrow field of view is used then any detected x-rays must have come from the intersection of the detector's field of view with the path of the exciting radiation. This is indicated schematically in Fig. 6. The intensity of the radiation detected would give an indication of the amount of fluorescent atoms in the focal region. The method is being tried clinically in thyroid scanning with iodine as the fluorescent agent (23, 24).

The difficulties with the method are (i) the low geometric efficiency in detecting homogeneously fluorescent x-rays, (ii) attenuation in tissue especially for low energy gamma and x-rays, (iii) scatter in the patient indicating the need for high energy resolution semiconductor detectors, (iv) difficulty in safely attaining high enough concentrations of fluorescent material in the organ to be imaged; and

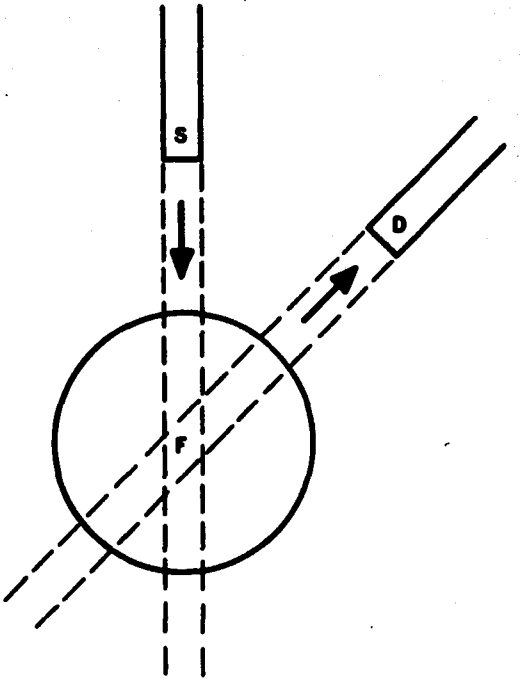

Figure 6. Fluorescent excitation scanning where S is an external x or gamma ray source and D is a high resolution detector. The intersection of the fields of view of S and D is a focal region F located in three dimensions whose content of fluorescent tracer is being measured.

therefore, (v) poor counting statistics.

3. Multi-Gamma Coincidence Techniques

In both methods described below use is made of specially selected isotopes which emit two or more gamma ryas at virtually the same time. For these isotopes there is some angular correlation between the relative directions of emissions of the gamma rays and their probability for emission. This angular dependence, however, is weak for isotopes considered below,* hence is neglected here.

a. Focusing Collimator Coincidence Scanning (FCCS)

In the coincidence method first proposed (25), Focusing Collimator Coincidence Scanning (FCCS), the multi-gamma emissions from the source are recorded as coincidences by detectors with collimators whose channels are all focused on a region within the source. The coincidence requirement that two or more gamma rays emitted at an angle be recorded simultaneously rejects gamma rays coming from sources outside the focal region. The focal region is then moved around the source volume and the count rate at each location gives a measure of the amount of activity, and thus a three dimensional image of the source activity distribution.

A significant theoretical advantage of this direct spatial technique is that a "cold" lesion can be detected within a three dimensional background region of "warm" radioacitvity just as well as can a "hot" region with activity concentration of twice the background. The potential for use in the three dimensional detection of cold lesions is apparent.

* Less than 10% for ^{75}Se whose main coincidence emissions have a $(1 + 3/51 \cos^2\theta)$ dependence as calculated using appropriate Clebsch-Gordon coefficients.

This method is the one used primarily in this work and will be further analysed in the following sections.

b. Multi-Gamma Coincidence Camera

In the coincidence camera method more recently proposed (26, 27) two standard parallel collimator channeled gamma cameras at right angles to one another register only the scintillation positions of coincident events as indicated in Fig. 7. The location of the source in three dimensions is then presumed to be at the intersection of the field of views of the channels nearest the two scintillations. Since all parts of the source are viewed at the same time there is a potential advantage over the focusing collimator (FCCS) method that dynamic studies can be taken.

The method, however, has many deficiencies. (i) Although all parts of the field are viewed simultaneously, each source volume is viewed by only a small solid angle. Since the coincident gamma ray emissions come off at any possible angle, the probability of detecting both gamma rays in two very small solid angle fields of view is exceedingly small, perhaps six or more orders of magnitude smaller than for FCCS where all channels view the same focal region. Thus, (ii) the sensitivity of the coincidence camera is poor. (iii) The fact that all points in the source are viewed simultaneously can be a significant noise problem. Since scattered gamma rays from all parts of the source will be detected as acceptable true coincidences unless energy spectrum analysis is extremely vigorous, tomographic resolution will be degraded. (iv) Gamma cameras have significantly larger resolve times

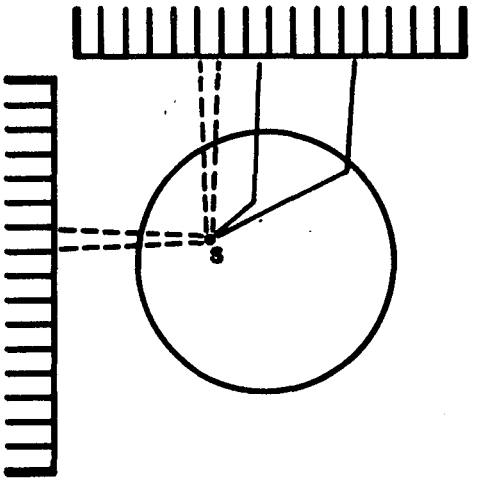

Figure 7. Coincident gamma camera technique where two cameras are placed at 90^{o} around a phantom containing a multi-gamma ray emitting radioisotope. Since the gamma rays are emitted in all directions the efficiency for detecting a given source S is very small since it is proportional to the product of the two very small solid angles represented by dashed lines. In addition, scattered gamma rays represented by solid lines can easily be counted as true coincidences thus obscuring the localization of the source.

than the simpler rectilinear scanner detectors; hence, the false or chance coincidence rate for the coincidence camera system will result in signal to noise difficulties.

CHAPTER IV

THEORY OF FOCUSING COLLIMATOR COINCIDENCE SCANNING (FCCS)

In this chapter two complementary methods for analysing FCCS due to Hart (28) are presented. The first deals with direct consideration of the PSF isoresponse curves. This method although exact in theory requires significant numerical calculation to obtain results. The other method is a simplified model which gives useful insight into FCCS and at the same time allows for rapid evaluation of the system sensitivity and resolution.

A. PSF and Isoresponse Curves

Isoresponse curves for a gamma ray emitting point source represent the relative probability that the gamma ray will be detected for a given position in the field of view. If, as in FCCS, two or more gamma rays must be detected at the same time in order for an event to be registered, then for a single focusing collimator detector and for two similar energy gamma emissions, the FCCS isoresponse curves will be the square of the single gamma isoresponse curves. This was first experimentally verified by Hart and co-workers (28, 29) using a ^{125}I point source. The result of squaring the isoresponse curves is that the corresponding new FCCS curves are much narrower, and thus spatial resolution is improved not only transversally but longitudinally. When multiple detectors, scattering material, and various energy gamma emitters are used in a more practical FCCS system, this description of the system response, although exact, becomes complicated, requiring three dimensional numerical computations in order to determine the PSF isoresponse curves in space.

B. Hart's Model for FCCS

1. Assumptions

A detailed discussion of Hart's simplified model for FCCS appears elsewhere (28, 30) so that only the application of the model to the two crossed-probe experiment used primarily in the work will be reviewed here. The basic assumption is that the field of view or penumbra of each collimator channel can be divided into two volume regions as illustrated in Fig. 8: a) the focal region of volume α common to all con-focal collimator channels and b) the off-focal or single channel volume ν which is the volume of intersection of the channel penumbra with the source volume exclusive of α. Furthermore, it is assumed that any two channels interact only in region α. It is clear that this assumption is inapplicable for two adjacent channels on a collimator. But if the further restriction is made that only channels approximately 90^{o} from each other can contribute to a valid coincident event, the region of overlap of the two channels becomes minimal and approaches α. If a dual gamma ray emitter is considered, the above assumption of 90^{o} relative channel angle is well approximated for a two probe detector such as the one illustrated in Fig. 9, if both probes are required to trigger for a valid coincident event. In this figure only three channels per probe are indicated whereas in reality the collimators used in this study have up to 1507 channels. In either case the assumption of separate focal and off-focal regions becomes quite reasonable if it is required that both probes fire. An additional assumption will be made here which simplifies the review of the theoretical formulation below. That assumption is that $\alpha \ll \nu$.

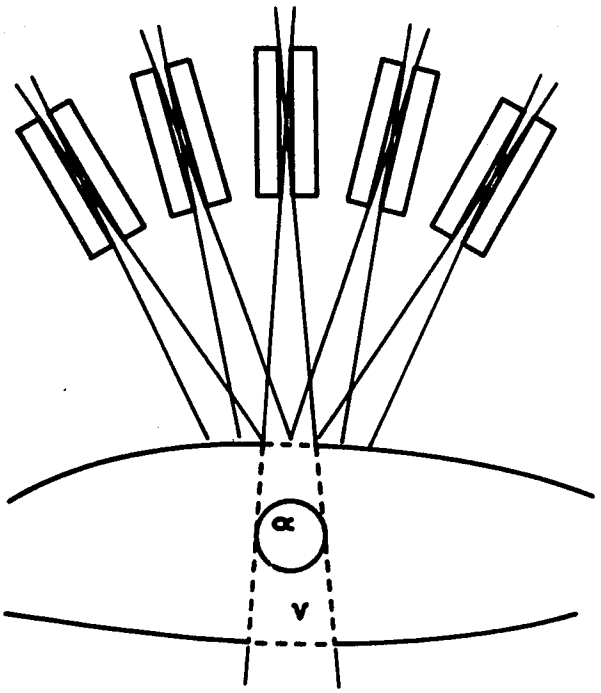

Figure 8. Illustration of the basic assumption in the Hart's theory of FCCS. The intersection of the field of view of a collimator channel with the source volume in the simplified theory of FCCS, divided into a focal region α , and an off-focal region or single channel volume, V .

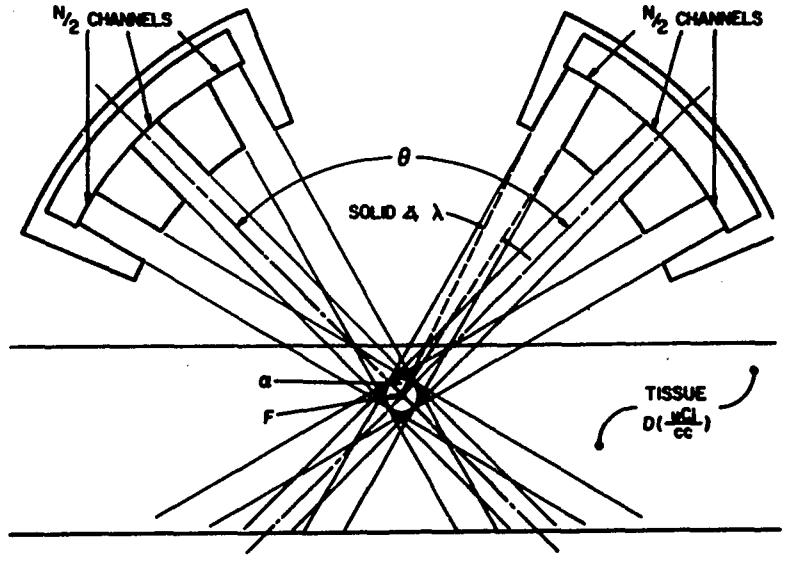

Figure 9. A two probe FCCS system, each collimator having N/2 channels and focused at point F in the focal volume α. The axes of the two probes are separated by angle θ. The isotope concentration in the patient is D.

This is again a plausible assumption considering Fig. 9 where there is a reasonably thick source compared to the longitudinal dimensions of the focal region α . Finally it is convenient to assume for later use that N/2, the number of channels in each collimator is sufficiently large so that $N\alpha \gg \nu$. The significance of this assumption will be discussed below.

2. Theoretical Formulation

Table 1 gives the definitions of terms and relevant equivalences. It can be seen that because of the assumption that $\alpha \ll \nu$, the total focal single gamma count rate γ_2 is significantly less than the total off-focal single gamma count rate, γ_1 . Thus most of the single gamma signal comes from outside the focal region.

$$\gamma_2 \ll \gamma_1 \tag{4.1}$$

On the other hand because $N\alpha \gg \nu$ was assumed in Chapter IV, Part B.1, Eq. (4.2) holds, where μ_2 is the focal coincidence rate and μ_1 is the off-focal coincidence rate.

$$\mu_2 \gg \mu_1 \tag{4.2}$$

The assumption $N\alpha \gg \nu$ thus implies that most of the coincident gamma signal will come from the focal region compared to that from outside the focal region. In fact, in counting coincident events the significant noise is not μ_1, but the chance or statistical coincidences due to the finite resolve time, τ , of the coincidence detection circuitry. If this chance coincidence rate or noise is called C_c ,

TABLE 1

DEFINITION OF TERMS FOR FCCS

Terms	Equivalences	Definitions
$N/2$		= number of channels per collimator
e_o =	λ	= efficiency of each channel
e_1 =	$(N/2)\lambda$	= collimator efficiency
D		= source concentration in activity per volume
α		= focal volume
d_1 =	$D\alpha$	= activity in focal volume
υ		= single channel volume field of view in source
d_o =	$D(N/2)\upsilon$	= activity in collimator field of view
$\gamma_2 = e_1 d_1$	$= (N\lambda)D\alpha$	= in-focal single gamma count rate
$\gamma_1 = e_o d_o$	$= (\lambda)DN\upsilon$	= off-focal single gamma count rate
$\mu_2 = e_1^2 d_1$	$= (N\lambda)^2 D\alpha$	= in-focal coincidence count rate
$\mu_1 = e_o^2 d_o$	$= \lambda^2 DN\upsilon$	= off-focal coincidence count rate
$C_c = 2\tau\gamma_1^2$		= chance coincidence rate

then Eq. (4.3) holds.

$$C_c = 2\tau\nu_1^2 \tag{4.3}$$

It is assumed temporarily that the single gamma count rate ν_1 in each detector is the same; however, this assumption can easily be discarded with slight modifications to Eq. (4.3) and some of the other equations in this section.

3. Evaluation Criteria

The simplified model may now be used to evaluate FCCS in terms of the smallest detectable lesion defined as equivalent to volume $\beta_{\gamma 2}$ within the focal region, and in terms of the comparison between the lesion detectability of FCCS with standard single gamma ray scanning. If $\beta_{\gamma 1}$ is the equivalent volume of the smallest detectable lesion using single gamma ray counting, then the relative lesion detectability, r.l.d., is the ratio $\beta_{\gamma 1}/\beta_{\gamma 2}$. The smallest detectable lesion volumes and hence collimator design parameters are determined by the requirement that the lesion signal be greater than 3 times the standard deviation of the background count signal (1). Formally, this determination of $\beta_{\gamma 1}$ and $\beta_{\gamma 2}$ is given, greatly simplified, in equations (4.4) and (4.5):

$$\nu_2 \frac{\beta_{\gamma 1}}{\alpha} t_1 > 3\sqrt{\nu_1 t_1} \quad , \tag{4.4}$$

and

$$\mu_2 \frac{\beta_{\gamma 2}}{\alpha} t_2 > 3\sqrt{2\tau\nu_1^2 t_2} \quad , \tag{4.5}$$

where t_1 and t_2 are counting times for single gamma and coincident gamma counting. A more complete discussion of this analysis appears elsewhere (28, 30) and only a review of the results is attempted here.

It should be noted first, however, that lesions $\beta_{\gamma 1}$ and $\beta_{\gamma 2}$ coulIt should be noted first, however, that lesions $\beta_{\gamma 1}$ and $\beta_{\gamma 2}$old" lesions) as they could regions of increased activity ("hot" lesions). In such a case $\nu_2 \frac{\beta_{\gamma 1}}{\alpha} t_1$ and $\mu_2 \frac{\beta_{\gamma 2}}{\alpha} t_2$ would represent the decrease in counts collected over the "cold" lesion for single gamma and coincident gamma counting respectively.

If r.l.d. < 1, then smaller lesions can be detected using standard scanning; the FCCS system would not be worth using. It turns out (30) that if a uniform source with no boundary or other inhomogeneities is assumed to be used with scanners such as those of this work, then the r.l.d. is close to 1 and FCCS has no advantage over standard single gamma ray scanning. All real sources, however, have inhomogeneities of some sort and if only a small (5%) non-uniformity is assumed, then, although Eq. (4.5) does not change significantly, Eq. (4.4a) is now valid for single gamma counting where the new term due to the 5% inhomogeneity is dominant.

$$\nu_2 \frac{\beta_{\gamma 1}}{\alpha} t_1 > 3\left[\nu_1 t_1 + (.05)^2 (\nu_1 t_1)^2\right]^{\frac{1}{2}} \qquad (4.4a)$$

For this new $\beta_{\gamma 1}$, the new $\text{r.l.d.}_{(.05)}$ can be orders of magnitude greater than 1(30).

CHAPTER V

FCCS PRELIMINARY EXPERIMENTS: TWO CROSSED PROBES

A. Isotope and Probe Assembly

The isotope used in this experiment was ^{75}Se which has a few sets of gamma rays emitted in coincidence. Table 2 and Fig. 10 indicate that the energies of these coincident gamma rays fall into two ranges: 97 to 136 keV and 265 to 280 keV (31). In addition, there is a 401 keV gamma ray at the sum of these ranges. There are also other coincident and non-coincident emissions which are not of interest. Since ^{75}Se has a 120 day half-life and is readily available it is the most convenient isotope to use in laboratory and phantom studies of FCCS. The isotope ^{125}I was used in the original experiments (28, 29), but was not chosen for this work because its low energy gamma rays are too easily attenuated in tissue.

Each probe used in this work consisted of a 1 in thick cylindrical lead housing containing a 5 in diameter, 2 in thick Harshaw Co. NaI (Tl) crystal, an RCA 4525 bialkali photomultiplier tube and a 5 in diameter 2.5 in thick 1507 channel lead collimator (32) made at Brookhaven National Laboratory (BNL).*

The single gamma isoresponse curves for a point source in air (Fig. 1) were determined by moving a 3μCi ^{75}Se point source (one millimeter in diameter) in the collimator field of view.

Actually two families of isoresponse surfaces were obtained, one

* The collimators were suppled by Powell Richards of Brookhaven National Laboratory.

TABLE 2

GAMMA SPECTRUM FOR ^{75}Se

Radiation	%/disintigration	Energy (MeV)
Gamma-7	58.6	0.2646
Gamma-5	55.5	0.1359
Gamma-8	25.2	0.2795
Gamma-4	16.4	0.1211
Gamma-10	13.0	0.4005
Gamma-3	3.1	0.0967
Gamma-9	1.4	0.3037

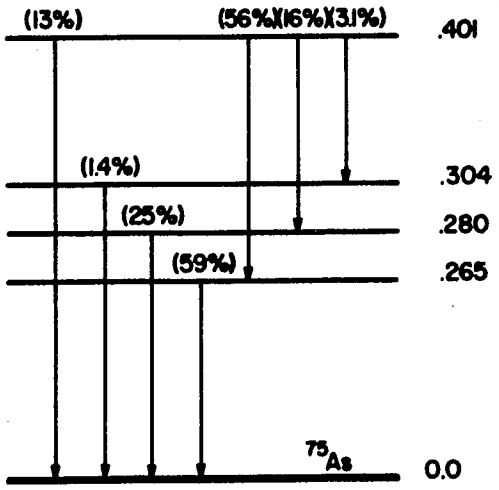

Figure 10. Decay scheme of ^{75}Se showing isomeric states of ^{75m}As. Note that here and in Table 2 not all transitions are indicated, only the most significant.

for each energy range of gamma emission; however, these families differed significantly only for isoresponse surfaces of less than 5%.

B. Scanning Geometry

The two identical probes were set up in the geometry illustrated in Fig. 11. The X axis is along the transverse direction perpendicular to both probe axes; the Z axis is along the longitudinal direction defined by the angle bisector of the two collimator axes; and the Y axis is along the other transverse direction (i.e. the Y axis lies in the plane defined by the probe axes).

C. Coincidence Detection Electronics

The configuration of the detection electronics was upgraded a number of times throughout this work. These configurations are described in order of increasing complexity in Appendix A. For the initial experiments each probe was allowed to register gamma rays in only one of the ^{75}Se energy ranges centered approximately about 130 and 265 keV. In later configurations a factor of two in increased sensitivity was gained by allowing both probes to register for either energy range as long as both probes fired in coincidence.

The resolve time, γ , for the initial configuration was about 50 ns. For later circuitry the resolve time was reduced to between 10 and 20 ns. Cross-over and fast-slow, leading edge and constant fraction timing techniques were used at various times in the work as described in Appendix A. An attempt was made to improve the resolve time even further by using fast rise time plastic and liquid scintillators doped with lead for improved sensitivity; however, both

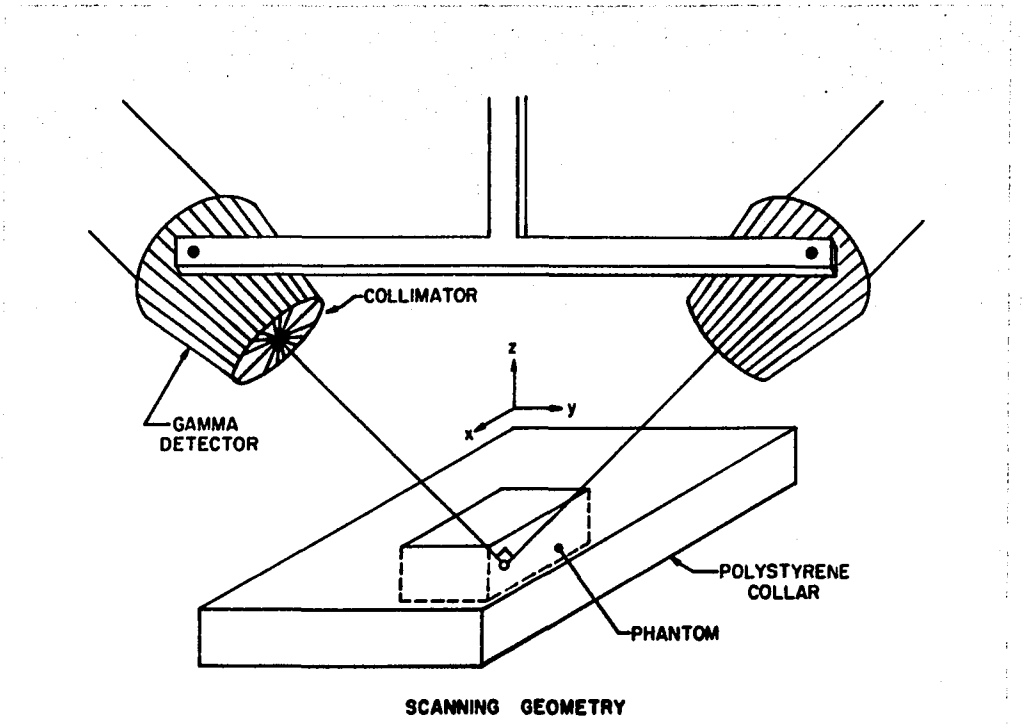

Figure 11. Coincidence scanning geometry where Z is longitudinal and X and Y are transverse scanning directions. The Z direction is the collimator axes angle bisector; the X direction is perpendicular to both collimator axes; and the Y direction is in the plane parallel to both collimator axes. The polystyrene collar around the phantom helps make attenuation more uniform.

the lack of energy resolution and sensitivity compared to the standard NaI (Tl) scintillators made these initial efforts unrewarding.

D. Scanning Platform, Data Acquisition, and Computer Control

Normally in patient scanning the detector is moved; however, it was more convenient in this work to move the source. This was done using an X-Y-Z traverse set rigidly onto an optical bench. The positional reproductibility in X and Y directions was better than 0.05 mm and in the Z direction better than 0.2 mm. The probes were placed on a platform that allowed for the alignments of their focal points to better than 0.2 mm in the critical transverse X direction, i.e. maximum separation of the crossed collimator axes was held to less than 0.2 mm. For the initial experiments the source was moved manually to a given X-Y-Z position and the coincident and/or single gamma counts were recorded on either a scaler or ratemeter for each position. Later, stepping motors were added to the X and Y axes, and the scanning position was controlled automatically by a computer system. In addition, the counts at each position were recorded and printed out by the computer system. The computerized scanner and interface are described in detail in Appendix B.

E. PSF Isoresponse Curves

1. Calculating Coincident Isoresponse Curves

In order to provide a simple check for the experimental set-up, the FCCS response to a 1 mm point source in air was determined for the two confocal probes. The response in the plane determined by the axes of the two collimators was also obtained for single gamma counting in each probe separately, and the product of their responses

compared with the observed two probe coincidence rate. For count rates down to 3 percent of the maximum, the product of the single count rates as a percentage of the maximum count rate (for each probe) compared to the coincidence count rate as a percentage of maximum coincidence count rate were within 5% throughout the plane, where data was recorded every 1.0 mm^2. This experiment verifies the theoretical formulation of Chapter IV, Part A and then justifies a prediction of the system's isoresponse to coincidences as being equivalent to the product of the single isoresponse curves of the two separate probes, for any angle, θ, between the probe axes. This can be calculated using two sets of the curves of Fig. 1 superimposed with one set rotated through angle θ. Figure 12 shows the same single gamma curves as Fig. 1 only enlarged in size and restricted to a region near the focal point. Figure 13 shows the single gamma isoresponse circles in a plane perpendicular to the collimator axis and going through the focal point. Figures 12, 13 and 14 appear to represent almost a family of concentric cylinders. Figure 14 shows the intersection of these isoresponse cylinders with a plane whose normal is 45^o to the collimator axis. These figures are helpful in calculating the two orthogonal or crossed probe coincidence isoresponse curves.

Figures 15 and 16 show such coincidence response curves; that is, the result of multiplying the values of two single gamma collimator isoresponse curves for $\theta = 90^o$ (for two probes whose axis are perpendicular). Figure 15 shows the coincidence isoresponse curves in the plane common to both probe axis, and Fig. 16 shows the coincidence

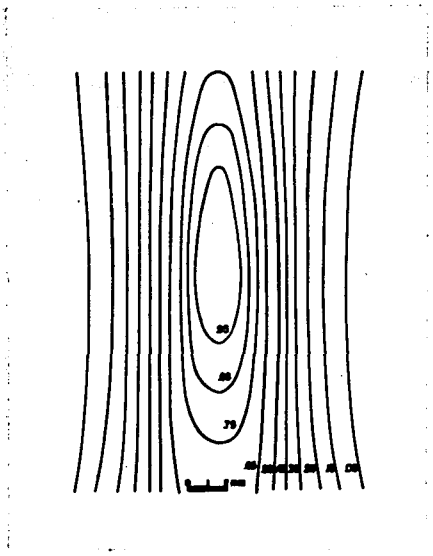

Fig. 12. Point source isoresponse curves near the focal region for the BNL collimators. The same section as Fig. 1 but magnified.

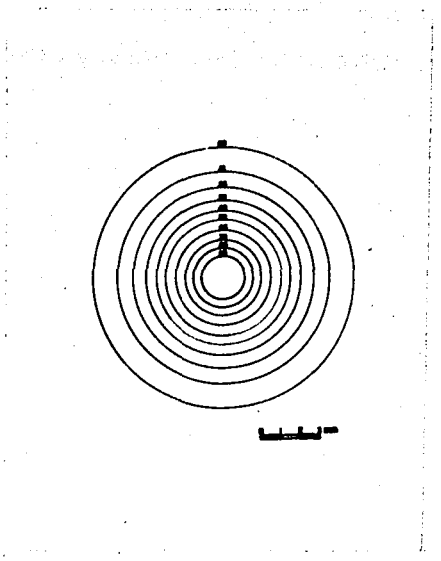

Figure 13. Point source isoresponse curves near the focal region for BNL collimators. The section through the focal point perpendicular to the collimator axis.

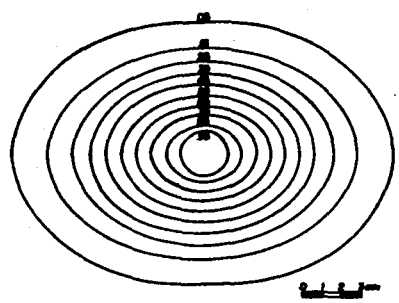

Figure 14. Point source isoresponse curves near the focal region for BNL collimators. The section at 45° to the planes of Figs. 12 and 13.

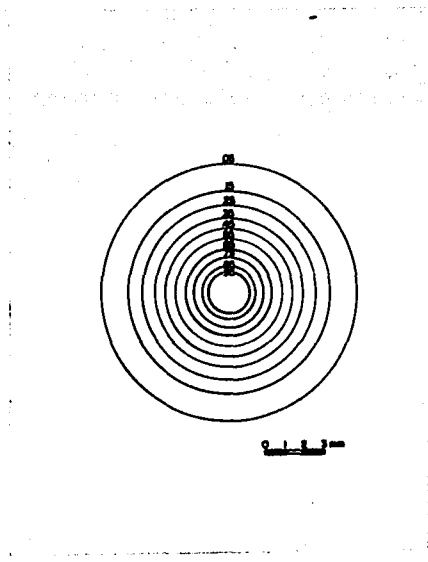

Figure 15. The isoresponse curves of the two detector FCCS system for coincidence scanning. The section in the plane common to both collimator axes.

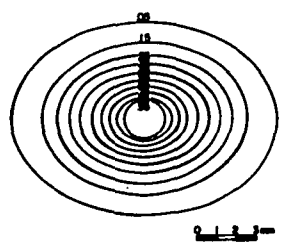

Figure 16. The isoresponse curves of the two detector FCCS system for coincidence scanning. The section in a plane perpendicular to that of Fig. 15.

isoresponse curves for planes perpendicular to that in Fig. 15. It can be seen that the coincidence isoresponse curves are the products of two families of cylinders of Figs. 12 through 14 "crossed" at 90^{o}. These coincidence isoresponse curves appear from Figs. 15 and 16 to be oblate spheroids or ellipsoids (ellipses of rotation). The focal region $\propto$ can then be estimated (using the FWHMs) as being an oblate spheroid whose dimension is greatest in the plane containing both probe axis (about 6.0 mm) and whose dimension is smallest in the direction perpendicular to this plane (about 4.2 mm).

2. Summed Single Gamma Ray Isoresponse Curves

In contrast to the coincidence response consider the two-probe summed single gamma response obtained by adding the single gamma responses of each probe. Figure 17 shows the summed single gamma isoresponse curves for the plane common to the two collimator axes (same plane as Fig. 15). The elongations or lobes of Fig. 17 lie along the collimator axes. Figure 18 is for planes common to either one of the collimator axes and perpendicular to the axis of the other one at the focal point. Figure 19 is for the plane perpendicular to the plane of Fig. 17, but in common with the axes angle bisector (45^{o} to the axes). Thus Figs. 18 and 19 represent the maximal and minimal sections of the isoresponse curves perpendicular to the plane of Fig. 17 determined by the collimator axes. Notice that Fig. 19 is identical to Fig. 14.

The coincidence isoresponse curves of Figs. 15 and 16 are quite tomographic in nature since the sensitive region is essentially confined

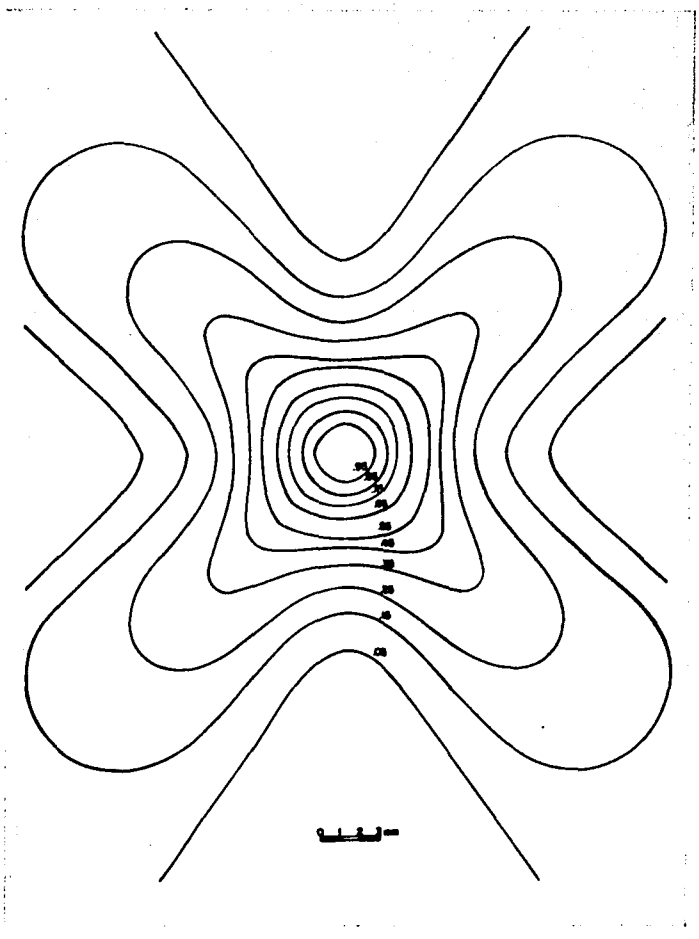

Figure 17. The isoresponse curves of the two detector system for summed single gamma counting. The section in the plane common to both collimator axes.

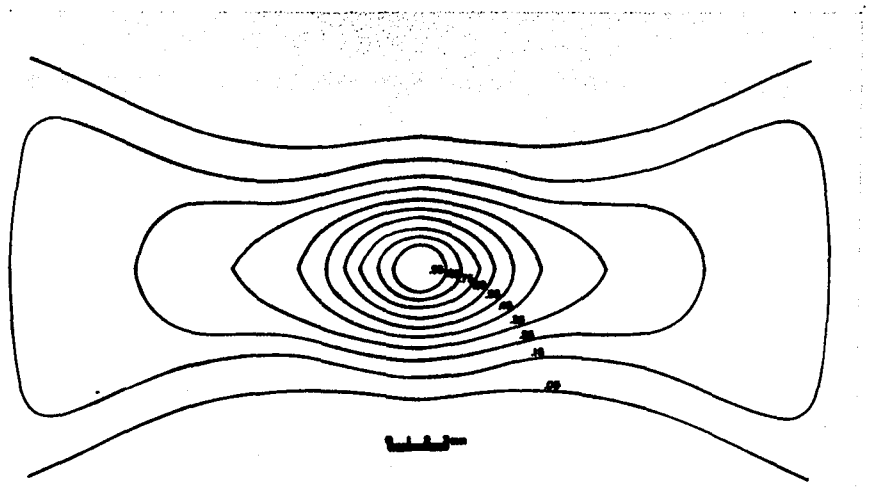

Figure 18. The isoresponse curves of the two detector system for summed single gamma counting. The section in the plane perpendicular to that in Fig. 17 but common to one of the collimator axes.

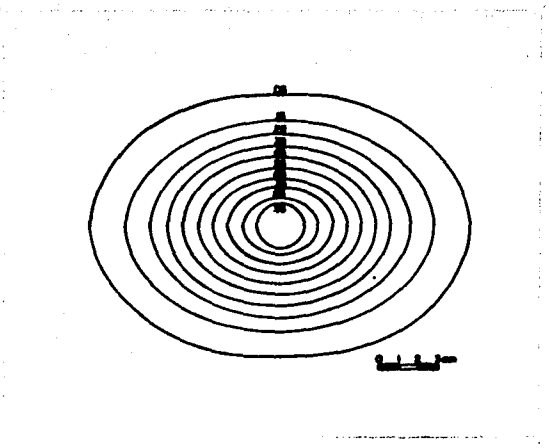

Figure 19. The isoresponse curves of the two detector system for summed single gamma counting. The section in the plane perpendicular to that in Fig. 17 but 45^{o} from that in Fig. 18 (in common with axes angle bisector). The isoresponse curves of Fig. 19 are identical to those of Fig. 14.

to small concentric oblate spheroids. The single gamma isoresponse curves of Fig. 17, however, are quite non-tomographic since the sensitive region ranges over large concentric "four-leaved-clover" shaped volumes whose leaves extend along the collimator axes.

3. Chance Coincidence Isoresponse Curves - Signal Compared to Noise

As was mentioned in Chapter IV the noise in FCCS is the chance coincident count rate. It can be seen that the spatial response for chance coincident counting is approximately the same as that for summed single gamma counting. Consider the isoresponse curves for a small point source (or defect) within a background source uniformly distributed throughout the field of view of both collimators of the two-probe device. Also consider the counts in one detector, say detector A, arising from the point source (or defect) within its field of view. The gamma rays coming from this source counted in detector A, $\Delta\gamma_A$, will contribute to the system chance coincidence rate according to Eq. (5.1):

$$\Delta C_A = 2\tau\gamma_B\Delta\gamma_A \,, \tag{5.1}$$

where γ_B is the single gamma rate for detector B and $\Delta\gamma_A$ and ΔC_A are negative for a defect. As the point source (or defect) is moved over the field of view of detector A, $\Delta\gamma_A$, will change according to the single gamma isoresponse curves for detector A. Since γ_B, the total single gamma count rate for detector B remains unchanged, then ΔC_A will vary as $\Delta\gamma_A$; that is, according to the single gamma isoresponse curves for detector A.

If the point source (or defect) is now considered for the field of view of detector B then Eq. (5.2) can be written for the contribution to the system chance coincidence rate due to the single gamma count rate $\Delta\gamma_B$ of detector B.

$$\Delta C_B = 2\tau \gamma_A \Delta\gamma_B \tag{5.2}$$

This chance coincidence rate will vary according to the single gamma isoresponse curves for detector B. Since the background distributed source is uniform we can assume $\gamma_A = \gamma_B$. Thus the total chance coincidence rate, $\Delta C_T = \Delta C_A + \Delta C_B$, will then vary as the sum of the single gamma isoresponse curves.

Since the off-focal chance coincidence count rate constitutes the noise relative to the true coincidence rate signal, the signal to noise ratio for FCCS will vary in space more closely with the signal. The reason for this is that the sensitive volume for the FCCS signal is a small oblate spheroid region whereas the sensitive volume for the noise is a large "four-leaved-clover-like" region. Thus even though the signal to noise ratio may be poor (less than 1), the spatial frequency response for high frequency spatial details appears to be much greater for the signal than for the noise (neglecting statistical fluctuations).

F. Calculation of Absolute Coincidence Count Rate

The isoresponse curves of the previous section give an idea of the size of the sensitive tomographic scanning volume region. By

assuming this region can be approximated by the focal volume equivalent to an oblate spheroid with a semi-minor axis of 2.1 mm and a semi-major axis of 3.0 mm, the simplified theory of Chapter IV, Part B can now be used to obtain a calculated value for the absolute coincident count rate sensitivity which can be compared directly with an experimental value. A volume phantom with concentration of 7.5 μCi/ml of ^{75}Se was used. The count rate of 200 cpm was obtained with the circuitry of Fig. A1 for the focal point placed 7mm below the surface of the phantom. The equations of Table 1 must be modified in order to provide for physical as well as geometric efficiencies. Such physical efficiencies include the fractional yield of gamma rays per disintegration of the isotope for each different gamma ray, the collimator septa penetration, the attenuation of gamma rays in the phantom, and the fractional loss of gamma rays which do pass through the collimator but do not register as pulses of the proper height. Equation (5.1) is the new equation representing the theoretical coincidence count rate.

$$\mu_2 = De_1e_2f_b^2 \propto {}_cA_1A_2 \tag{5.1}$$

$$e_1 = e_g e_{c1} f_{loss,1} \tag{5.2a}$$

$$e_2 = e_g e_{c2} f_{loss,2} \tag{5.2b}$$

In Eq. (5.1), D is the uniform volume concentration of

radioactivity. The symbol f_b is the fractional per disintegration yield from the isotope of the gamma rays in the two energy ranges of interest for each branch as determined by the branching ratios and conversion ratios of the radionuclide. The volume of the focal region for coincidence is α_c. The attenuation factors for the gamma rays as determined by the distance travelled in the phantom are A_1 and A_2. The efficiencies e_1 and e_2 are broken down in equations (5.2) to three factors. The first, e_g, is the geometric efficiency of the bare 5" detector without the BNL collimator. This is equivalent to the solid angle which a 5" diameter circle subtends at a point, F + t distance from the circle, where F + t are the sum of the collimator focal length and thickness. For the detectors used in this work e_g was 2.8%. Second, e_{ci} is the ratio of the number of counts detected from a point source at the focal point with the collimator in place compared to the number of counts detected using the same source in the same position without the collimator in place. This factor combines the geometric efficiency of the collimator with a factor determined by the septa penetration to give a quantity which is experimentally determinable. In this work, e_{c2}, for the higher energy gamma ray was determined to be 62% compared to the theoretical value of 63% determined from the collimator geometry. Because of scatter in the external lead shielding and K x-rays of lead, e_{c1} for the lower ^{75}Se energy range could not be measured accurately and was assumed to be 63% as well. The third factor in Eq. (5.2), $f_{loss,i}$, is a loss factor associated with the NaI crystal detector and its

geometry. Of the primary gamma rays which arrive at the crystal some may not produce pulses of the correct height to be counted. This may be due to compton scattering out of the crystal with resulting incomplete energy absorption, transmission through the crystal without being absorbed at all, light losses, noise, edge effects and statistical fluctuation. Because the gamma ray energies of ^{75}Se are fairly low there is hardly any transmission as such through the full 2" crystal thickness: none for the 135 keV gamma ray and about 2.5% for normally incident 265 keV gamma rays. The absolute contributions to the loss factors $f_{loss,\ 1}$ and $f_{loss,\ 2}$ of the other above mentioned phenomena are difficult to assess precisely; however, the ratio of the two factors was easily determined from the energy spectrum and branching ratios for single gamma ray emission from ^{75}Se. About 15% more lower energy gamma rays were detected than higher energy gamma rays in the energy spectrum, whereas from the decay scheme of ^{75}Se it can be seen that a lower energy gamma ray has less probability of being emitted than a higher energy gamma ray, the ratio being 0.87. The ratio of loss factors, $(f_{loss,2} / f_{loss,\ 1})$, is then 0.76. Furthermore, considering the fact that the half value layer in NaI for 135 keV gamma rays is about 2 mm it is doubtful that $f_{loss,\ 1}$ is much less than 1.0. If this is assumed, then $f_{loss,\ 2}$ can be taken to be about 0.75. We believe this more significant loss factor for the higher energy gamma rays is due to compton scatter out of the crystal and the shorter oblique path length possible through the crystal near its edge. This latter effect is due to the fact that the collimator

"cone" of acceptance whose apex is at the collimator focal point has a circular base 5" in diameter only at the nearest face of the 5" diameter cylindrical crystal. Two inches further, at the rear face of the still 5" diameter crystal the base of the "cone" of acceptance is almost 6.5".

Let us now estimate the remaining parameters of Eq. (5.1) in order to obtain a theoretical value for μ_2. A review of the calculations appears in Table 3. The concentration of ^{75}Se, D, at the time of scanning was about 7.5 $\mu Ci/cm^3$ for the 21 cm^3 phantom. The fraction f_b as determined by the decay scheme of ^{75}Se is actually a combination of the two schemes as indicated in Fig. 10. The gamma rays of 121 keV and 280 keV are detectable in coincidence 16% of the time and those of 136 keV and 265 keV are detectable in coincidence 55% of the time. The resulting factor f_b is equivalent to the sum of these percentages, (0.16 + 0.55) = 0.71. The focal volume α_c is estimated to be about 0.08 cm^3. Finally, the effective attenuation factor per coincidences, A_1A_2, for about 7 mm depth in the phantom is 0.76. Substituting these values into Eq. (5.1) gives a true focal coincident rate μ_2 of about 170 cpm compared to the measured value corrected for statistical coincidences of about 200 cpm. This is quite a good agreement considering the simplifications of the theory, the uncertainty in the estimate of the effective focal volume α_c, and the uncertainty in determining the isotope concentration.

TABLE 3

ABSOLUTE EXPERIMENTAL FCCS VALUES

Sympol		Equivalence
μ_2	=	$D \propto (N\lambda/2)^2$ (Att)
	=	$D(N\lambda_1/2)(N\lambda_2/2)f_b \alpha_c A_1 A_2$
	=	$D(e_1)(e_2)f_b \alpha_c A_1 A_2$
e_i	=	$N\lambda_i/2$ = efficiency of γ_i in one collimator
	=	$e_g e_{ci} f_{loss,i}$
e_g	=	geometric efficiency of 5 in detector at F + L from focus = 2.8%
e_{ci}	=	ratio for gamma ray i of focal point efficiency with and without collimator; function of collimator geometric efficiency and septal penetration = 0.63
$f_{loss,i}$	=	losses due to crystal penetration and scatter
$f_{loss,1}$	=	1.0
$f_{loss,2}$	=	0.75
f_b	=	factor due to branching ratios from decay scheme = 0.16 + 0.55 = 0.71
D	=	isotope concentration = 7.5 μCi/cm^3
α_c	=	focal volume = $(4/3)\pi a^2 b$ = $(4/3)\pi(0.3)^2(0.21)$ = 0.079 cm^3

TABLE 3 cont.

Sympol		Equivalence
A_1A_2	=	attenuation factor for 7 mm in z-direction
	=	(0.854)(0.889) = 0.76
μ_2	=	$(D)(\alpha_c)(A_1A_2)(f_b)(e_{c1})(e_{c2})(e_g)^2(f_{loss1})(f_{loss2})$
	=	169 cpm

CHAPTER VI

EVALUATION CRITERIA FOR THREE DIMENSIONAL SCANNING

Before going on to consider the use of the above described system for scanning, the evaluation criteria for scanning of Chapter II must be generalized to three dimensions.

A. The Effect of Finite Counts in Three Dimensional Scanning - Volume Information Density (VID)

For a three dimensional radioisotope scan just as for a two dimensional scan the image contrast variations must not be overly blurred by statistical count fluctuations in order for the scan to have clinical usefulness. In two dimensions the measure of this statistical quality as defined in Chapter II was counts per scan area or information density. The natural generalization for this concept in three dimensions is the counts per scan volume or volume information density hereafter referred to as VID. The information for standard two dimension projection scanning will be referred to as the planar information density or PID. Similarly, if N is now the background counts collected per unit volume, and it is required that a contrast change of P percent be detected with confidence, then (0.01)PN must be a few times greater than the standard deviation of N, i.e. the square root of N, depending upon the degree of certainty required. If $(0.01)PN \gtrsim 3\sqrt{N}$ for example, then $P\sqrt{N} \gtrsim 300$. Thus the detection of finer contrast gradations will require a higher VID. For a three dimensional rectilinear scanner scanning successive planes normal to the Z axis, the VID equals (counts per minute)/ [(line spacing in Y

direction) x (plane spacing in Z direction) x (speed in X direction)] .

Since three dimensional clinical scanning procedures do not exist as yet there are no typical VIDs usable for comparative purposes; however, two general considerations should be made as guidelines in deciding what VIDs to require should such three dimensional procedures become available.

a. First of all it should be realized that since there will be much more information in a three dimensional scan of a given source than in a two dimensional projection scan, significantly more time may be required to obtain such information. This information is qualitatively different in that there may be lesions in depth detectable by three dimensonal scans yet completely missed in projection scans. If this additional information is clinically essential the additional scan time required may become acceptable.

b. The requirements for statistical quality for three dimensional scan picture elements may be considerably reduced compared to that for projection scan picture elements. If a complete three dimensional image is obtained, the detection of lesions in space will be a different perceptive procedure in correlating information in three rather than two dimensions. The number of information or picture elements is thus considerably greater and, therefore, the statistical quality of each one need not be so great. Conversely, if only a few slices are of clinical usefulness a higher VID would be required since three dimensional correlations would then no longer be available.

B. Spatial Resolution (Infinite Counts)

1. Existing Tomographic Resolution Evaluation Criteria

As indicated in the review of tomographic nuclear imaging techniques in Chapter III above, almost all existing techniques involve obtaining information from only one section or slice of the source at a time. Since the longitudinal or tomographic resolution obtainable has not been as good as the transverse resolution, it is understandable that the criteria for evaluating tomographic scans have been somewhat less precise than the response functions and MTFs used to evaluate transverse resolution.

The longitudinal FWHM of a transverse line source has been used to evaluate tomographic resolution for a new slanted-hole rectilinear scanner (33). However, it has been shown that transverse FWHMs of line sources are insufficient (4). They do not contain information about the shape and the tail of the line source response function. It would seem to be apparent that the longitudinal FWHM would also be insufficient in describing the complete longitudinal spatial response of a scanner.

Muehllenher (34) has pointed out the difficulties involved in using the full longitudinal line source response function and MTF due to the sharp truncation at the boundary of the scanning device itself. He has suggested instead the use of the concept of specificity defined as the difference in the MTFs of a fixed line source measured in its focal plane and in an adjacent image plane, normalized to the response in the focal plane. It would

appear that this concept is again limited to slice or section scanning where the longitudinal resolution is not as good as the transverse resolution. He states in fact, "no image exists in the perpendicular direction and there are only a limited number of images at right angles to the direction in which the response is measured" (34). In addition, the specificity does not describe the tomographic effect in a unique way (34).

2. Generalization of Resolution Evaluation Criteria to Three Dimensions

In FCCS the scan image is indeed a three dimensional one rather than a series of two dimensional slices and so more precise criteria for evaluating the three dimensional resolution performance are indicated. Consider extending the concepts of PSF, LSF, and MTF to three dimensional scanning where each direction is equally significant. For such a situation the source distribution and image count distribution may be considered three dimensional functions in an infinite vector space whose basis set are three dimensional linearly independent orthonormal functions such as the sinusoidal varying functions of Eq. (6.1).

$$B_3 = \left\{ \exp(i\,\omega_x X), \exp(i\,\omega_y Y), \exp(i\,\omega_z Z) \right\} \qquad (6.1)$$

Just as in the two dimensional case, all images are made up of linear combinations of the basis functions. How well a given three dimensional spatial frequency signal is recorded, that is to say, how good the frequency response of the system is, can be seen to be a complete measure

of the three dimensional system resolution. Further paralleling the two dimensional case, a point source contains all frequencies in B_3 and, therefore, the fourier transform of the point source image or PSF is the three dimensional measure of frequency response or MTF as indicated in Eq. (6.2).

$$MTF(\omega_x,\omega_y,\omega_z)=\int_{-\infty}^{\infty}\int_{-\infty}^{\infty}\int_{-\infty}^{\infty} dXdYdZPSF(X,Y,Z)\exp i(\omega_x X+\omega_y Y+\omega_z Z) \quad (6.2)$$

If the PSF were spherically symmetric, similar conclusions about the MTF could be drawn as were given in Chapter II, Part A.2. However, as was shown in Chapter V, Part E above, the PSF for the two probe FCCS system is not spherically symmetric. Furthermore, it might be useful to consider the general case where minimal symmetry could be assumed.

3. Other Complete Sets and Assumptions About Translational Invariance and Attenuation

In addition to the complete set of three dimensional sinusoidal functions mentioned above there are three other complete sets of functions worth discussing. Just as in the two dimensional case the set of PSFs form a complete although not orthonormal set. Considered at this point in the discussion, of course, the PSFs are three dimensional, such as the PSFs of the FCCS system in the summed single gamma and coincident gamma modes shown in Chatper V above.

The set of three dimensional LSFs although also forming a second complete set of functions are very inconvenient to consider. For

example, in the top of Fig. 20 is shown a central section of a fictitious family of PSF isoresponse curves, where cylindrical symmetry is assumed around the Z axis. The response for a line source parallel to the Y axis (perpendicular to the plane of the figure) in position X=-d may be greater than the response for such a line source at X=0. The LSF(X=-d,Z), curve B in the bottom of Fig. 20, is considerably wider than the LSF(X=0, Z) or curve A. To characterize the tomographic response of such a system by curve A alone would be misleading. The complete set of LSFs not only for line sources parallel to the Y axis, but for all line sources perpendicular to the X axis would have to be given. Even then this set of LSFs would not be unique. The set of line sources for all directions where the LSFs go through the origin would also be a complete set of LSFs yet entirely different from the first one.

The most natural and advantageous way to generalize the LSF to three dimensions is to introduce a third new complete set of functions, the set of surface source response functions (SURFs) for plane infinite surface sources.

The response of the system of Fig. 20 to plane surface sources whose normals point in any direction is a unique and complete set of response functions. The surface source would cut through all isoresponse curves, and hence, the total sensitive volume of the scanner would be sampled for each SURF. In addition, a SURF in any particular direction would give direct information about the response of the imaging system to edges and boundaries of organs and sources in clinical scanning

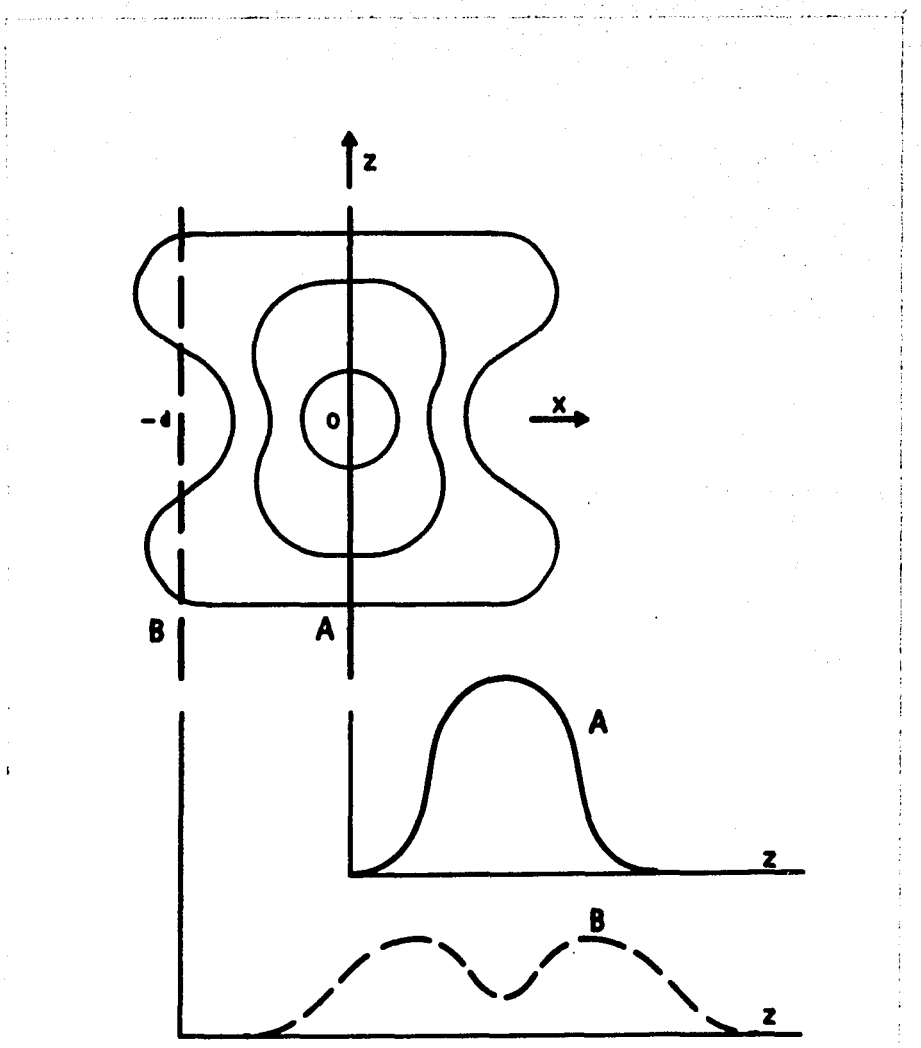

Figure 20. Top. A fictitious family of point source isoresponse curves. Middle. The LSF corresponding to a line at X=0, perpendicular to the X-Z plane. Bottom. The LSF corresponding to a line at X= -d perpendicular to the X-Z plane.

procedures, whereas LSFs and even PSFs would not. (Although PSFs would give better information about small lesion detection capabilities.)

The fourier transform of the SURF can be defined as determining the frequency response of a three dimensional scanner in a given direction, and thus may be thought of as a three dimensional or tomographic transfer function.

$$TTF(\omega) = \int_{-\infty}^{\infty} dX SURF(X) \exp i\omega X \qquad (6.3)$$

It may be noted at this point also that there are two additional sets of functions that can be considered. The functions that represent the response to a two dimensional edge which will be called ESFs or edge source response function are closely related to the LSFs. Also the functions that represent the response to a three dimensional step which will be called STPFs or step source response functions are closely related to the SURFs. The ESFs and STPFs bear the same relationship to the LSFs and SURFs as does the Heaviside function to the δ-function. Table 4 reviews all the response function definitions.

In order for any of the above response functions to form a complete set, the response functions must be found at each point in space. It is necessary then to simplify this task by assuming the translational invariance of the response functions or at least that the change in response functions from place to place in the viewing field is gradual or small after standard attenuation corrections are made.

TABLE 4

REVIEW OF RESPONSE FUNCTIONS

SYMBOL	Type of Scanning Where Useful (Dimensions, D)	Test Source
PSF	2D or 3D	point
LSF	2D	line
ESF	2D	edge
SURF	3D	plane-surface
STPF	3D	step
MTF	2D or 3D	sinusoidal - general direction
TTF	3D	sinusoidal - specific direction

In the case of the FCCS geometry discussed in Chapter V it is clear that these assumptions are exactly true in the X and Y directions. For different values of Z, however, the attenuation differences due to differences in the path lengths of the gamma rays to the detectors must be corrected by the usual exponential attenuation corrections. After these corrections are applied the validity of the assumption of a gradual translational variation must be experimentally verified, and this is done below in Chapter VII.

4. Special Cases of Separation of Variables and Ellipsoidal Symmetry

In order to obtain the three dimensional MTF in Eq. (6.2) above a difficult integration must be done. If the PSF can be further simplified, then the calculation of the MTF may be made more easily carried out. For example, if to first order the dependence of the PSF upon X, Y and Z can be separated as indicated in Eq. (6.4), then Eq. (6.5) results.

$$PSF(X,Y,Z) = f(X)g(Y)h(Z) \tag{6.4}$$

$$MTF(\omega_x,\omega_y,\omega_z)=\left[FTf(\omega_x)\right]\left[FTg(\omega_y)\right]\left[FTh(\omega_z)\right] \tag{6.5}$$

In Eq. (6.5) FT indicates the fourier transform. The problem of finding the MTF then becomes one of doing three separate single variable integrations. In addition equations (6.6) can be used with equations (6.5) and (6.3) to derive equation (6.7) where K_x, K_y, and K_z are

normalization constants.

$$\begin{aligned} SURF(X) &= f(X)\int_{-\infty}^{\infty}\int_{-\infty}^{\infty} dYdZg(Y)h(Z) = K_x f(X) \\ SURF(Y) &= g(Y)\int_{-\infty}^{\infty}\int_{-\infty}^{\infty} dXdZf(X)h(Z) = K_y g(Y) \\ SURF(Z) &= h(Z)\int_{-\infty}^{\infty}\int_{-\infty}^{\infty} dXdYf(X)g(Y) = K_z h(Z) \end{aligned} \tag{6.6}$$

$$MTF(\omega_x, \omega_y, \omega_z) = \frac{[TTF(\omega_x)]\ [TTF(\omega_y)]\ [TTF(\omega_z)]}{K_x K_y K_z} \tag{6.7}$$

Thus the total system response can be determined by only three simple plane surface source response measurements where the normal to the surface source is in either the X, Y or Z directions. These three SURFs will be designated X-SURF, Y-SURF, and Z-SURF.

If the further simplifying assumption of ellipsoidal symmetry for the PSF can be made, then from the proof in Appendix C it can be seen that the PSFs and SURFs must be gaussian in shape. The assumption of ellipsoidal symmetry for the two probe FCCS system PSF is justified experimentally by the data of Chapter V. In addition, a theoretical discussion of the plausibility of circular symmetry for planes parallel to the Y-Z plane (containing the collimator axes is given in Appendix D.

CHAPTER VII

QUANTITATIVE FCCS RESOLUTION MEASUREMENTS AND PERFORMANCE

A. Experimental PSF and SURF Measurements in Scattering Media

1. Preparation of the Radioisotope Test Sources

In order to determine the resolution of the two probe FCCS system, a point source of approximately 3 μCi of ^{75}Se was prepared. The point source was made by successively evaporating droplets of a highly concentrated ^{75}Se labeled sodium selenite solution onto a shallow well formed of thin polystyrene. The point source formed was shaped like a thin disc or spot of diameter less than 0.8 mm and thickness equal to the thin evaporated film, estimated to be less than 0.03 mm. The source was sealed by placing a small disc of thin polystyrene over the radioactive spot and using a polystyrene solvent as the sealant.

A surface source was also prepared. The container of the surface source consisted of a sandwich of two 5" x 5" x 1/8" sheets of polystyrene separated by a 20 mil (0.5 mm) spacer in the shape of a frame. The radioactive region was a 4" x 4" x 0.02" volume filled with sodium selenite solution. The areal concentration was approximately 10 μCi/cm^2.

2. Comparison of FCCS Response Functions to Single Gamma Response Functions in the Absence of Scatter

Figure 21 shows a comparison of the X-PSF and X-SURF for summed single gamma scanning with those for FCCS. The FCCS system was geometrically oriented as in Fig. 11 and employed the circuit of

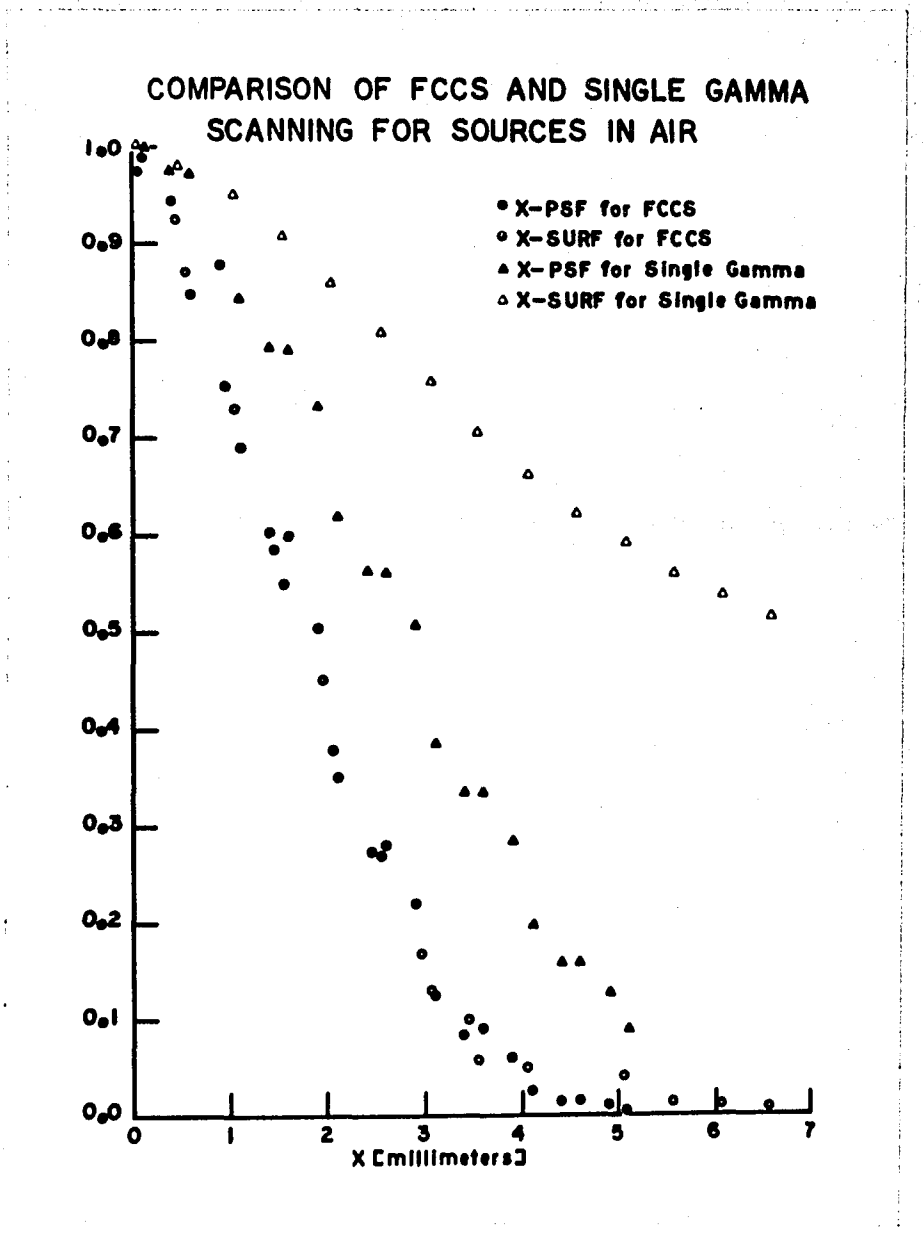

Figure 21. Response functions for point and plane surface sources in air comparing FCCS with single gamma ray scanning in the X direction (perpendicular to both probe axes). Notice that FCCS response functions are narrower, and the FCCS PSFs and SURFs are nearly identical. All data for this figure and similar ones to follow are statistically accurate (one standard deviation) to better than 2% of the maximum response. The source position accuracy in the X and Y directions is about $\pm$0.02mm and in the Z direction is about $\pm$0.1mm. The scatter in the data then appears to be due primarily to other factors such as instrument drifts and small instabilities. The scatter itself provides a measure of the accuracy of the data.

Fig. A.3. Figure 22 shows the same comparison for Y axis response functions. The comparison of Z direction responses (not shown) is similar to those for the Y direction. The sources were placed in air with no scattering medium nearby. It is clear that the single gamma response functions are much broader than the FCCS responses and the Y-SURF (the SURF taken with the normal to the plane surface source pointing in the Y direction) for single gamma scanning indicates that the resolution for the Y direction is almost nil. In contrast the FCCS response functions which have been corrected for chance coincidences all have full widths at a tenth of maximum (FWTM) less than 1.2 cm.

3. Effect of Scatter on FCCS Spatial Resolution

In order for FCCS to be a viable method for radioisotope scanning the high spatial resolution characteristics observed for sources in air must be reasonably well preserved when the sources are in scattering media. Because of the low energy emissions from ^{75}Se the attenuation of a point source signal for the two probe system for Fig. 11 would be fairly high, about 45% for every 2 cm of tissue equivalent thickness added in the Z direction. Figure 23 shows the effect on the energy spectrum of 5.5 cm of polystyrene scattering material placed between the point source and each detector (equivalent to 3.9 cm in the Z direction). From the known effect of these factors in decreasing the resolution of single gamma scanning one might expect that the FCCS resolution characteristics would be similarly degraded for just a few centimeters of scattering material. However, if the types of scattering events which can be accepted by the two probe

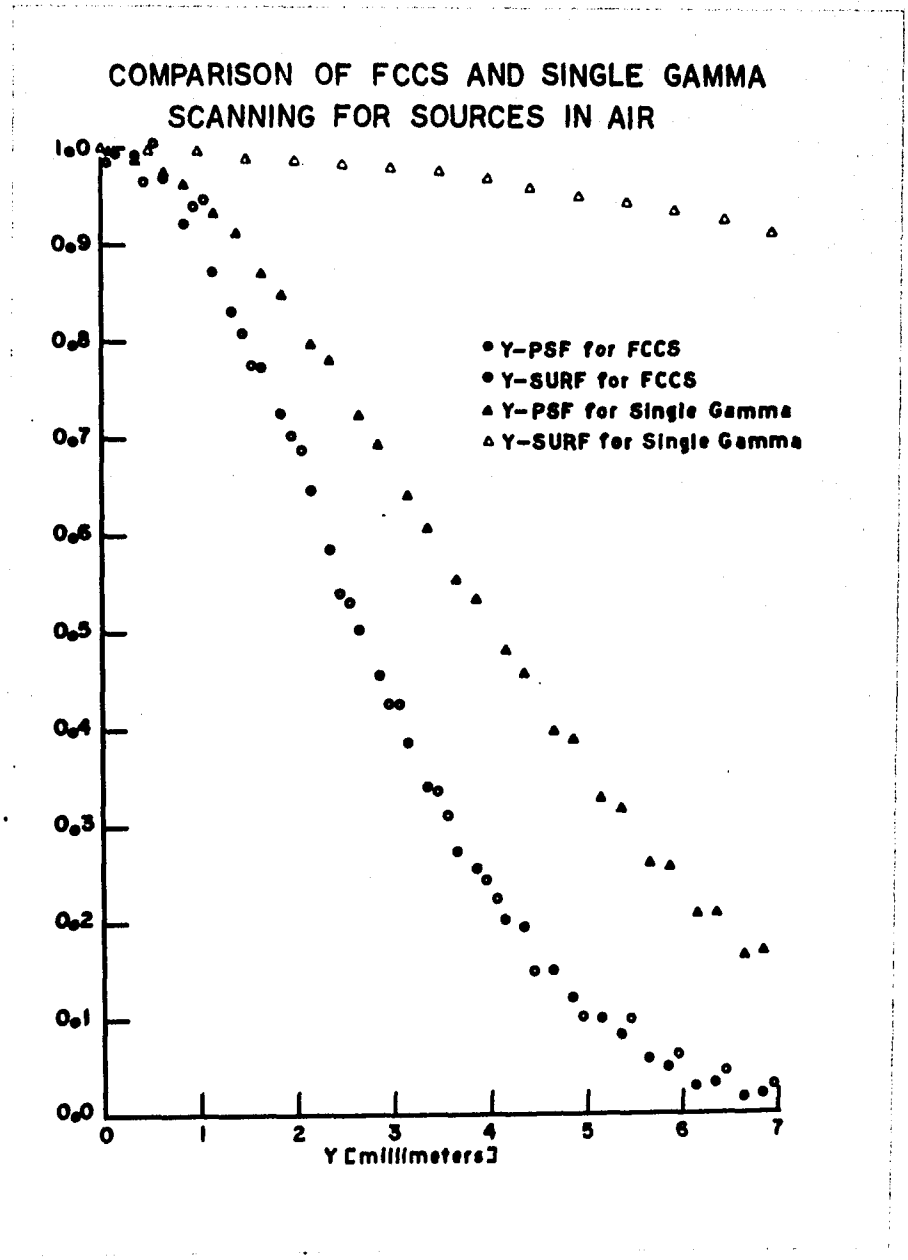

Figure 22. Same as Fig. 21 but for response functions in the Y direction.

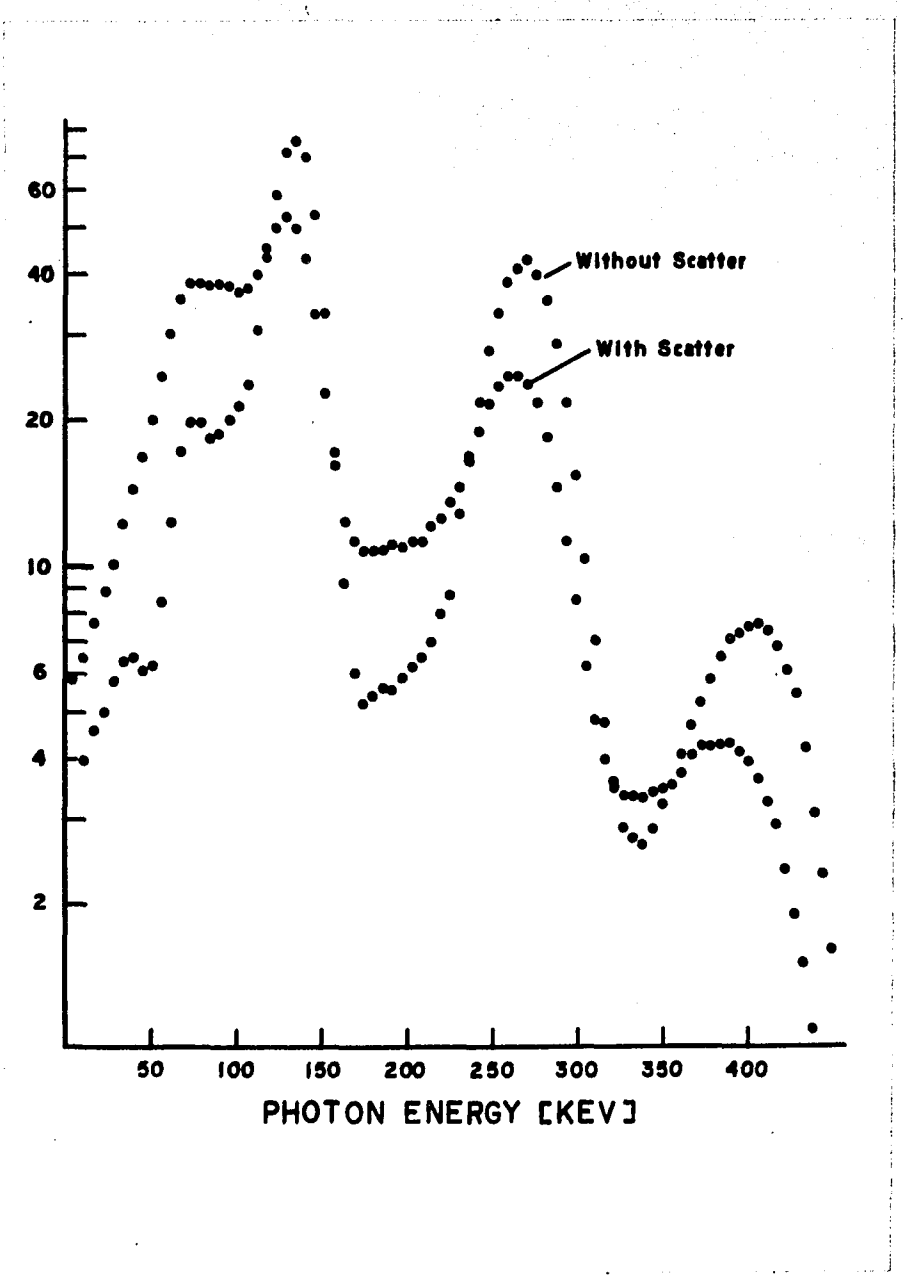

Figure 23. Energy spectrum for ^{75}Se source in air (without scatter) compared with that using 5.5 cm of polystyrene between the source and detector (with scatter). Notice for the spectrum with scatter the 265 keV and 410 keV peaks are reduced while the 135 keV peak is much broader. The structure in the 135 keV peak on the lower energy side corresponds to lead x-rays from the probe shielding.

system are examined, it can easily be seen that the FCCS system discriminates strongly against off-focal sources.

The effect of scatter on FCCS resolution was studied experimentally. The response functions were measured for thicknesses of from 0 to 4 cm of polystyrene for each major direction and are shown in Figs. 24, 25, and 26 for the point source and in Figs. 28, 29, and 30 for the plane surface source. Since the response functions are essentially symmetric about the focal region only one half of the curves are shown. Each figure indicates the measured responses for different attenuations, and as is evident, they are virtually indistinguishable. Thus it appears that although attenuation of the image signal is significant, the loss in tomographic spatial resolution with depth of scattering medium appears to be quite small for FCCS.

4. Experimental Determination of the FCCS Response Function Shape and Symmetry

Figure 27 shows a comparison between the measured FCCS point source response functions for the X, Y and Z directions. It can be seen that the Y-PSF and Z-PSF are almost identical (as are the Y-SURF and Z-SURF). This confirms the circular symmetry around the X direction of the FCCS isoresponse curves as obtained in Chapter V by multiplying single gamma isoresponse curves (see also Appendix D). In contrast, as expected, the X-PSF is sharper than the Y-PSF or Z-PSF in Fig. 27, just as the X-SURF is sharper than the Y-SURF or Z-SURF (not shown). These facts again confirm the oblate spheroidal nature of the PSF obtained in Chapter V where the oblated portion is along the

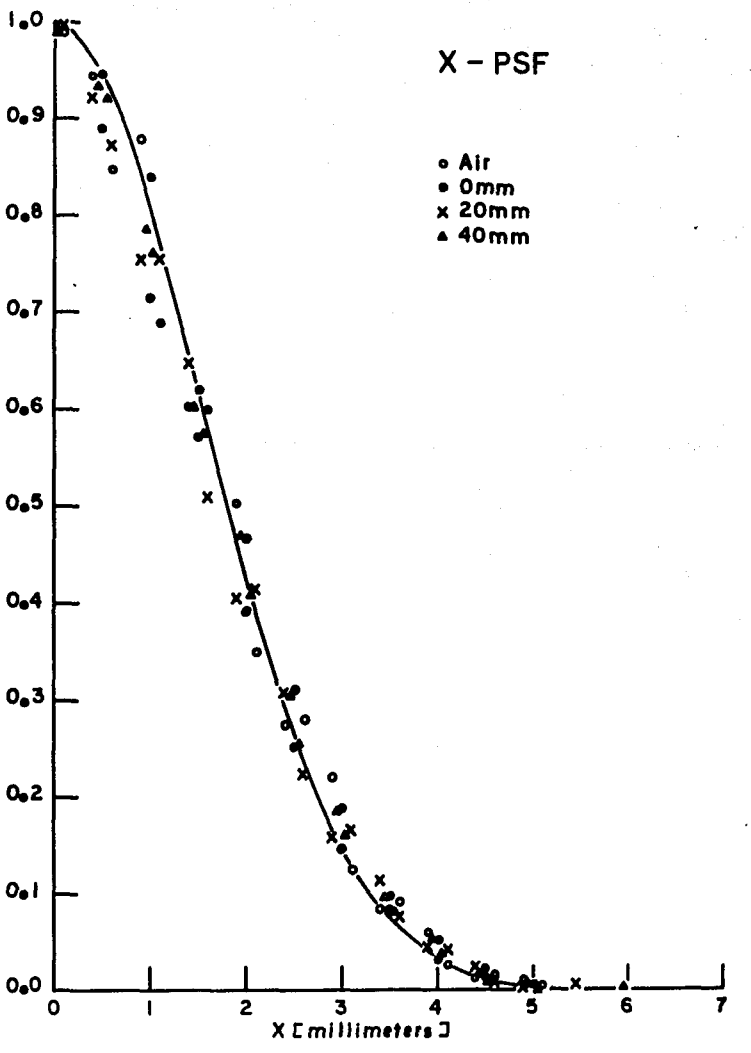

Figure 24. Point source response functions in X direction for various indicated Z-thicknesses of scattering material placed between the point source and the two detectors. All PSFs are normalized to their maximum values so that the attenuation with increased scatter thickness would not hinder comparison of the spatial resolution at the various depths. Notice the spatial resolution does not appear to deteriorate with depth. Solid curve is least squares gaussian fit.

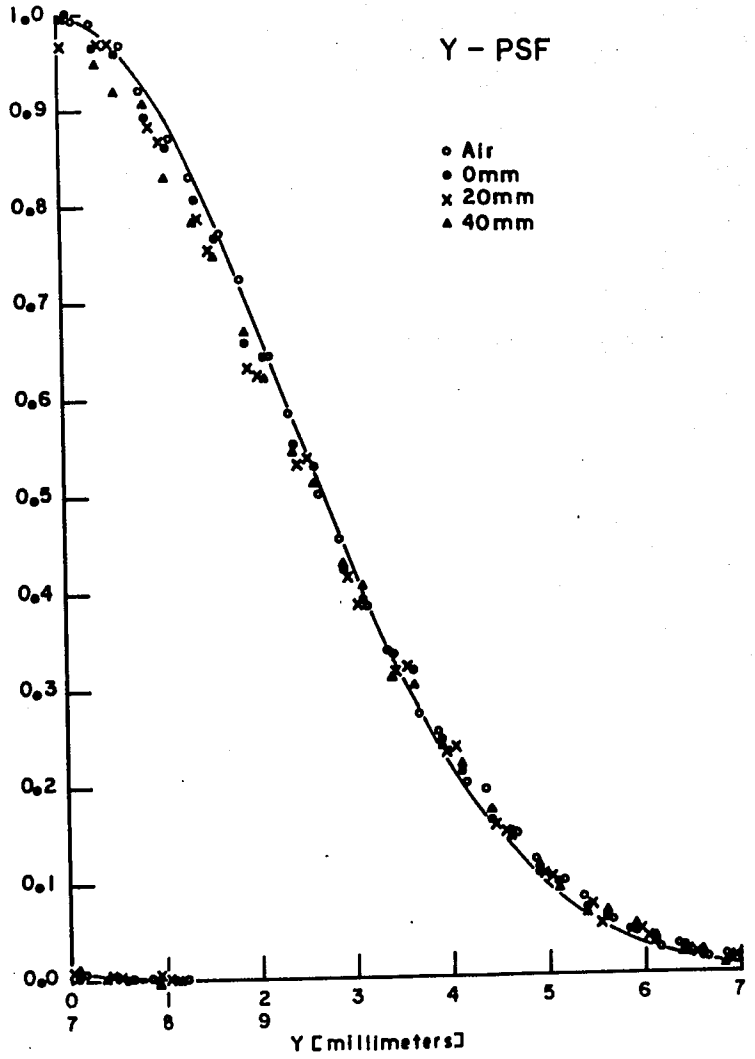

Figure 25. Same as Fig. 24 but for response functions in Y direction.

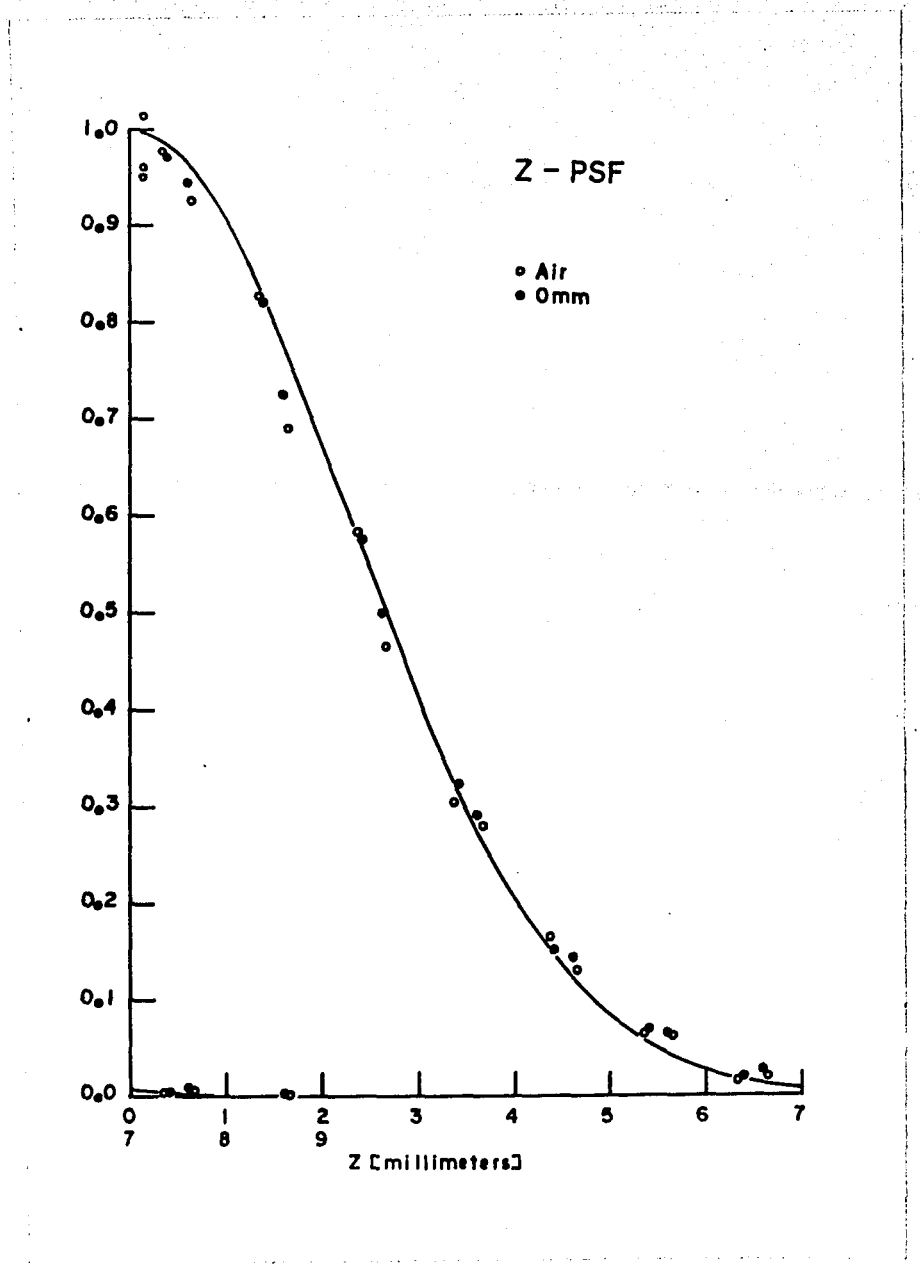

Figure 26. Same as Fig. 24 but for response functions in Z direction.

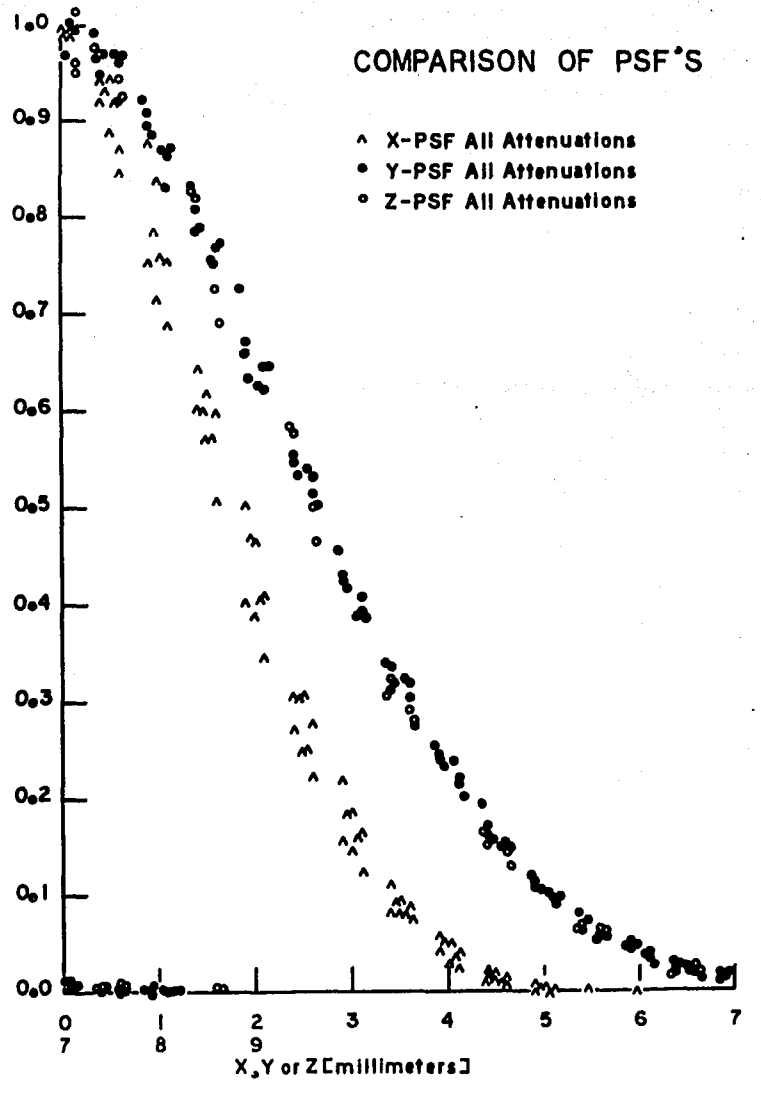

Figure 27. Comparison of PSFs for all scatterer thicknesses showing nearly the same responses in the Y and Z directions but sharper resolution in the X direction.

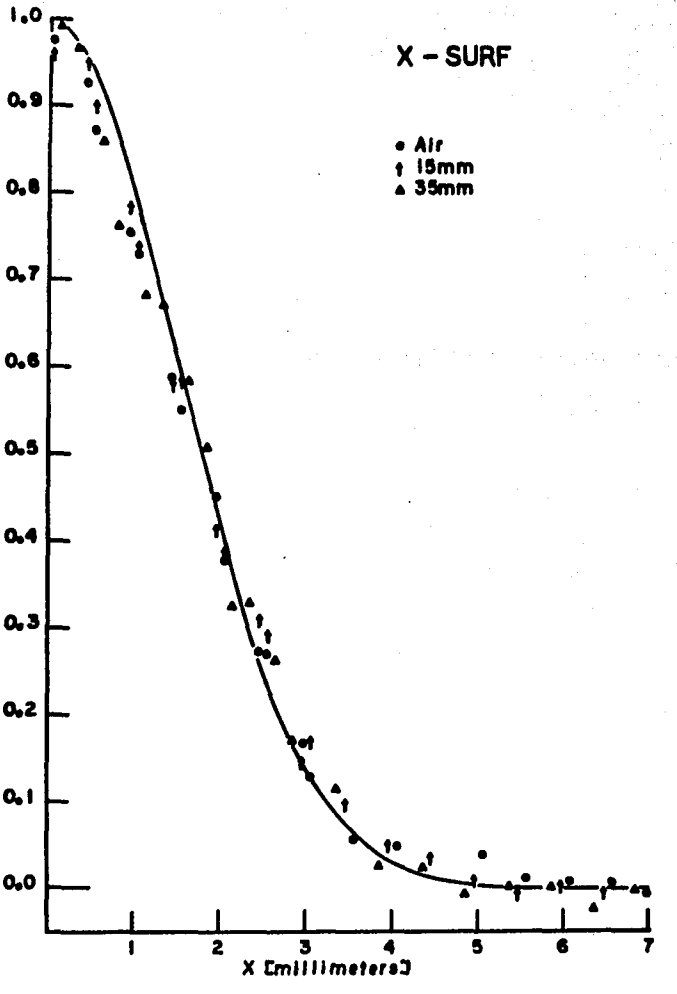

Figure 28. Surface source response functions in X direction for various indicated Z-thicknesses of scatterer. All SURFs are normalized to unity independent of scatterer attenuation. Notice that just as for the PSFs, the SURFs do not appear to change very much with depth. Solid curve is least squares gaussian fit.

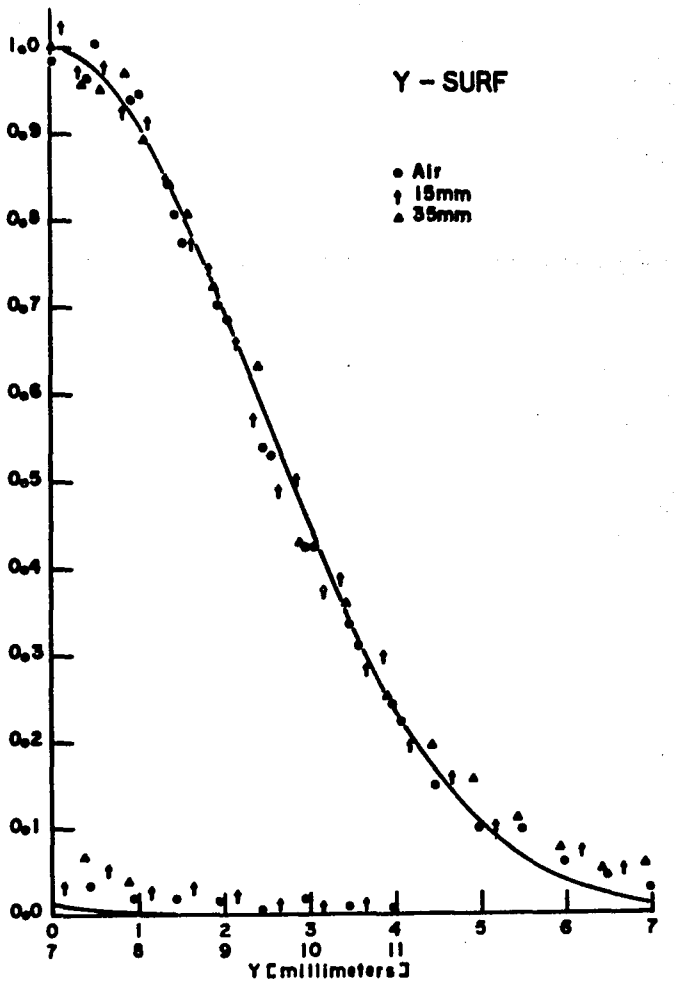

Figure 29. Same as Fig. 28 but for response functions in Y direction.

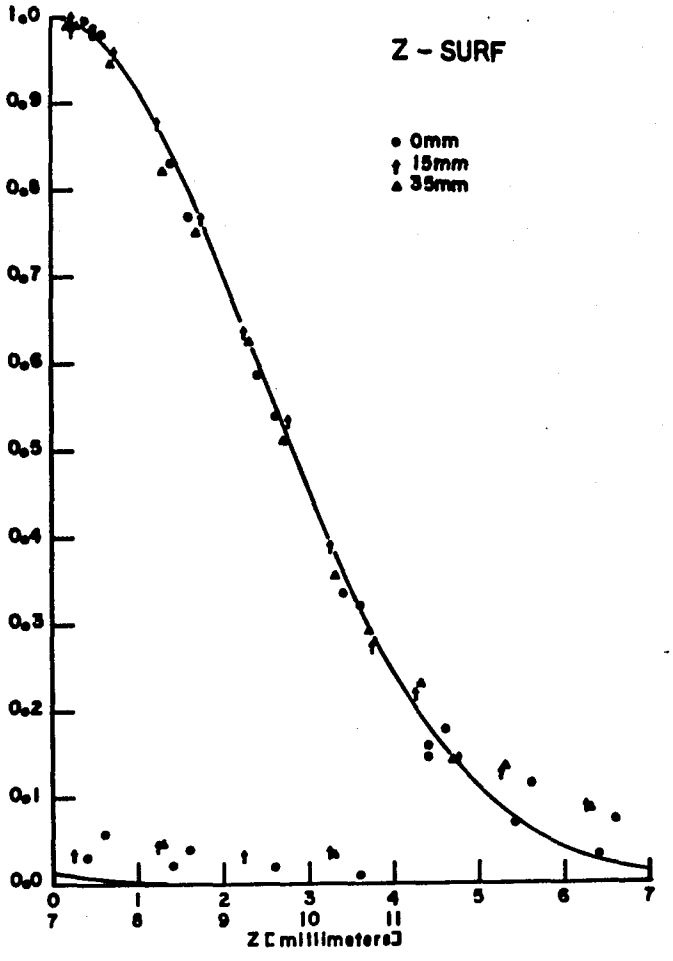

Figure 30. Same as Fig. 28 but for response functions in Z direction.

X direction hence explaining the sharper resolution in the X direction.

In order to evaluate the separability of the PSF as defined in Chapter VI above, the X-PSF and X-SURF are plotted on the same graph in Fig. 31 as are the corresponding response functions for the Y and Z directions drawn in Figs. 32 and 33. It can be seen that except for the tails of the SURFs, the PSFs are essentially the same as the SURFs indicating that equations (6.6) are nearly satisfied and thus providing a test of the separability property.

When the comparison of X-PSFs and X-SURFs were first made it was noticed that the curves other than the tails were the same except that the X-SURF curves were translated about 0.25 mm to the right of the X-PSF curves. It seems plausible to explain this disparity by considering the fact that the actual thickness of the surface source was about 0.5 mm whereas the point source was aligned so that its width in the X direction was considerably less than 0.03 mm. Since only half of the total X-SURFs are plotted, half the source thickness or 0.25 mm was used to correct all of the X-SURF positions for the width of the surface source. Since the widths of the surface source and that of the point source in the Y and Z directions are comparable and the response functions are not as sharp, no correction was made for source fine structure in the Y and Z response functions.

Since it appears that circular symmetry and separability of variables are both approximated by the FCCS PSFs it is natural to compare measured curves to least square fits of gaussian functions. Such gaussian fits appear as solid lines in Figs. 24, 25, and 26, and

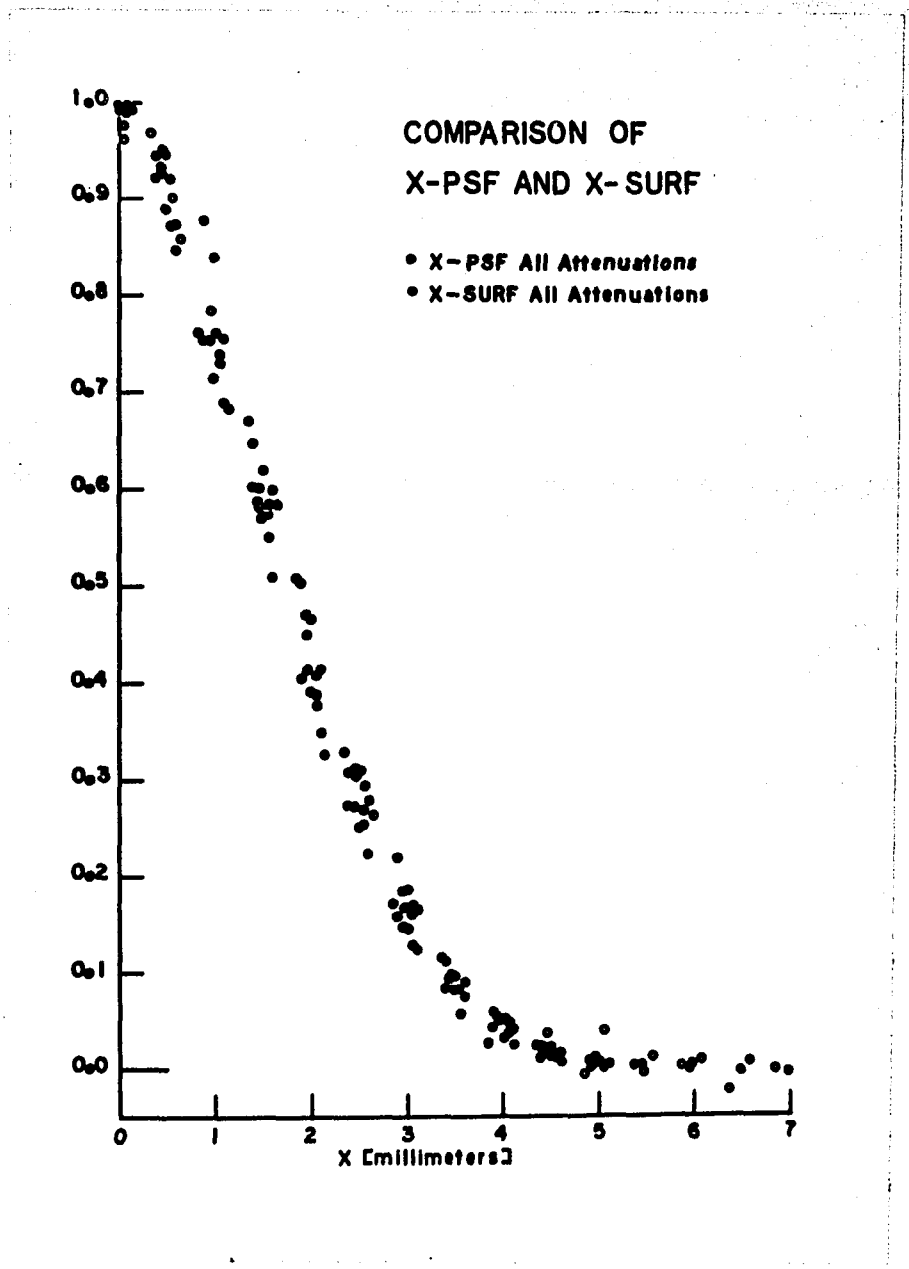

Figure 31. The PSF and SURF for all attenuations are compared for the X direction. The shapes of the PSF and SURF appear similar. The data has been corrected for the relative thickness of the plane surface source ($\sim$ 0.5 mm) compared to the point source ($\sim$ 0.03 mm).

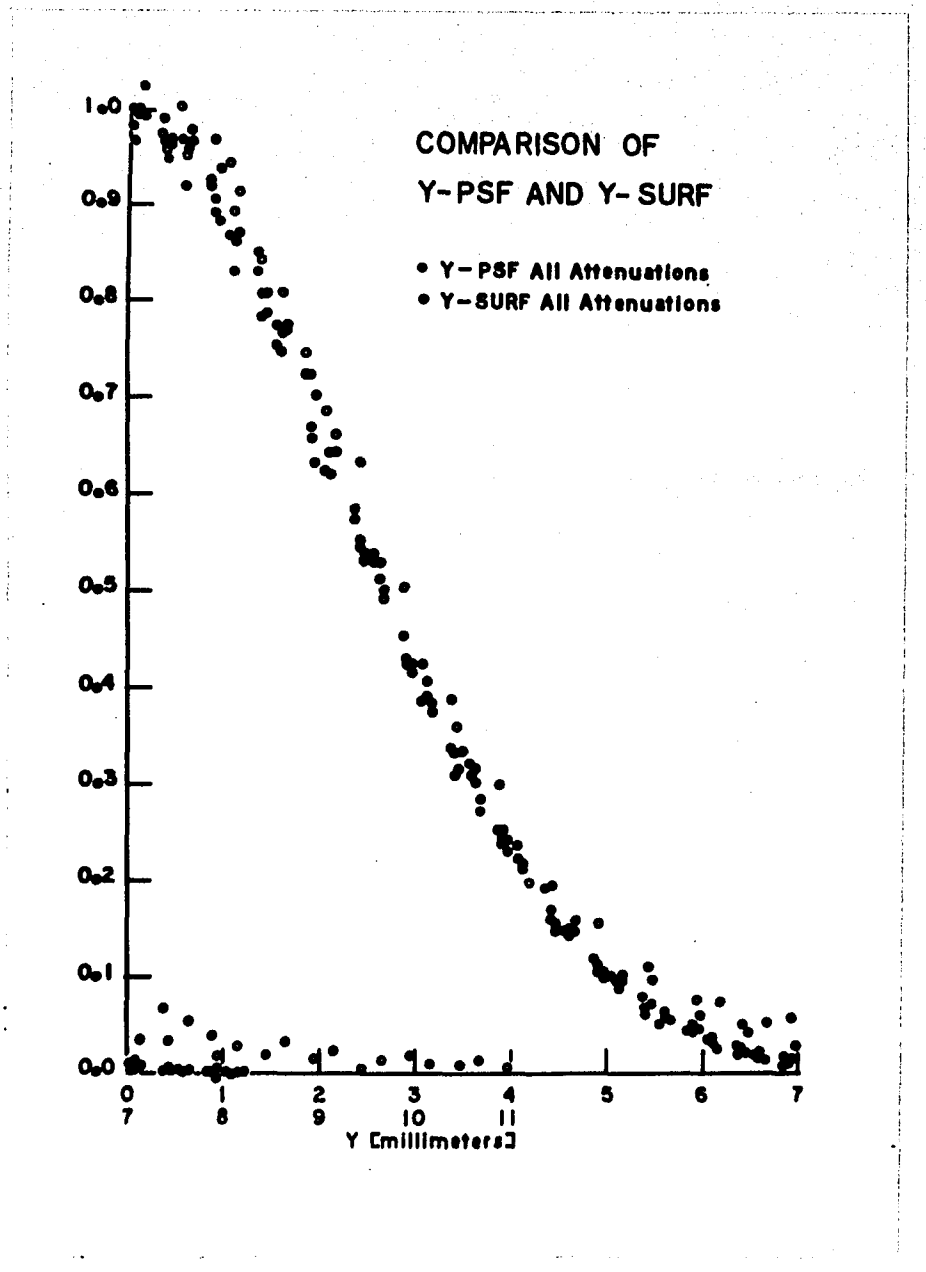

Figure 32. The PSF and SURF for all attenuations are compared for the Y direction. The shapes of the PSF and SURF appear similar except for the larger tail of the Y-SURF.

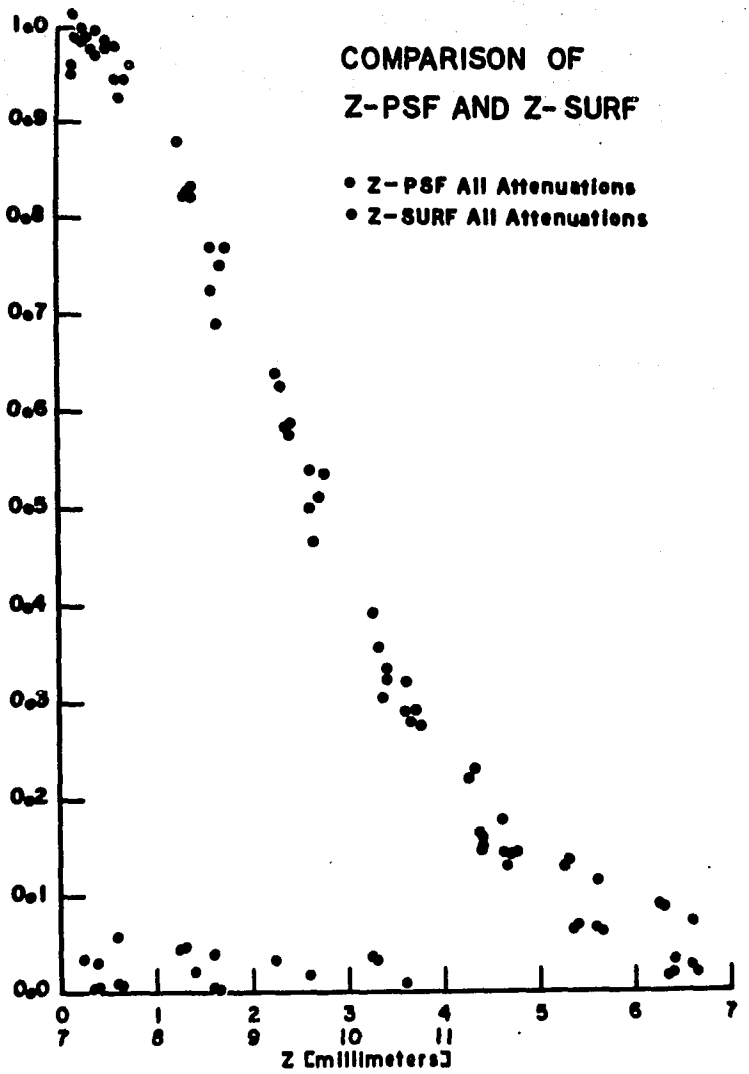

Figure 33. Same as Fig. 32 but for the Z direction.

Figs. 28, 29, and 30. Table 5 reviews the parameter "a" in the gaussian fit used for PSFs and SURFs in various directions and with various thicknesses of attenuating tissue equivalent media.

The least square fit was done using only data greater than 10% of the maximum. It is clear from Figs. 24, 25 and 26 that the PSFs fit the gaussian form quite well; however, it appears from Figs. 28, 29 and 30 that the tails of the SURFs are greater than those of the gaussian fit. This represents a measure of the limitations on the assumptions that there is separability of variables and ellipsoidal symmetry for the FCCS system.

B. Resolution and Sensitivity in Phantom Studies

1. Scan of Volume Phantom Containing a Cold Lesion

a. Resolution

In order to examine the capability of the system for cold lesion detection, phantoms consisting of cold spherical defects imbedded in a homogenous radioisotope distribution were employed. The six sides of the phantom were made of 1/8" thick polystyrene. The central cold defect was formed using a 6 mm diameter artificial plastic pearl epoxied to a glass fiber fixed at diagonally opposite corners of the rectangular phantom. The phantom was put in a collar of solid polystyrene and scanned in the geometry indicated in Fig. 11 using the circuitry of Fig. A.1. The collar insured that the gamma ray attenuation would be uniform for the transverse scanning directons. About 240 μCi of ^{75}Se in the form of selenomethionine in water was injected into a small filling port which was then sealed.

TABLE 5

GAUSSIAN CONSTANTS "a" IN $\exp-(X/a)^2$ FOR

LEAST SQUARES FITS (NORMALIZED)

Attenuation In Z-Direction	Symbol	Gaussian Constant "a" (millimeters)					
		X-PSF	X-SURF	Y-PSF	Y-SURF	Z-PSF	Z-SURF
air	o	2.21	2.11	3.26	3.30	3.13	--
0 mm (backscatter)	●	2.17	--	3.23	--	3.19	3.31
15 mm	†	--	2.14	--	3.33	--	3.42
20 mm	×	2.12	--	3.20	--	--	--
35 mm	△	--	2.15	--	3.43	--	3.37
40 mm	▲	2.17	--	3.19	--	--	--
all attenuations (average)	^ o ●	2.17	2.13	3.22	3.35	3.16	3.37
single gamma	△ ▲	3.31	7.41	4.87	76.70	--	--

About ten weeks after the phantom was made the small globs of epoxy which secured the artificial pearl to the glass fiber and the ends of the fiber to the phantom corners, began to change color; transparent to slightly yellow. At this time the corners of the phantom were scanned, and it was apparent that the ^{75}Se was concentrating in the epoxy globs. By accident, then, a phantom designed to consist of one small 6 mm diameter cold lesion in the center of a uniform activity of 7.5 μCi of ^{75}Se per ml of water became a much more complex and challenging phantom with a small cold lesion in contact with two small hot lesions imbedded in a uniform activity. Furthermore, by inspecting the phantom it could be seen that one of the epoxy globs near the pearl was much larger than the other one. The phantom is schematically indicated in Fig. 34.

A tomographic scan of the phantom was made by manually translating the system focal region 2 mm at a time in each of the three major directons. Both coincident counts and summed single gamma values were obtained for each (X-Y-Z) position. The coincidence values were corrected for background, Chance (or "false") coincidence due to the finite 55 ns resolve time, and for the variation in attenuation with depth.

A 12 mm x 14 mm x 18 mm region (560 lattice points) centered about the cold lesion was scanned. The resulting minimum count was about 53% of the maximum count and integral values from 1 to 9 were assigned to counts between the extreme values. This represents a contrast enhancement of 53%. Figure 35 shows the scan results

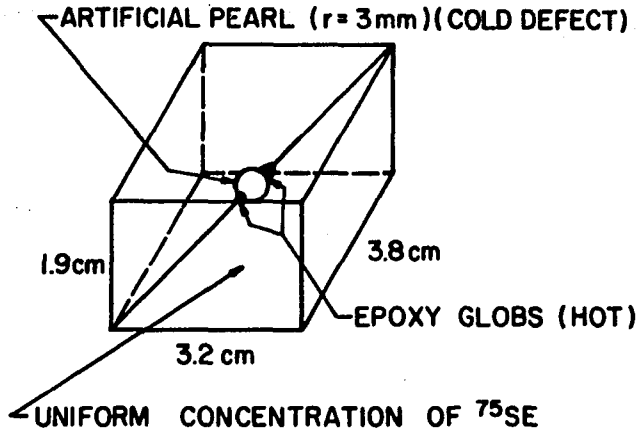

Figure 34. The rectangular solid phantom with internal dimensions 3.8 cm x 3.2 cm x 1.9 cm containing a solution of 7.5 μCi/ml of ^{75}Se in water and a central plastic pearl 6 mm in diameter. Two epoxy "globs" hold the pearl onto a glass fiber which is along the diagonal of the phantom. The "globs" were found to differentially concentrate radioisotope hence appear "hot".

raphically displayed so that the integers 1 to 9 are represented by gradually darker boxes. Note that for purposes of visualization the 2 mm unit scanning intervals in each of the X, Y and Z directions are represented by different lengths.

Fig. 35 indicates the following: (a) There is a definite cold lesion probably centered slightly below plane 3. (b) The lesion appears wider in the Y and Z directions than in the X direction. (c) The activity of thephantom appears to decrease for planes above plane 6 and for planes below plane 1. (d) There is a hint of a hot spot centered between planes 3 and 4 just to the upper right of the cold lesion.

The above observations will now be interpreted. The cold lesion in the center of the display corresponds to the artificial pearl, and its dimensions in Fig. 34 of between 6 mm and 9 mm are consistant with the actual dimensions of the 6 mm pearl and the smearing surface source response functions ($\sim$5 mm wide). The asymetrical, apparent 6 mm width in the X direction arises from the fact that the X step response function is sharper than the Y or Z step response functions. This result can also be understood in terms of the coincidence isoresponse oblate spheroids whose axes are smallest in the X direction. The reduced activity of planes 0 and 7 (14 mm apart) corresponds to the fact that the phantom is only about 19 mm in the Z direction, and the coincidence sensitive volume extends outside the phantom. Finally the position of the hot spot next to the cold lesion corresponds exactly to the position of the larger epoxy glob next to

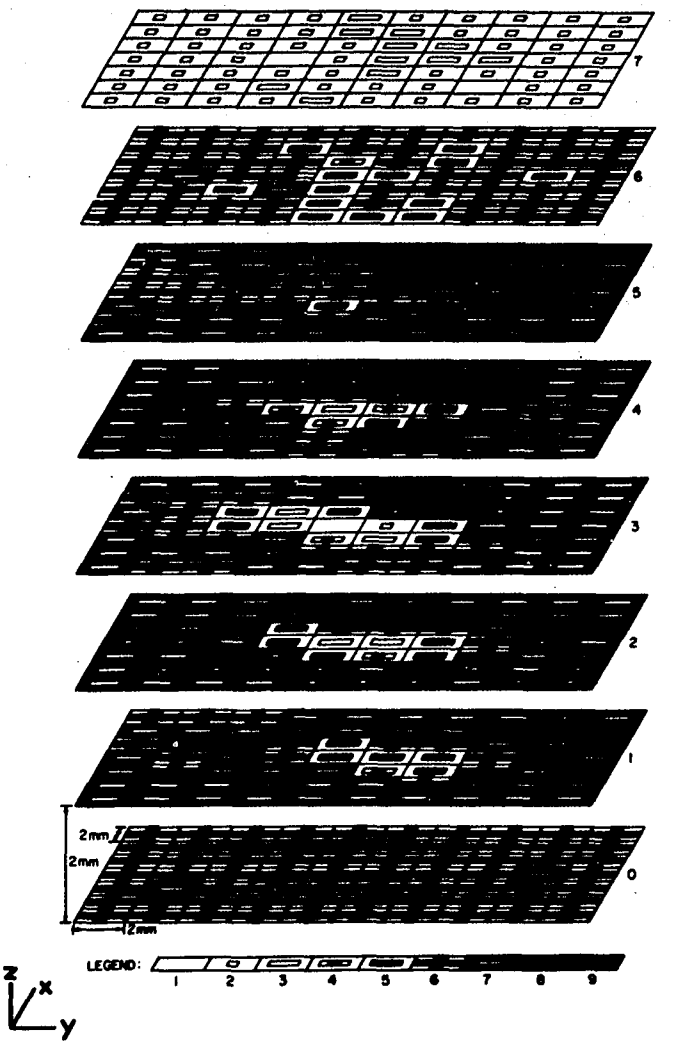

Figure 35. The result of an FCCS scan by the two-perpendicular-detector system of the phantom of Figure 34. Darker regions represent increased isotope uptake. The central spherical defect is readily visualized. The planes are 2 mm apart and each picture element is 2 mm x 2 mm.

the pearl in the phantom. Thus it appears that an accurate tomographic representation of a three dimensional radioisotope volume distribution with a resolution of a few millimeters has been obtained.

In order to compare the coincidence response to the summed single gamma response, the latter was similarly plotted. Figure 36 shows such a display where the contrast enhancement is now 78%. A clearly defined cold lesion is not apparent let alone an adjacent hot spot; however, all values on plane 3 appear depressed. The total activity of the phantom appears to decrease much more rapidly in the $\pm$ Z directions than it did in Fig. 35. In fact it is hard to conclude that there is a relatively uniform isotope distribution in the phantom at all. This is no doubt due to the very wide single gamma surface source response functions in all the directions.

b. VID and Sensitivity

Some mention should be made of the absolute values of the coincidence rates and VIDs found in the above phantom study. It should be emphasized, however, that the main objective in these studies was to obtain the highest three dimensional resolution possible without regard to clinically realistic scanning requirements. Later a discussion will be made to show how clinically realistic parameters can be extrapolated from these results. The average summed single gamma count densities used in this work for scanning the phantom of Fig. 34 was of the order of 5 million counts per cm^3. The average maximum coincidence scanning information density used was about 50,000 true counts per cm^3. The average time for scanning each

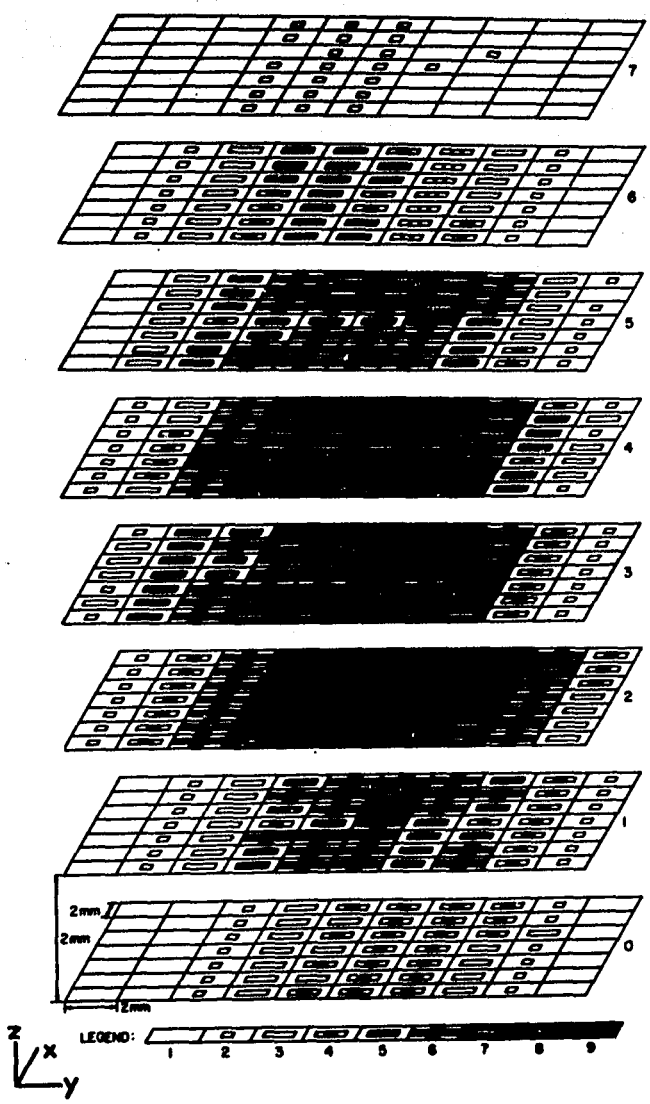

Figure 36. The result of a summed single gamma scan by the two-perpendicular-detector system of the phantom of Figure 34. The central spherical defect is not visualized.

12 mm x 18 mm plane was about 3 hr. The statistical coincidences varied between about 10 and 20 per cent of the true count rate.

2. Scan of Volume Thyroid Phantom Containing Various Lesions

As a step toward clinical scanning, a standard thyroid phantom as illustrated in Fig. 37, with a concentration of about 5 $\mu Ci/cm^3$ of ^{75}Se was scanned. The same system as above was used except that by using the circuit of Fig. A.3. both probes could now accept both the 135 keV and the 265 keV gamma rays. The system sensitivity was therefore doubled. The scan field was increased to planes of X-Y dimensions 7.2 x 8.0 cm. The maximum VID was reduced to about 1700 counts/cm^3. The lattice spacing in each direction was increased to 4 mm with a counting time per plane of 2 to 3 hr.

The scan results of successive planes are presented in Figs. 38 to 45 and each data point has been corrected for attenuation and physical decay but not for background or chance coincidences. The latter are together less than 10% throughout the three dimensional scan. Figures 38 to 45 show clearly all the basic depth features of the phantom as well as all the cold lesions, and in general indicate the depth discrimination capabilities of the FCCS system in "slicing-up" a phantom only 1.9 cm thick.

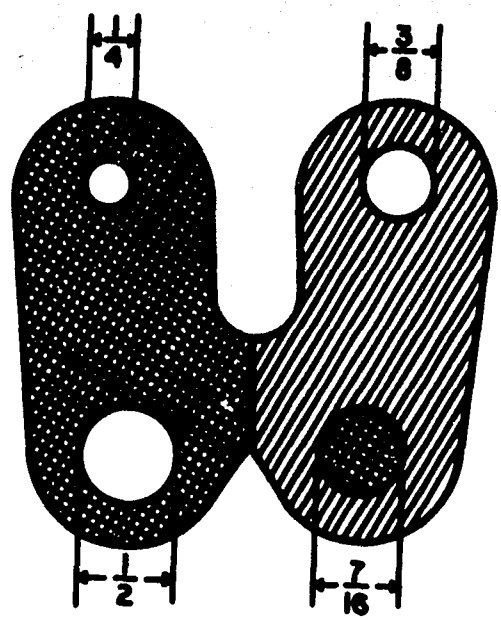

Figure 37. Schematic projection of the standard thyroid phantom where dark cross-hatched regions indicates presence of radioisotope activity and white regions indicate no radioisotope throughout the depth (into plane of figure) of the phantom. Lightly cross-hatched region indicates that only half the thickness of the phantom contains radioisotope (the deeper half). The phantom is 19 mm thick inside with about 3 mm thick walls outside. Dimensions in figure are in inches.

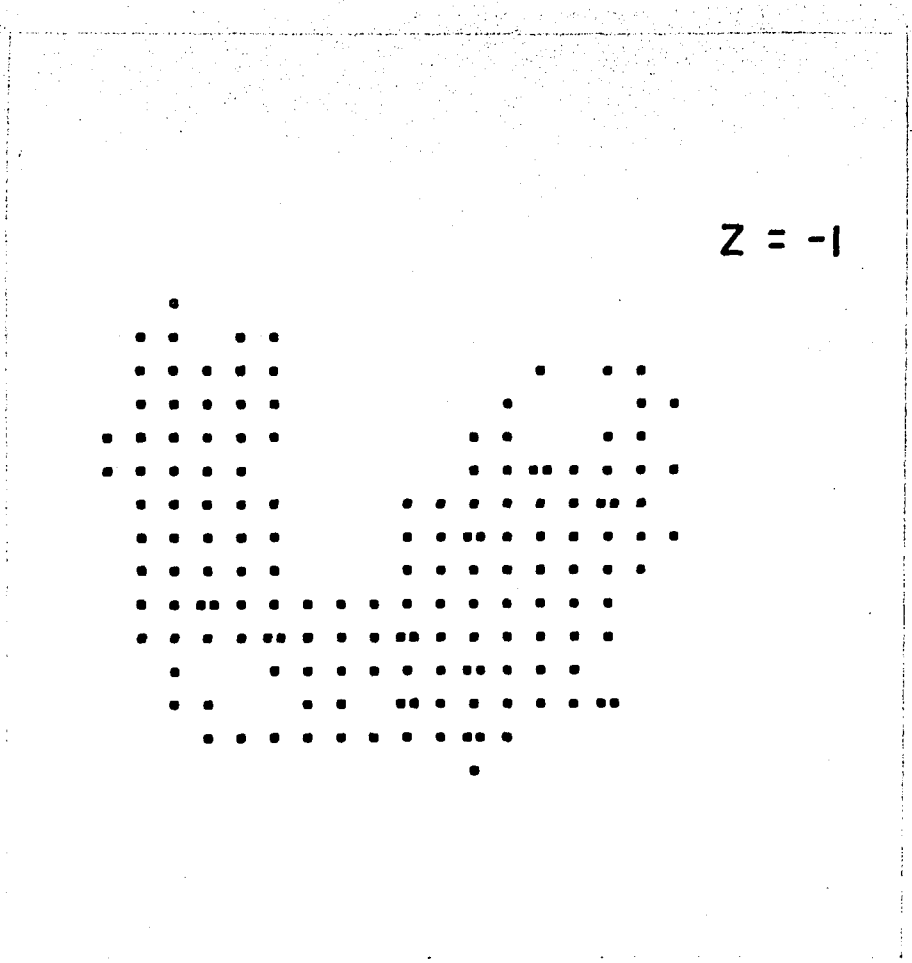

Figure 38. Results of the scan of the standard thyroid phantom for Z=-1 mm where positive Z-values indicate greater depth into the phantom scattering material (more attenuation). Each data point taken 4 mm apart in the X and Y directions is represented by a 5 x 5 unit^2 region where 0 to 25 unit squares are darkened depending upon the activity detected.

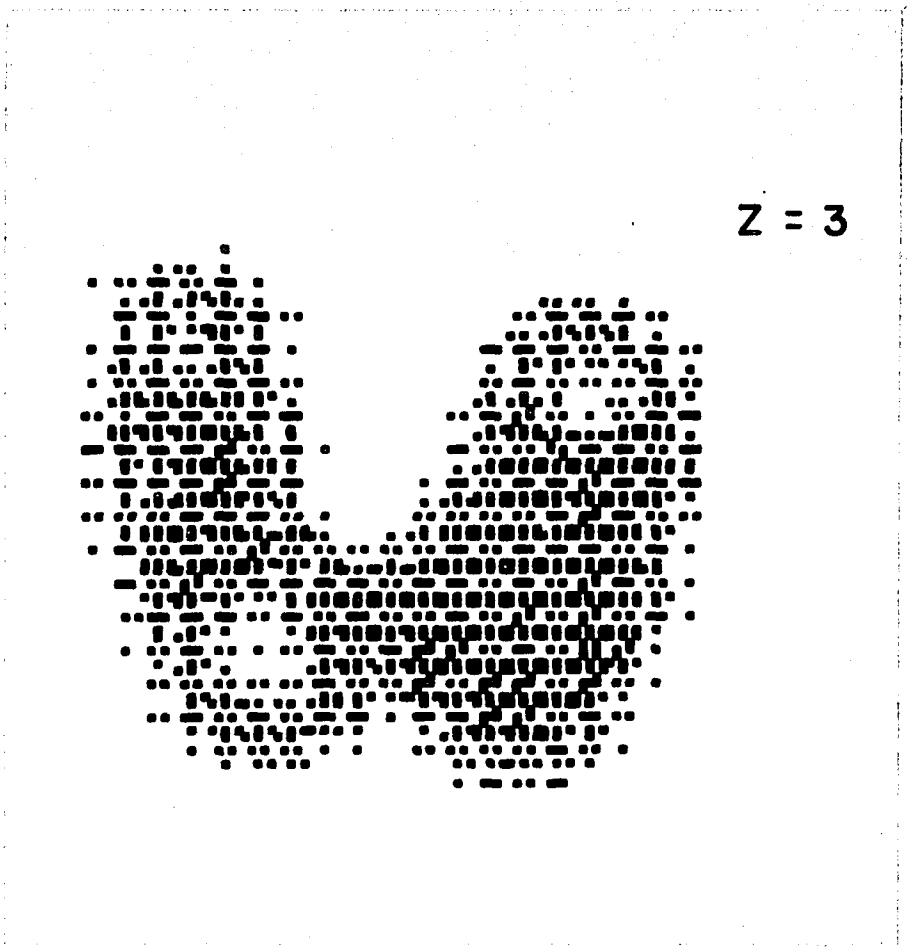

Figure 39. Same as Fig. 38 but Z = 3 mm.

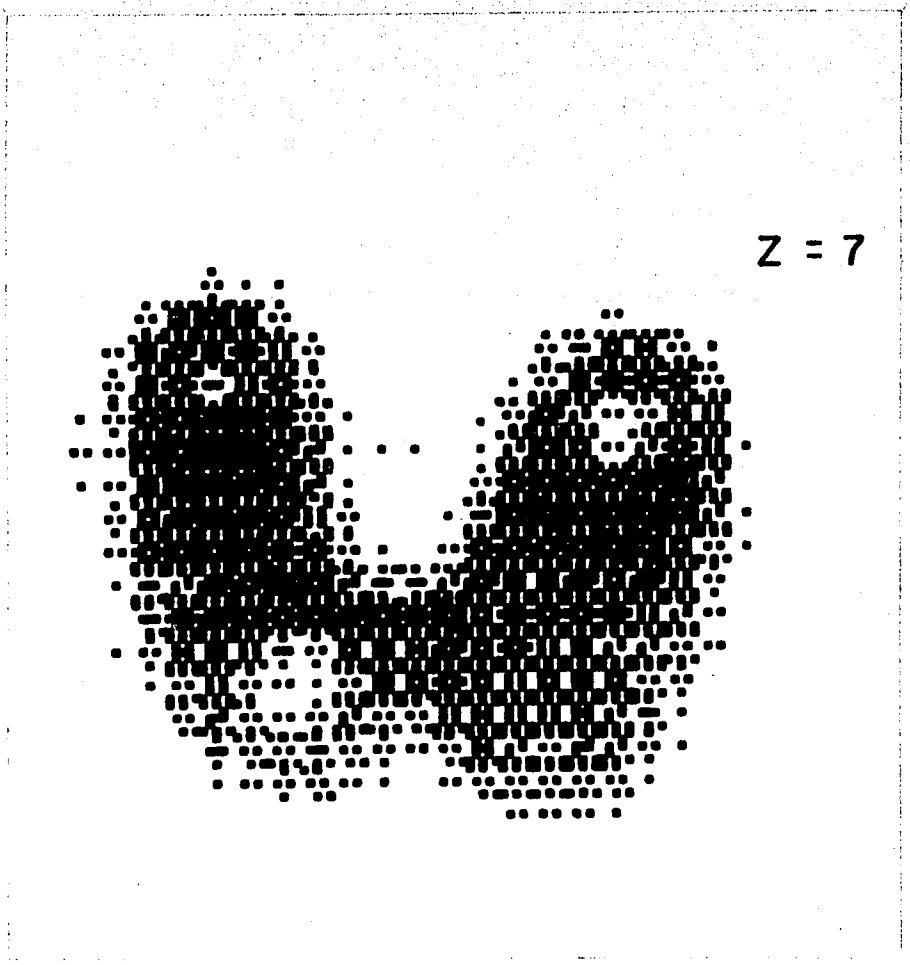

Figure 40. Same as Fig. 38 but Z = 7 mm.

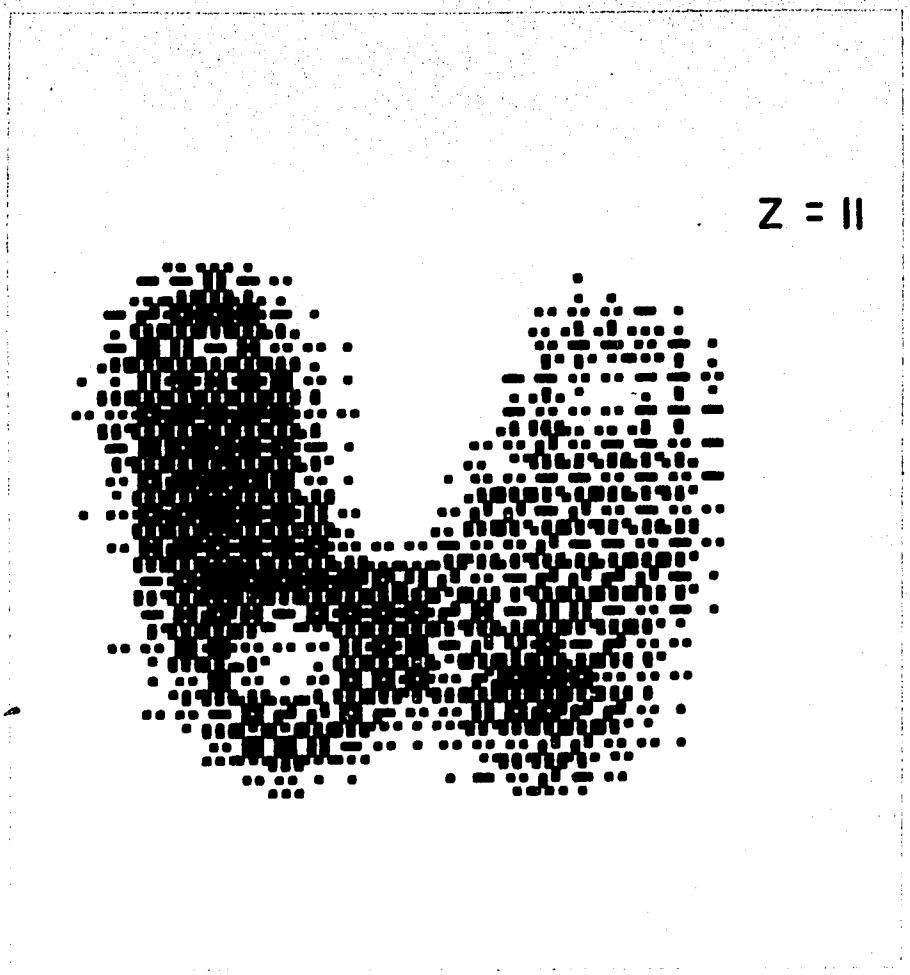

Figure 41. Same as Fig. 38 but Z = 11 mm.

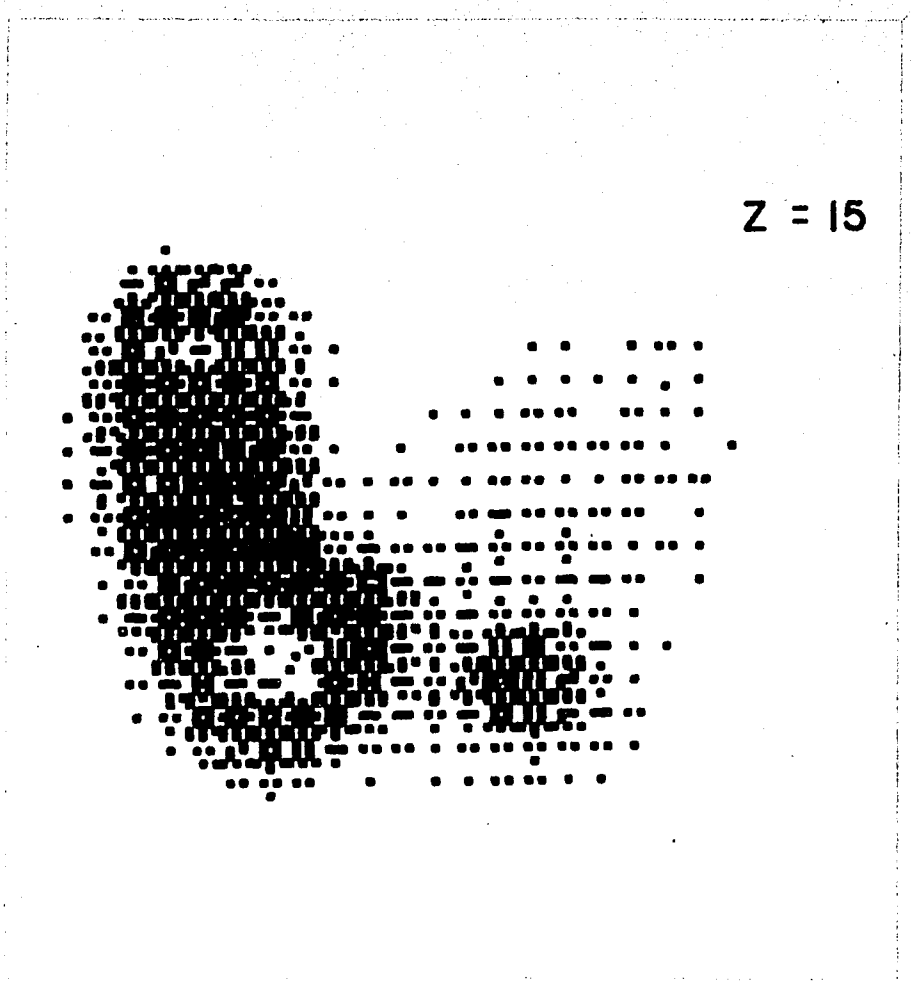

Figure 42. Same as Fig. 38 but Z = 15 mm.

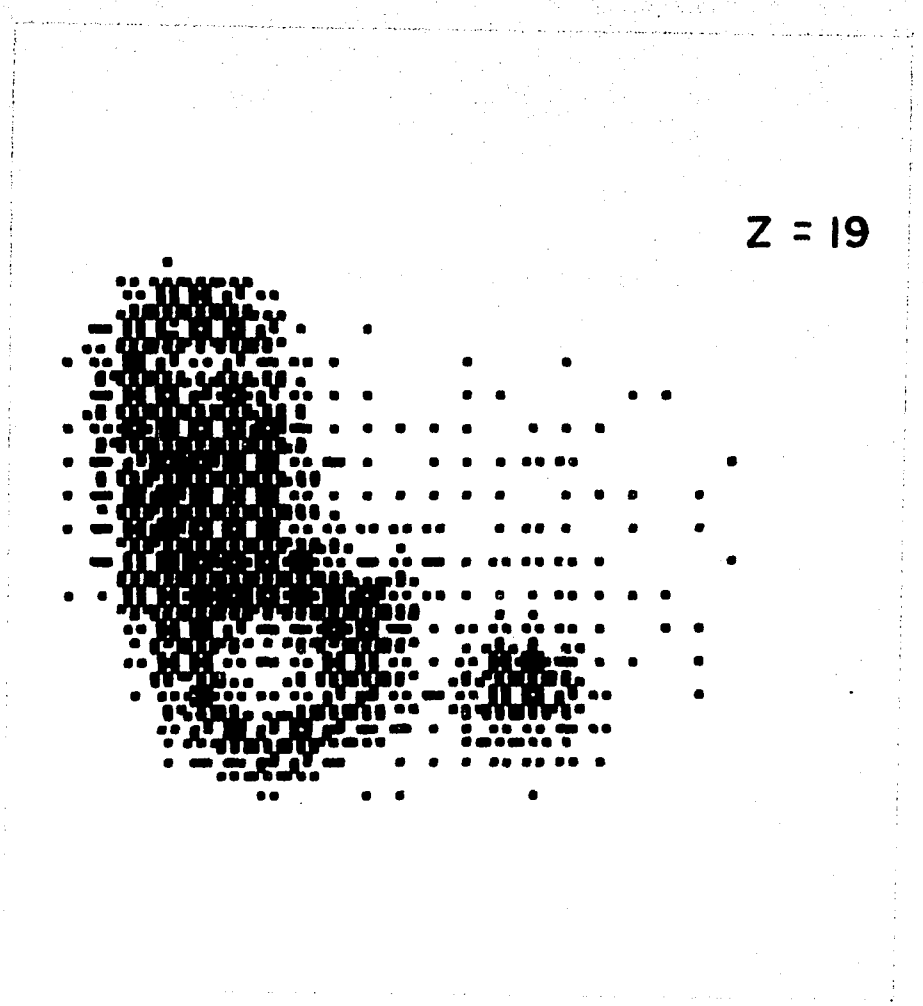

Figure 43. Same as Fig. 38 but Z = 19 mm.

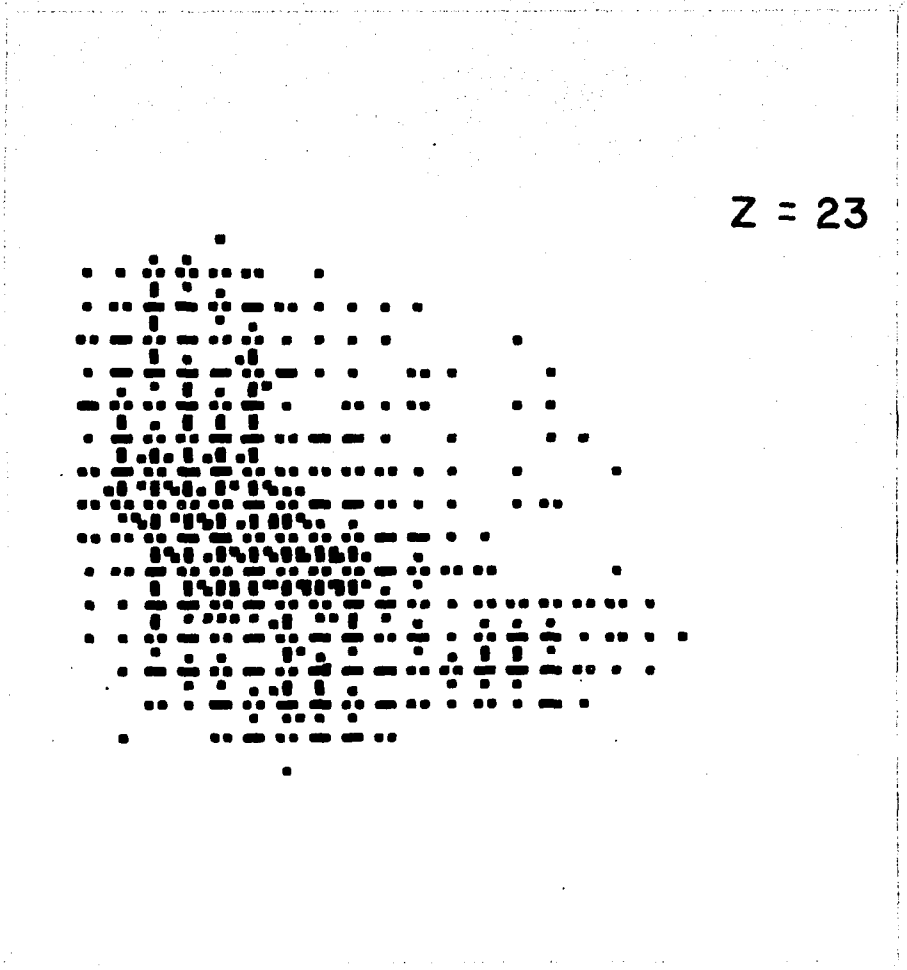

Figure 44. Same as Fig. 38 but Z = 23 mm.

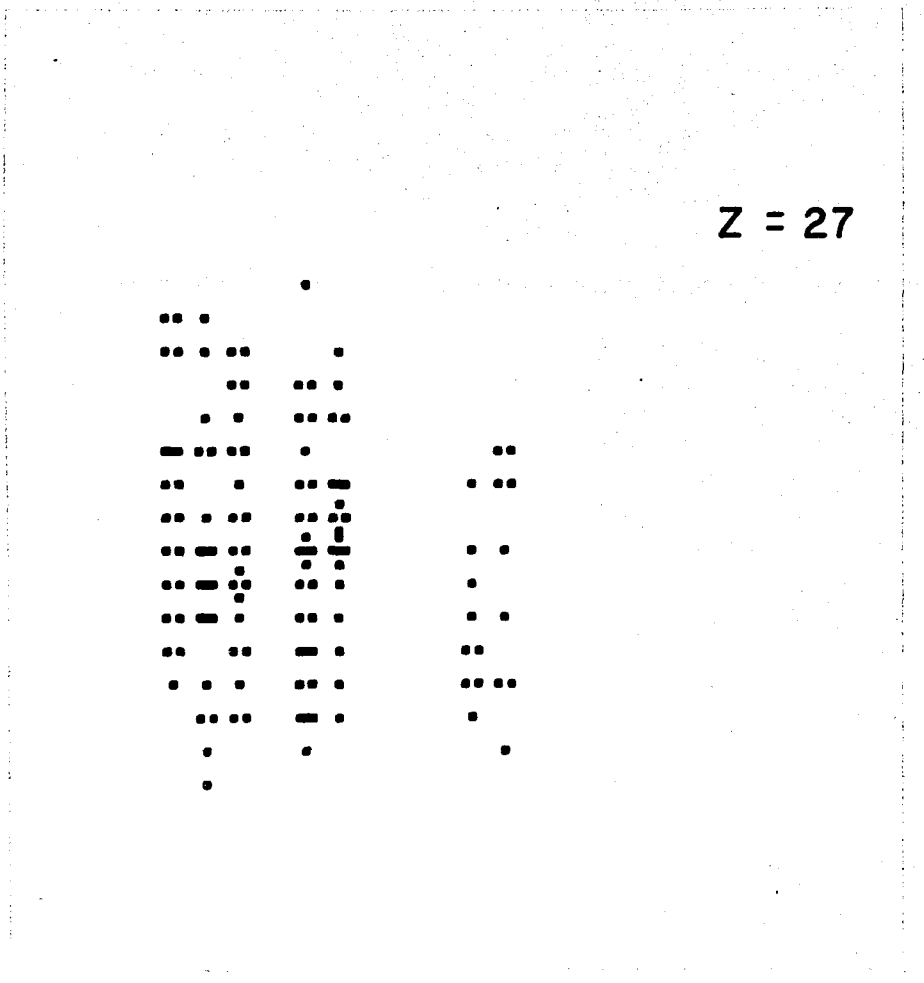

Figure 45. Same as Fig. 38 but Z = 27 mm.

CHAPTER VIII

CLINICAL APPLICABILITY OF FCCS

A. Areas of Applicability

The FCCS system used in the studies of Chapter VII Part B.2 was designed for as high a tomographic resolution as possible without much regard for the clinical usefulness of the specific system. The result was a system with lower count rate sensitivity and perhaps higher spatial resolution than required for a clinically useful device. There are many straight-forward ways in which the system sensitivity can be increased. These methods, which will be discussed more fully in Part B of this chapter, include instrument and radionuclide-related factors such as increasing the number of probes, increasing the collimator efficiencies, and using short half-lived radionuclides which have more than two coincident gamma rays and which have higher energies for reduced attenuation. In addition, the geometric factor of increasing the size of the focal region (degrading the resolution) can increase the focal coincidence count rate.

In the development of specific applications using FCCS consideration must be given not only to its ability to provide information of clinical importance, but also to the relative effectiveness of FCCS in comparison with other techniques. The experimental results here obtained suggest that FCCS may be the method of choice when tomographic high spatial resolution ($< 1\ cm^3$) is indicated. The classes of application immediately suggested are:

a) small organ scanning

b) small regions of interest within a large organ

c) determination of local dynamic function for a clearly defined volume within an organ.

Appropritate adaptations of system design, isotope selection and tissue distribution (using a variety of radioisotope tagged compounds) are required for specific organ applications. A variety of these special applications ranging from prostate and thyroid scanning to the quantitation of cerebral blood flow are being investigated.*

It should be noted that a certain flexibility exists in carrying out the dynamic measurements (c) since the focal region can be adjusted by simple geometric means such as collimator selection. If it is necessary to monitor a very small region, a high resolution system would be used; for monitoring a larger volume, lower resolution collimators would be used with a resulting increase in the experimental count rate and so the statistical reliability.

The area of large organ or body section tomography in nuclear medicine is under rapid development. Most of the promising technqiues involve acquisition of data from a large tissue volume with subsequent computer analysis. The role of FCCS in this general area of large organ tomography will dpened upon the additional choices of isotopes it allows, the geometric orientation of the scan sections provided, and

*Aspects of instrumentation are now being actively worked on by Prof. H.E. Hart and graduate students, P. Spetsieris and P. Zacuto, and tissue distribution studies are being carried out in collaboration with Prof. B. Rosoff.

the relative insensitivity of FCCS to physiological motion because of its direct spatial nature (Chapter III). For large organ scanning all of the sensitivity factors (instrument, radioisotope, and geometry-related) would have to be used in order to do tomographic scans in clinically realistic times using FCCS. The design of such a system using commercially available collimators is considered in detail in Part B of this chapter.

B. FCCS System Designs

1. General Dependences of Signal and Noise Upon System Parameters

In order to construct a clinically useful FCCS system some extrapolations can be made from two probe systems used in this work. In considering these larger systems the signal, S, which is the true coincidence rate μ_2, will be evaluated and compared to the noise, N_o , which is the chance coincidence rate C_c. The following equations obtained from information and definitions reviewed in Table 1 will be used in addition to Table 1 in order to determine the effect of parameters upon the single gamma count rate, ν_1, the signal, S, and the signal to noise ratio ($S/N_o = \mu_2/C_c$).

$$\nu_1 = e_1 D v \tag{8.1}$$

$$S = \mu_2 = e_1\left(\frac{\alpha}{v}\right)\nu_1 = e_1^2 D\alpha \tag{8.2}$$

$$\frac{S}{N_o} = \frac{\mu_2}{C_c} = \frac{e_1}{2\tau\nu_1}\left(\frac{\alpha}{v}\right) = \frac{1}{2\tau D}\left(\frac{\alpha}{v^2}\right) \tag{8.3}$$

The parameters upon which S and (S/N_o) depend can be divided into three groups: instrument-related, geometric, and isotope-related. These are reviewed in Table 6 along with their effects upon ν_1, S, and (S/N_o). Among the instrument-related parameters are the number of probes N_p, the coincidence resolve time τ, the number of gamma energies detectable per probe, γF, and the probe efficiency. It can be seen, for instance, that the true coincidence rate, μ_2, increases as the number of detector probe pairs, $N_p(N_p-1)/2$. Improved (decreased) resolve time helps increase (S/N_o). The number of gamma energies detectable per probe for ^{75}Se is either 1 as for the system using the circuit of Fig. A1, or 2 as for the system using the circuit of Fig. A3. The relative probe efficiency, EF, was indicated in Table 6 for the convenience of future comparisons; however, its effect on ν_1, S, and (S/N_o) were obtained from the dependence of ν_1, and μ_2 upon e_1, the absolute collimator focal efficiency, determined from equations (8.1) and (8.2). In general, it can be seen in Table 6 that the improvement of instrument parameters, except τ, increases the signal without changing the signal to noise ratio (or the spatial resolution), whereas decreasing τ improves the signal to noise ratio without changing the signal.

Among the geometric parameters are the previously defined focal and single channel volumes, α and ν, as well as a linear gauge of the focal volume size, d, which would be related to the FWHM of the PSF. The source thickness in the Z direction, L_Z, effects the single gamma

TABLE 6

SIGNAL AND S/N DEPENDENCES

Dependence		μ_1	$S=\mu_2$	$S/N=\mu_2/C_c$
Instrument parameters:				
N_p	no. probes (↑)	--	$N_p(N_p-1)/2$ (↑)	--
γ	resolve time (↓)	--	--	γ^{-1} (↑)
γ_F	no. gamma energies detectable per probe logic circuit (↑)	γ_F (↑)	γ_F (↑)	--
EF	relative probe efficiency (↑)	EF (↑)	$(EF)^2$ (↑)	--
Geometric parameters:				
L_z	source thickness (↑)	L_z (↑)	--	L_z^{-2} (↓)
d	focal region diameter (↑)	d^2 (↑)	d^3 (↑)	d^{-1} (↓)
α	focal volume $\sim d^3$ (↑)	$\alpha^{\frac{2}{3}}$ (↑)	α (↑)	$\alpha^{-\frac{1}{3}}$ (↓)
v	single channel volume $\sim d^2 L_z$ (↑)	v (↑)	--	v^{-2} (↓)
Isotope-related parameters:				
D	concentration (↑)	D (↑)	D (↑)	D^{-1} (↓)
n_c	no. gamma rays per cascade ($\gamma_F=2$) (↑)	$n_c/2$ (↑)	$n_c(n_c-1)/2$ (↑)	$2-2/n_c$ (↑)
Att	source attenuation factor per gamma ray (↑)	Complex	$(Att)^2$ (↑)	Complex

count rate, γ_1, because it depends upon $\mathcal{V}$ which is defined as the intersection of the collimator single channel field of view with the source. Thus as the source thickness, L_Z, increases, so will $\mathcal{V}$ and hence γ_1. For the present discussion the effect of attenuation due to patient thickness is grouped under isotope-related parameters since the attenuation is gamma ray energy dependent. In general, as indicated in Table 6, the signal can be increased by changing the geometric parameters but only at the sacrifice of spatial resolution and signal to noise ratio.

Among the isotope-related parameters are the concentration D, the number of gamma rays per disintegration, n_c, and a complicated attenuation factor dependent upon the energies of the gamma ray emissions. An increase in D can improve the signal but only with a decrease in signal to noise ratio. By using an isotope with many coincident gamma emissions per disintegration, an improvement in S and somewhat in (S/N_o) can be accomplished. Finally, the effect of attenuation in the patient upon S and (S/N_o) is complex although assuming uniform patient thickness, the signal is roughly decreased by the product of exponential attenuation factors for each of the two coincident gamma rays for each valid event (regardless of n_c).

2. Collimator Changes For Two Probe FCCS System

As an example of increasing FCCS system sensitivity (and degrading resolution) by using broader focusing collimators, two commercially available collimators were substituted for the high resolution BNL collimators used for the studies of Chapters V and VII.

A factor of about 27 in increased focal volume can be obtained by using Raytheon Model HC100/18B collimators. These collimators were designed for scanning gamma rays up to 600 keV in energy. They have about the same length from the face nearest the detector crystal to the focal point, 7 in. Although the FWHM of the single gamma PSF is about 3 times that of the experimental high resolution BNL collimators used in the work of previous sections, the point source focal efficiency, e_{ci}, is less than that for the BNL collimators. A comparison of the properties of the two types of collimators is reviewed in Table 7. For a two probe system, the increase in sensitivity should be about a factor of 10, not including tissue attenuation effects.

A two probe system having the electronics of Fig. A3 with the new collimators was used to scan the thyroid phantom of Fig. 37. Figures 46 and 47 show the results for two planes 8 mm apart, near the center of the phantom. Although as might be expected, much of the detail is lost, a difference between the planes can still be perceived. The upper part of the right lobe appears to have less activity for the deeper plane (greater Z) while the lower part of the right lobe and the whole left lobe appear unchanged. This reflects the fact that in this phantom the right lobe has no radioisotope in half the phantom thickness (the deeper half, with greater Z) except for the 7/16" diameter "hot" lesion which goes through the whole thickness of the phantom. The left lobe, however, is identical throughout the thickness of the phantom. In addition, although the upper half of the right lobe

TABLE 7

COLLIMATOR PARAMETERS

PARAMETER		Raytheon HC 100/18B	BNL
N/2	number of channels	19	1507
F	focal length (inches)	3.9	4.6
t	thickness (inches)	3.2	2.5
F + t	(inches)	7.1	7.1
FWHM	(mm)	18	6
$\propto$	focal volume (cm^3)	2.1	0.08
VF	ratio of focal volumes	27	1
e_{ci}	focal efficiency (%)	38	63
EF	relative efficiency	0.6	1.0
$(EF)^2$	relative coincidence efficiency	0.37	1.0

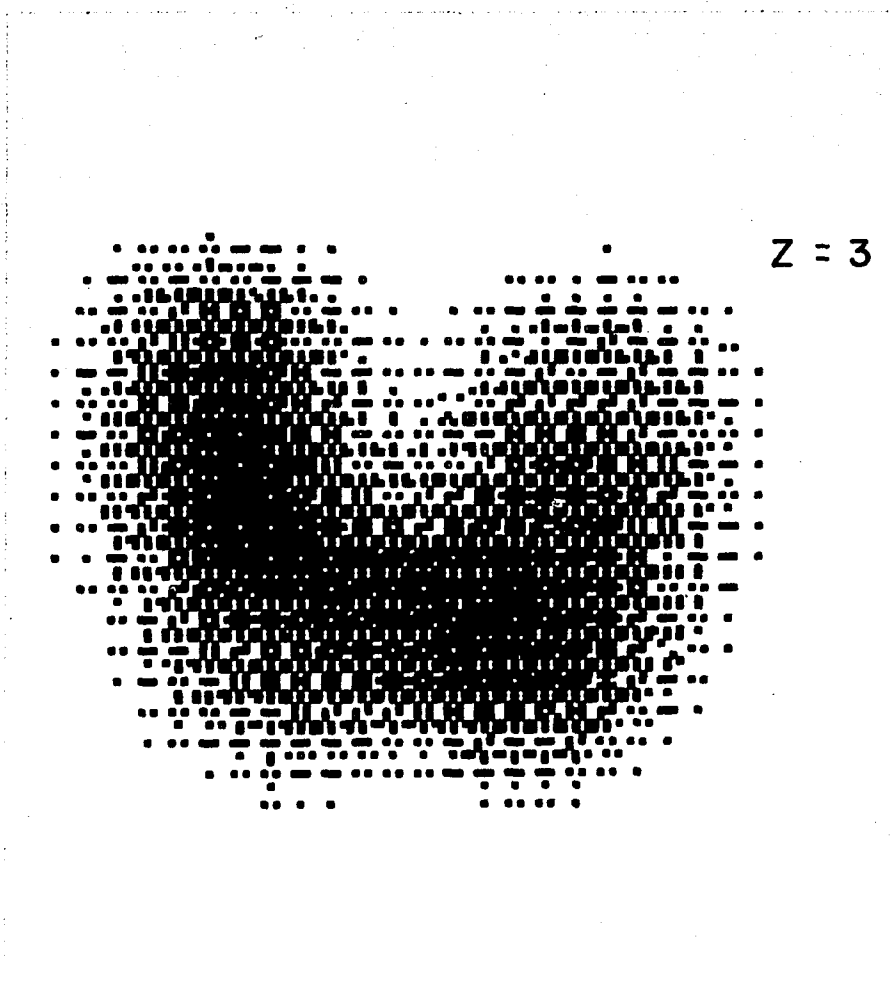

Figure 46. Results of the scan of the thyroid phantom Z = 3 plane using a two probe FCCS system having commercial broad focused collimators. Although the spatial resolution is not as good as that of the system using the BNL collimators, still the decrease of activity in the upper part of the right lobe with depth can be seen as an indication of the two right lobe lesions.

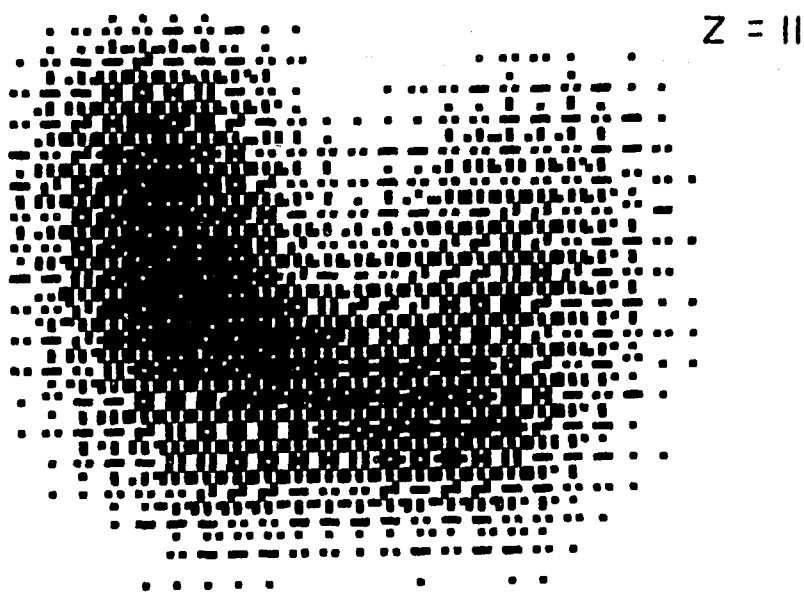

Figure 47. Same as Fig. 46 but Z = 11.

of the scan in Fig. 46 appears to have more activity, the very top of the right lobe is still colder than the top of the left lobe. This occurs in the same region as the 3/8" diameter cold lesion of the phantom.

The scans could not easily be corrected for attenuation because as contrasted with the case when using high resolution BNL collimators, the attenuation varied significantly through the enlarged focal region. This would also in part explain why only an increase in system sensitivity, of about 6 times was recorded while scanning the thyroid phantom. In addition, the width of the phantom is only 1.7 cm, less than the 1.8 cm FWHM of the Z-PSF for the system with the changed collimators. For a practical system, then, it would seem necessary to use a higher energy emitting isotope so that the attenuation changes across the focal region would be small.

3. Comparison of Multi-Probe FCCS Systems and Design of Large Organ Scanning System

In order to provide a quantitiative illustration of the effects of some of the sensitivity factors discussed in Part B.1 above, a system was designed using the commercial collimators described in Part B.2 above for scanning large organs such as the liver. In order to see the evolution from the two probe high resolution system used for the studies of Chapter V and VII to the six probe large organ scanning system a number of specific FCCS system configurations are listed in Table 8. There are five different device configurations

numbered 1 through 5 in order of increasing size and sensitivity. The scanning parameters used with system 1 are identical to those used in scanning the phantom with spherical defect of Chapter VII, Part B. The scanning parameters used with system 2 approximate those used in scanning the thyroid phantom of Chapter VII, Part B. The scanning parameters used with system 3, where broader focused commercial collimators replace the fine focus BNL collimators, are the same as those used in scanning the thyroid phantom in Chapter VIII, Part B except that the proposed source thickness has been changed to 10 cm more comparable with large organs. There is, therefore, a consequent increase in $\mathcal{V}$ and $\mathcal{V}_1$ and decrease in (S/N_o). In addition, a range of picture element sizes (2 to 5 mm) has been given with a 5 mm distance between transverse planar scans, d_z. The relative focal volume, α_{rel}, and single channel volume, $\mathcal{V}_{rel}$, have been listed in order to compare the systems using the commercial collimators with the systems using the BNL collimators. For system 3, comparisons are made for two isotope concentrations, 5 μCi/cc (system 3), used in the thyroid phantom studies, and 1 μCi/cc (system 3'), a more clinically realistic concentration. In system 4 and 5 only the number of probes has been increased to 5 and 6 respectively, and finally a comparison is made for system 5 using an order of magnitude lower isotope concentration (system 5').

The sensitivities of the five systems are compared in Table 9. The total relative sensitivity factor SF is the product of

TABLE 8

SCANNING PARAMETERS

Device Configuration:	(1)	(2)	(3)	(3')	(4)	(5)	(5')
Circuitry:	Fig.A1	Fig.A3	Fig.A3	Fig.A3	Fig.A7	Fig.A7	Fig.A7
Collimators:	2 BNL	2 BNL	2 Ray.	2 Ray.	5 Ray.	6 Ray.	6 Ray.
Parameter							
d_x picture element size (cm)	0.2	0.4	.2-.5	.2-.5	.2-.5	.2-.5	.2-.5
N_x no. data locations	10	25	50-20	50-20	50-20	50-20	50-20
L_x $N_x d_x$, x-distance scanned (cm)	2.0	10	10	10	10	10	10
d_y picture element size (cm)	0.2	0.4	.2-.5	.2-.5	.2-.5	.2-.5	.2-.5
N_y no. data locations	5	25	50-20	50-20	50-20	50-20	50-20
L_y $N_y d_y$, y-distance scanned (cm)	1.0	10	10	10	10	10	10
d_z distance between scan planes (cm)	0.2	0.4	0.5	0.5	0.5	0.5	0.5
L_z thickness of source (cm)	1.9	1.9	10	10	10	10	10
A $L_x L_y$, area scanned (cm^2)	2.0	100	100	100	100	100	100
D concentration ($\mu Ci/cm^3$)	7.5	5.0	5.0	1.0	1.0	1.0	0.1
$\frac{(\alpha)}{(\nu)_{exp}} = \frac{\mu 2}{e_1 \nu_1 (\gamma F)(N_p F)}$	0.10	0.10	0.06	0.06	0.06	0.06	0.06

TABLE 8 CONT.

SCANNING PARAMETERS

Device Configuration:	(1)	(2)	(3)	(3')	(4)	(5)	(5')
Circuitry:	Fig.A1	Fig.A3	Fig.A3	Fig.A3	Fig.A7	Fig.A7	Fig.A7
Collimators:	2 BNL	2 BNL	2 Ray.	2 Ray.	5 Ray.	6 Ray.	6 Ray.
Parameter							
α focal volume (cm^3)	0.08	0.08	2.1	2.1	2.1	2.1	2.1
α_{rel} relative focal volume	1	1	27	27	27	27	27
ν_{rel} relative single channel volume	1	1	47	47	47	47	47
τ resolve time (ns)	50	15	15	15	15	15	15

the relative coincidence efficiency, $(EF)^2$, the number of gamma energies detectable per probe, γF, the number of detector pairs, $N_p F$, and the relative focal volume, VF. Thus the six probe system with commercial collimators is 300 times as sensitive as the two probe system used to scan the phantom with spherical defect of Chapter VII, Part B. Although ^{75}Se is used for comparative purposes, the considerable attenuation in the source is not indicated in detail because of complexity, but it obviously must be taken into account in the final clinical system.

The final comparison of system responses is made in Table 10 for the five configurations and various conditions described above. A review of the most significant initial conditions is given at the beginning of the table. The resultant major parameters γ_1, N_o, S, (S/N_o), PID, VID, and T_t are next given, and last are other useful parameters. The parameter T_t is the total time needed to scan the plane of area, A, with the information densities, PID and VID, indicated. The signal, S, has been computed from the experimental value of 200 cpm obtained using system 1 multiplied by the appropriate sensitivity factor, SF, and the ratio of the isotope concentrations, D. Similarly, the single gamma count rate, γ_1, was obtained from the experimental value for system 1 multipled by factors taking into account the relative probe efficiencies EF, the relative single channel volumes, γ_{rel}, and the relative isotope concentrations. The PIDs for systems 1 and 2 are the experimental values. The latter value was used for all but the last set of scanning parameters in order to be able

TABLE 9

SENSITIVITY PARAMETERS FOR ^{75}Se

Device Configuration:		(1)	(2)	(3), (3')	(4)	(5),(5')
Parameter						
e_1	average probe efficiency (%)	1.5	1.5	0.9	0.9	0.9
N_p	no. of probes	2	2	2	5	6
$N_p e_1$	focal efficiency for one gamma ray (%)	1.5	3.0	1.8	4.5	5.4
$(EF)^2$	relative coincidence efficiency per pair	1.0	1.0	0.37	0.37	0.37
γ_F	no. gamma energies detectible per probe	1	2	2	2	2
$N_p F$	$N_p(N_p-1)/2$, no. pairs	1	1	1	10	15
VF	α_{rel}, relative focal volume	1	1	27	27	27
SF	$(EF)^2(\gamma_F)(N_p F)x$ (VF), total sensitivity factor	1	2	20	200	300

TABLE 10

SYSTEMS COMPARISON

Device Configuration:		(1)	(2)	(3)	(3')	(4)	(5)	(5')
Parameters								
Initial Conditions:								
N_p	no. probes	2	2	2	2	5	6	6
α	focal volume (cm^3)	.08	.08	2.1	2.1	2.1	2.1	2.1
A	scan area (cm^2)	2	100	100	100	100	100	100
D	concentration ($\mu Ci/cm^3$)	7.5	5.0	5.0	1.0	1.0	1.0	0.1
SF	sensitivity ratio	1	2	20	20	200	300	300
Resultant Major Parameters:								
ν_1	single gamma rate per probe $\sim$(EF)x νD (10^3cpm)	140	93	1740	350	350	350	35
N_o	$C_c=2\tau\nu_1^2(N_pF)x$ (γ F), noise (cpm)	32.7	8.7	3040	122	1220	1830	18.3
S	μ_2, signal (cpm)	200	265	2650	530	5300	7950	795
S/N	μ_2/C_c	6.1	30.5	0.9	4.5	4.5	4.5	45
PID	PEC/$d_x d_y$ (counts/cm^2)	10,000	550	550	550	550	550	200
VID	PID/d_z (10^3counts/cm^3)	50	1.4	1.1	1.1	1.1	1.1	0.4

TABLE 10 CONT.

SYSTEMS COMPARISON

Device Configuration:	(1)	(2)	(3)	(3')	(4)	(5)	(5')
Parameters							
T_t $A(PID)/\mu_2$, total scan time (min)	100	205	21	104	10.4	6.9	25
Other Paramters:							
$d_x=d_y$ size of picture element (cm)	0.2	0.4	.2-.5.	.2-.5	.2-.5	.2-.5	.2-.5
PEC $\mu_2 t=(PID)x$ $d_x d_y$, picture element counts	400	90	20-140	20-140	20-140	20-140	8-50
S_{pd} $d_x/t = L_x N_y/T_t$, linear scan speed (cm/min)	0.1	1.2	25-10	5-2	50-20	70-30	20-8
t $T_t/N_x N_y$, time in each location (min)	2.0	0.33	.008-.05	.04-.03	.004-.03	.003-.02	.01-.06

to compare the total scanning times for different systems doing the same scan. It can be seen from the table that the six probe system can scan a 100 cm^2 plane where the source concentration is either 1 or 0.1 μCi/cc in either 6 or 25 minutes with a PID of either 500 or 200 counts/cm^2. This may represent a clinically useful system since concentrations greater than 1 μCi/cc are commonly used in standard ^{99m}Tc liver scanning. Presently, ^{75}Se-selenomethionine used for standard pancreas scanning with PIDs of a few hundred counts/cm^2 collects in the liver at concentrations of about 0.1 μCi/cc.

It appears then that coincident large organ scanning with a presently clinically available radionuclide may be possible using a six probe FCCS system. A prototype of such a system has been constructed. Figures 48 and 49 show the physical appearance of this system and the two probe system respectively.* Scans by this system using ^{75}Se, however, would be of questionable usefulness since the attenuation of the ^{75}Se gamma emissions in tissue would appear to result in scanning times of an hour or more for each plane. If one of the existing more energetic, shorter half-lived isotopes, were employed at the concentration of 1 μCi/cc, FCCS may be clinically useful for large organ scanning as well as for small region scanning.+

The above discussion, however, was meant only as an illustration of how specific system parameter changes may affect the count rate

* The six probe system performance will be reported elsewhere (35).

+ Of the many existing coincident gamma isotopes the most promising appear to be ^{180m}Hf, ^{43}K, ^{82}Br and ^{130}I. A complete discussion of these possibilities will appear elsewhere (36).

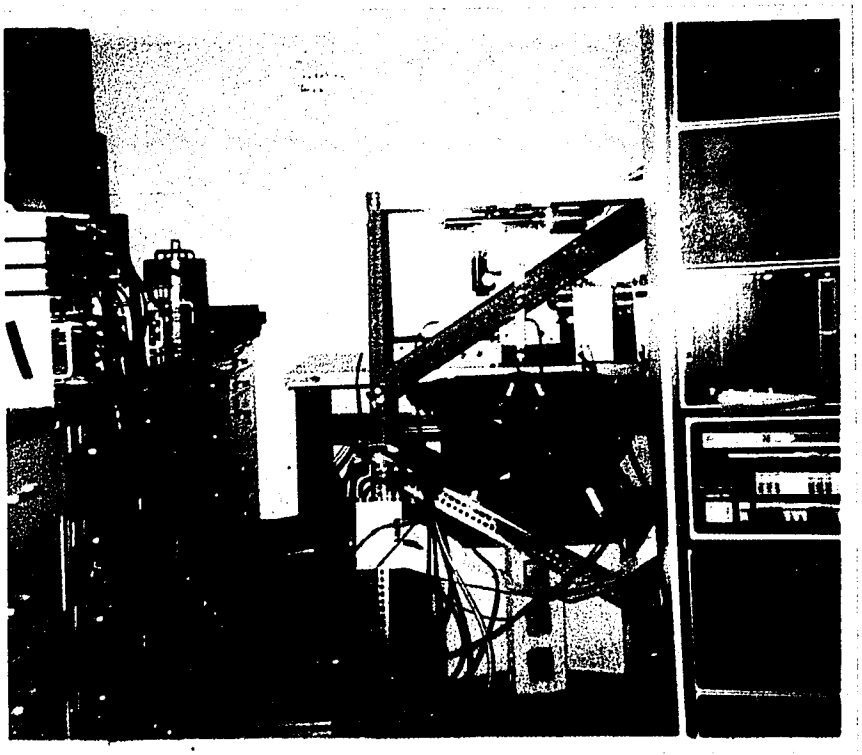

Figure 48. Six probe FCCS system with five probes in place.

Figure 49. Physical appearance of two probe FCCS system.

obtained for a uniform, homogeneous source distribution. The important discussion of the detection probabilities for a specific sized cold or hot lesion in a non-uniform, inhomogeneous clinically relevant medium is of necessity complicated, and is presently under investigation both theoretically and experimentally (39).

C. Conclusions

The goal in this work has been to study the properties of tomographic radioisotope scanning using a coincident gamma ray scanning method (FCCS). It was shown in preliminary work and in the first few phantom scans that multi-millimeter three dimensional spatial resolution could be obtained, and that this high resolution was reasonably well preserved while scanning through considerable thicknesses of tissue equivalent scattering media.

A general theory for evaluating three dimensional scanning systems was devised for analysing the results and parametric formulae for system sensitivity were developed. Also the electronic circuitry needed for more sensitive multi-probe devices (Appendix A) was designed and constructed to provide for the reduced resolving time needed to minimize chance coincidences. In addition, a computer controlled scanner and automatic data acquisition system (Appendix B) was designed and constructed in order to facilitate the study.

It appears that in the near future increasingly useful three dimensional radionuclide scans will become a reality in nuclear medicine, and that, in particular, FCCS may be of unique importance in certain types of three dimensional imaging procedures.

APPENDIX A

COINCIDENCE DETECTION ELECTRONICS

Three methods for detecting coincident events were used. The cross-over, fast-slow leading edge, and fast-slow constant fraction timing technqiues used in this work are diagrammed in Figs. A1, A2 and A3.

For the circuitry of Fig. A1 double delay line amplifier noise limited the resolve time to about 50 ns. Another limitation of the circuit of Fig. A1 is that each detector registers only events in one gamma ray energy peak. In Fig. A2 the resolve time is reduced to 12.9 ns for ^{75}Se; however, the second limitation still remains. In this circuit a standard fast-slow technique is used whereby the anode pulses from the photo-multiplier tubes are used for timing purposes and the dynode pulses are used to evaluate the energy. The output logic pulses from the tunnel diode leading edge discriminators (Chronetics Model 154) could be set to time widths from less than 3 ns to over 50 ns. The resolve time was determined by setting these output widths to the minimum of about 2.5 ns and recording the coincident rate as a function of time delays introduced to the anode pulse cable length by a delay box (Chronetics Model 21). The FWHM of this delay line time spectrum can then be considered the resolve time γ. Such time spectra are shown in Fig. A4 for ^{22}Na and ^{75}Se sources. It can be seen that as expected from photon statistics, the resolve time for the higher energy emitter (511 keV for ^{22}Na), 8.7 ns,is less than for the lower energy emitter

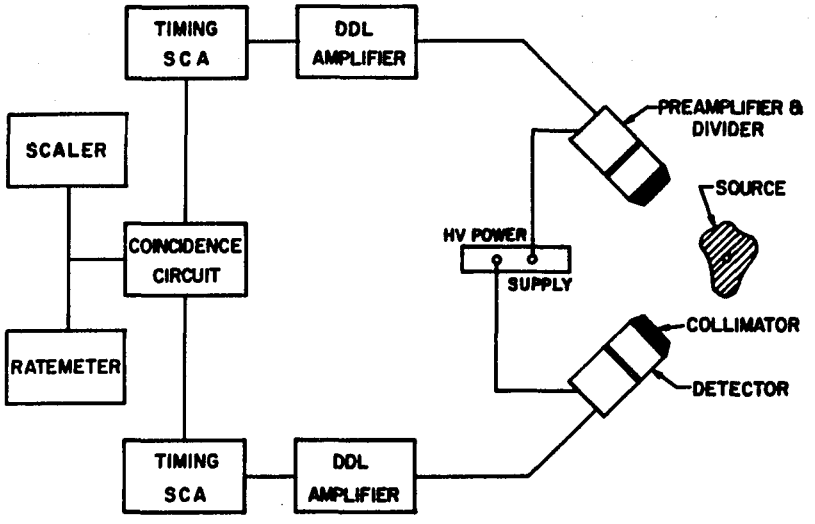

Figure A1. Circuit used in early work using cross-over (CO) timing where each channel can only process one gamma ray energy.

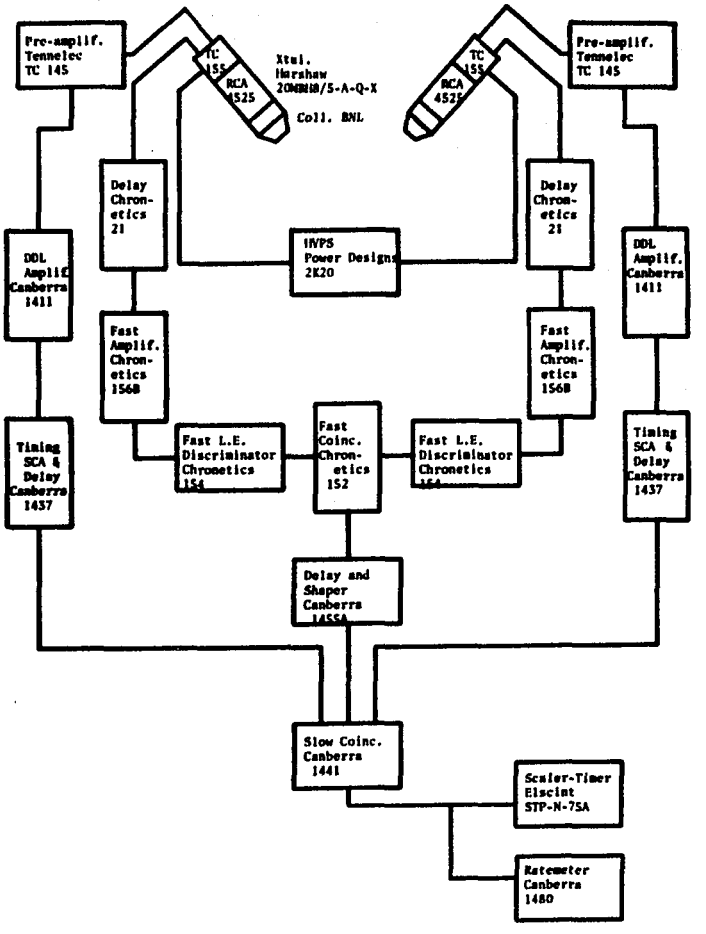

Figure A2. FCCS circuit modified to use a fast-slow leading edge (LE) timing technique where again each channel can only process one gamma ray energy.

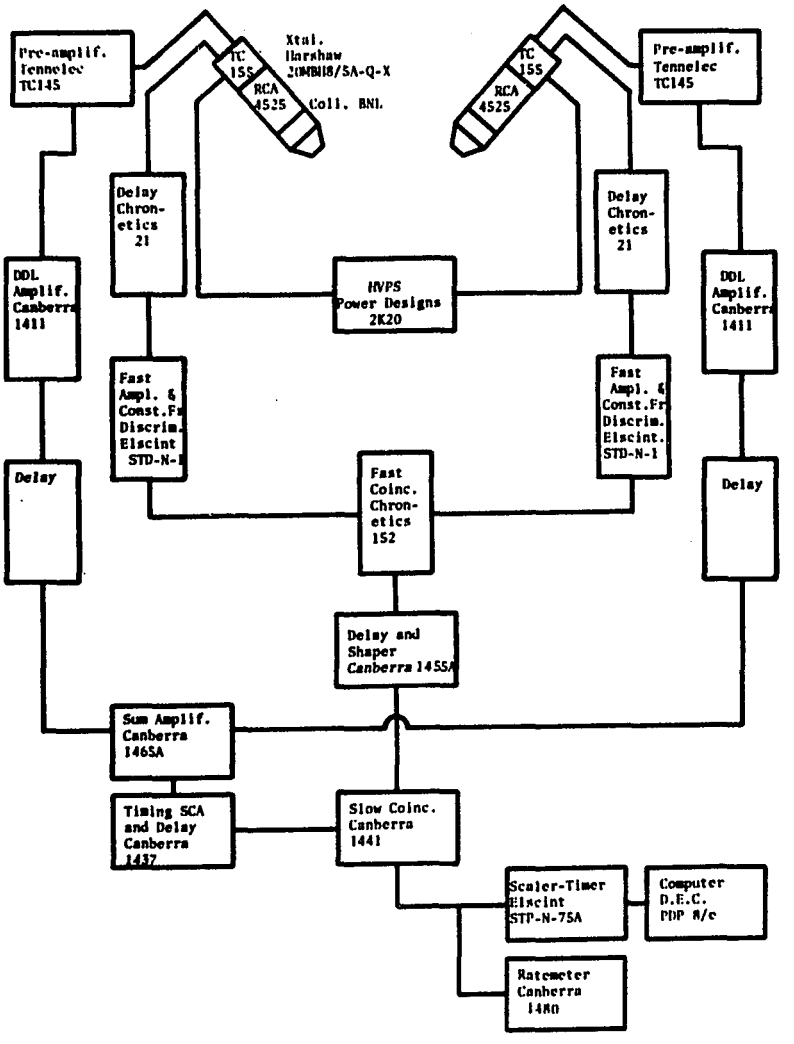

Figure A3. FCCS circuit modified to use a fast-slow constant fraction (CF) timing technique where either channel can process either gamma ray energy.

($\sim$135 and $\sim$265 keV for ^{75}Se), 12.9 ns.

In order to be able to count both energies of ^{75}Se in either detector the leading edge discriminators can not be used. Their dynamic energy range is limited by the time "walk" introduced due to anode pulses of varying heights. Figure A5 demonstrates the increase in resolve time and change in time spectrum shape which occurs when leading edge discriminators are used for both ^{75}Se energy gamma rays. Instead, constant fraction discriminators were substituted and energy selection was done after summing the dynode outputs as is indicated in Fig. A3. Figure A5 also shows the time spectrum obtained from the circuit of Fig. A3 except that the output of the constant fraction discriminators (Elscint Model STD-N-1) was reduced from between 15 and 20 ns to 2.5 ns by placing a leading edge discriminator (Chronetics 154) after the constant fraction discriminator. This was necessary in order to obtain a valid delay line time spectrum. The resolve time for the new circuit of Fig. A3 is now comparable to that of Fig. A3 (see Fig. A6); however, now the sensitivity of the system is doubled.

The circuit of Fig. A3 was the most advanced of those used in the two probe experiments of this work. Although the FWHM of the delay line time spectrum was 15.6 ns for ^{75}Se, the resolve time measured by delaying one anode output about 65 ns and measuring chance coincidences was 17.8 ns. This can be explained by the fact that the output pulse widths from the constant fraction discriminators was probably between 15 and 20 ns. Because of the energy selection in

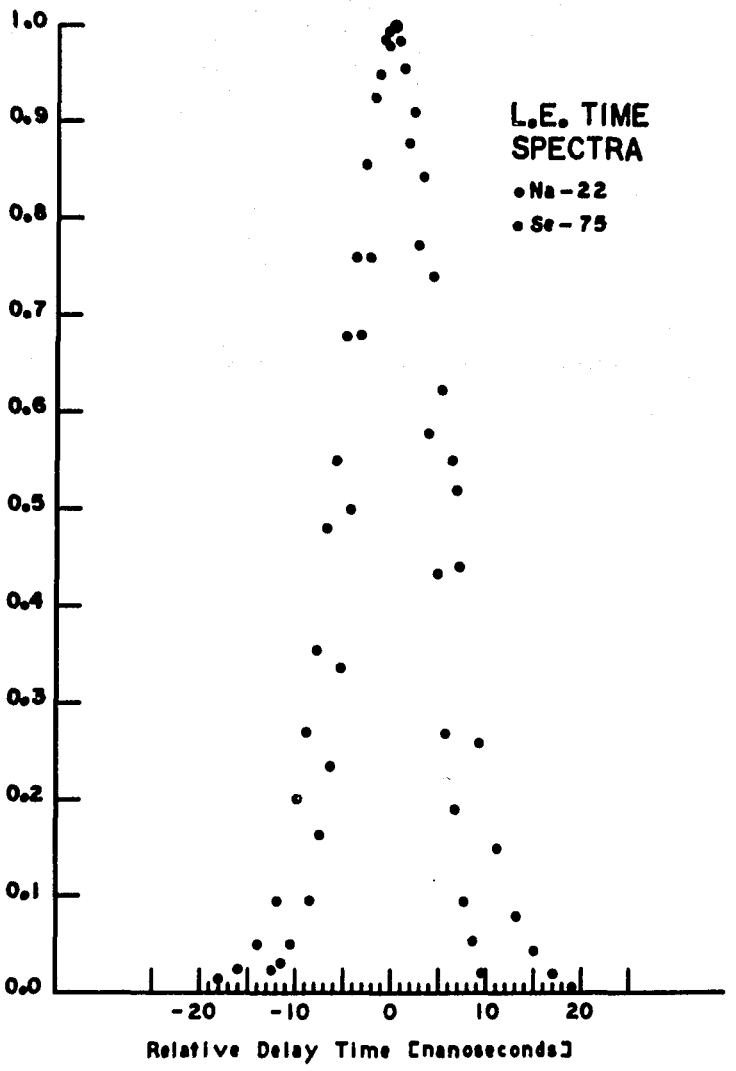

Figure A4. LE technique of Figure A2 using two different isotopes. The higher energy emitter ^{22}Na shows better time resolution.

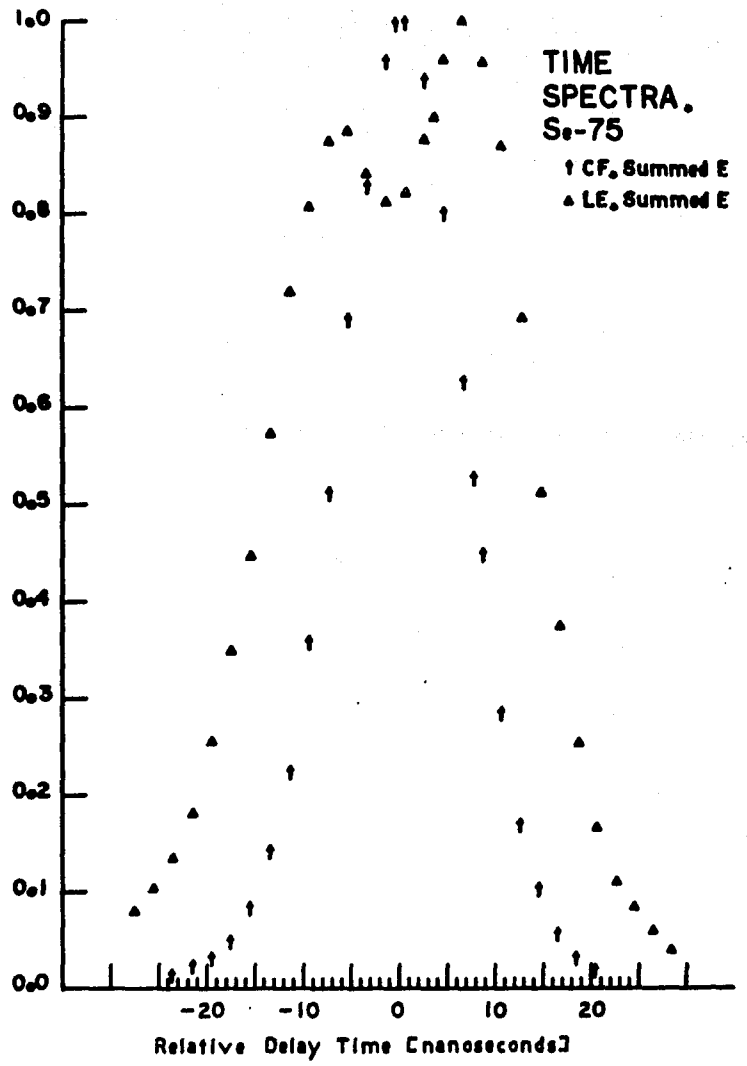

Figure A5. The CF technique of Fig. A3 compared to an LE technique modified from that in Fig. A2 to allow either channel to process either gamma ray. The double peak for the LE technique is due to the time walk which occurs when an LE technique is used over a large dynamic energy range.

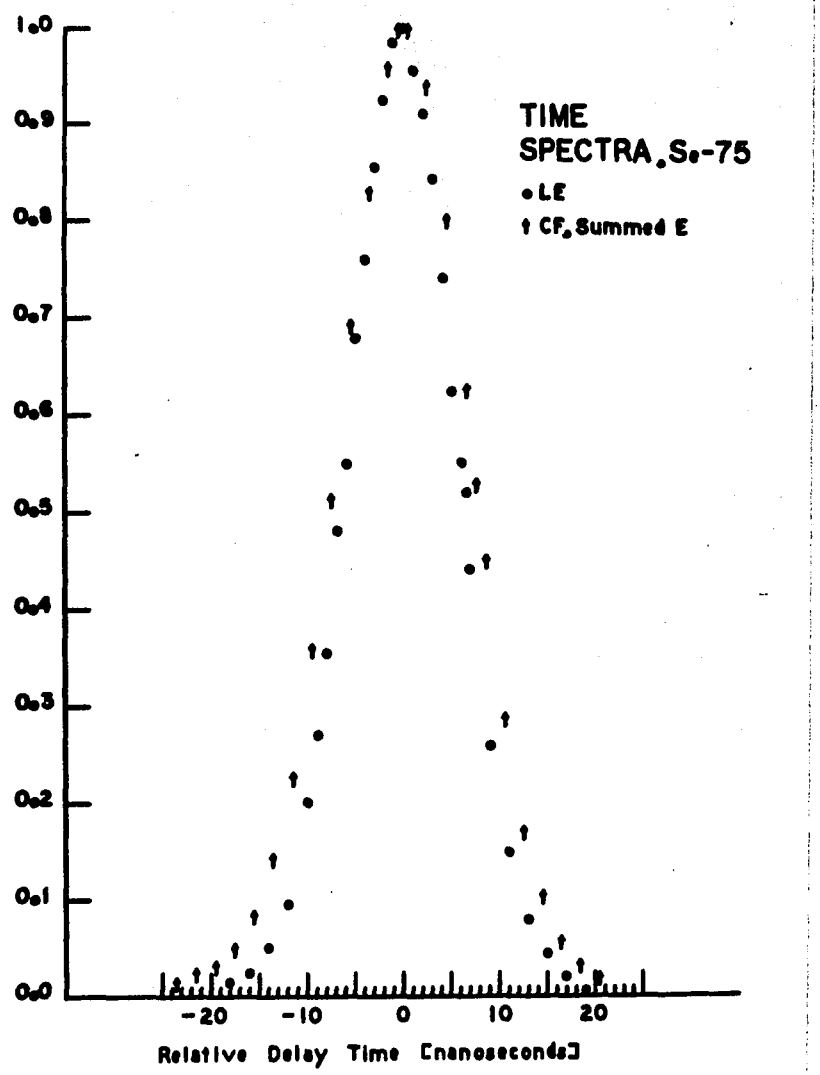

Figure A6. The CF technique of Fig. A3 compared to the LE technique of Fig. A2 where there is a restricted dynamic energy range. The CF circuit is twice as sensitive as the LE circuit without much loss in time resolution.

the circuit of Fig. A3, however, one half of the chance coincidence are counted and thus the effective measured resolve time was actually 8.9 ns. If it were necessary this time could be reduced to half the FWHM of the delay time spectrum for ^{75}Se of 7.8 ns by reducing the constant fraction discriminator output pulse width to 3 ns without appreciably losing true coincidence counts.

In order to expand the numbers of probes in the FCCS system the circuit of Fig. A7 was built where a linear mixer (Ortec-EGG Model AN308-NL) with up to 16 inputs and a tunnel-diode discriminator (Chronetics Model 154) at the output is used as the fast coincidence logic. The resolve time of this circuit is determined by the output pulse width of the constant fraction discriminators just as was the circuit of Fig. A3.

If the slow channel in Fig. A7 should cause coincidence counting losses, a gate can be inserted as indicated in Fig. A8 so that energy determinations are made only when a coincidence event has occurred. However, it has not yet proved necessary to build such a circuit.

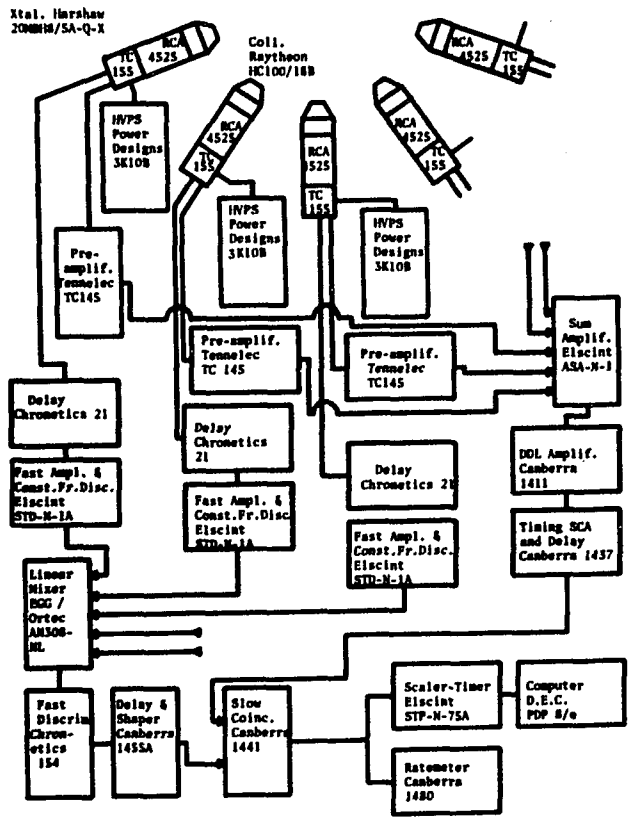

Figure A7. Multi-probe FCCS circuit using CF timing and a linear mixer-discriminator combination as the fast coincidence logic.

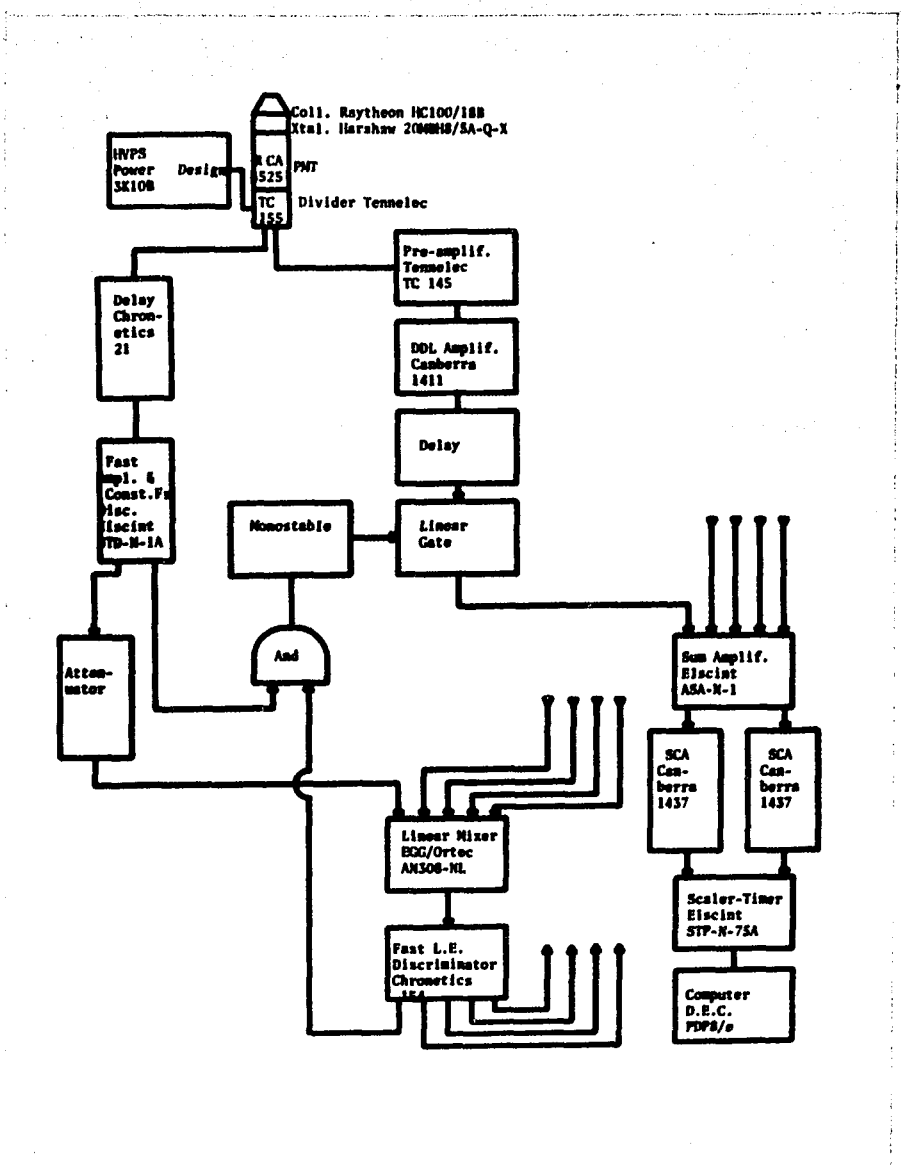

Figure A8. Proposed multi-probe FCCS circuit modification in order to reduce counting losses due to the slow channel.

APPENDIX B

COMPUTERIZED SCANNER

A computerized FCCS system which would scan a phantom and record the data automatically was designed and constructed. The design and construction of this system consisted of five parts:

1. Motorized X-Y traverse.
2. Motor translator to drive the motors, and power supply for the translator.
3. Computer interface to supply the proper pulses to the motor translator and scaler, and to accept data from the scaler and from limit switches.
4. Connector box to distribute the electronic signals properly.
5. Software.

The operation of the system can be described using Fig. B1. The scaler (Elscint STP-N-75A) is set to count for a preset time (or count) using its crystal clock. When the scaler stops counting, its "Gate Out" signal causes a computer interrupt. The computer sends two signals appropriately shaped by the new interface card (D.E.C. Model 1709) to the scaler via the new connector box (Fig. B1) in order to command the scaler to present its data. The two signals are the "Scaler System Inhibit" and the "Scaler Advance In" pulses. After these signals are provided the scaler presents its data (count or time) on a 50 pin panel connector. The data used is 6 decimal digits of 4 bits BCD or 24 lines of data. Two additional new cards

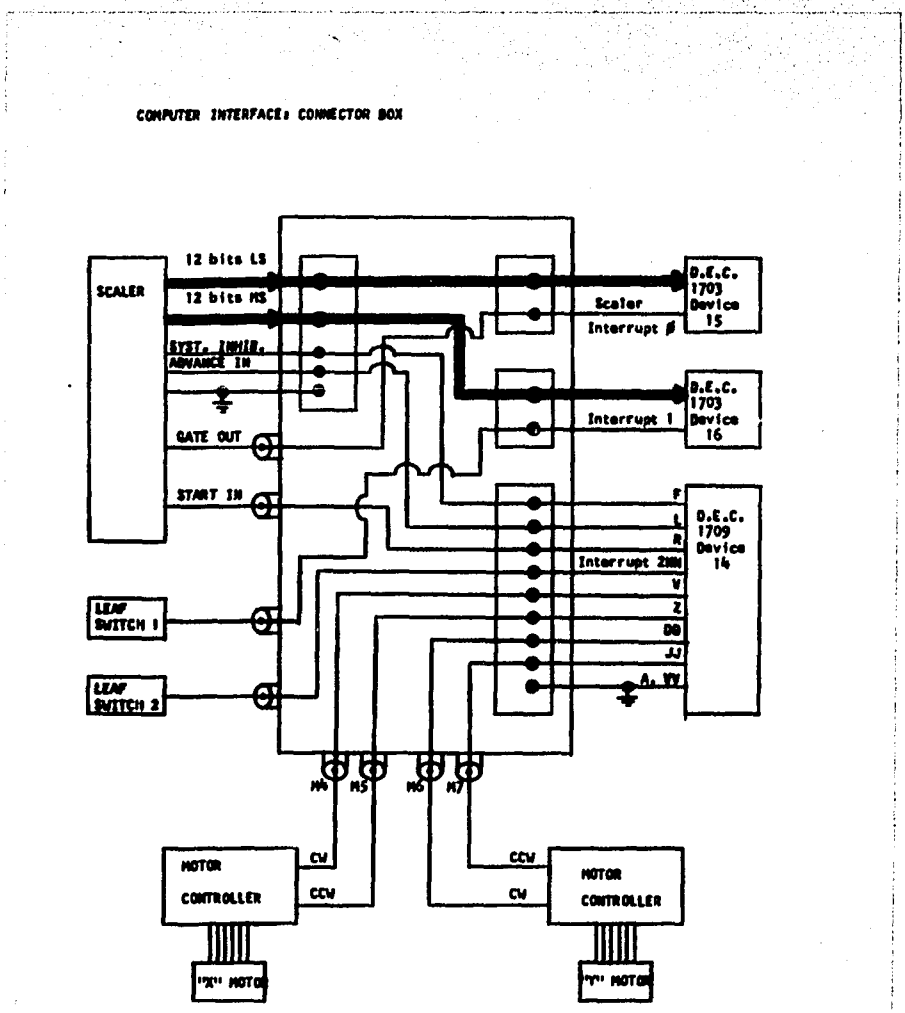

Figure B1. Connector box for interfacing scaler and motors with computer.

in the computer (D.E.C. Model 1703 - Omnibus Input Interface) receive the data from the scaler via the connector box and form two words in core of 12 bits each.

With the data now recorded in core the computer issues commands to move the X-Y traverse to the new position. Four outputs from the Model 1709 Interface Foundation are used to drive the traverse in the +X, -X, +Y, -Y directions. These pulses are fed via the connector box to the two motor translators (one for X, one for Y directions) which in turn supply the large currents required to step the motors. When the correct position is reached the computer sends a 1.5 μs "Start In" pulse to the scaler. While the scaler is counting at the new (X, Y) location, the data recorded in core from the previous location is now printed out as hard copy. When the scaler stops counting according to its preset-stop setting, the entire cycle begins again. In this way a scan of the X-Y plane is made.

1. Motorized X-Y Traverse

Two Superior Electric model M stepping motors were selected to be attached via a universal couple to a manual Spindler and Hoyer precision cross-carriage with 200 mm X-Y displacement (Fig. B2). Two hundred steps per revolution were thus made equivalent to 1 mm displacement.*

* The construction of the motorized traverse was carried out by Mr. P. Zacuto.

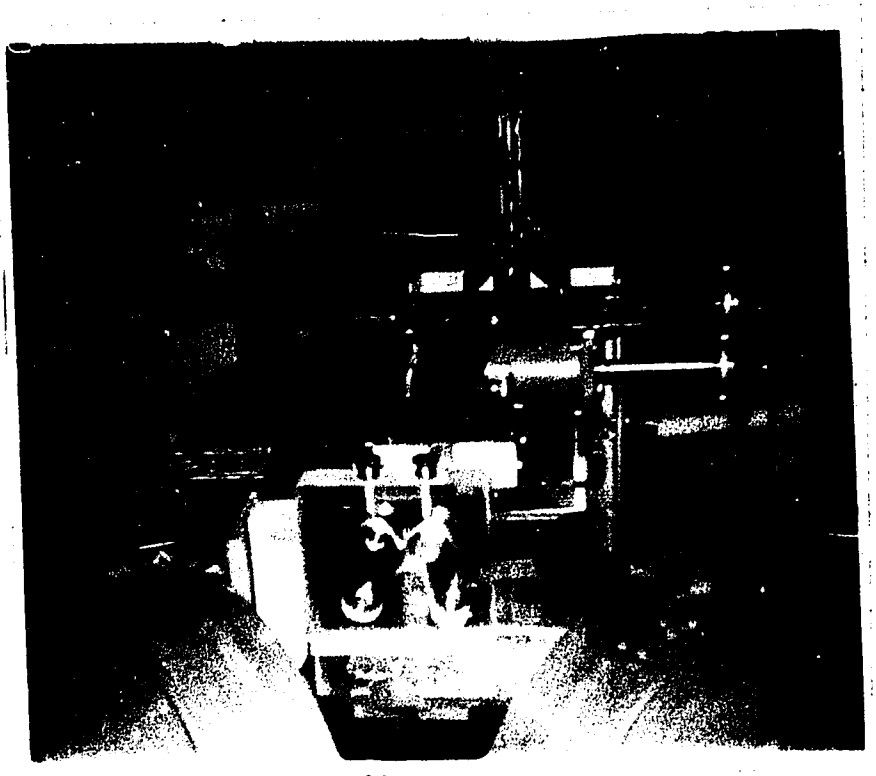

Figure B2. Physical appearance of motorized traverse.

2. Translator and Power Supply

Two box chassis each containing a power supply built out of a Superior Electric T6382 transformer, two full-wave rectifiers and capacitive filters (Fig. B3) provides +12V and -25V D.C. with better than 5% ripple to a Superior Electric Model STM1800CV translator card. The output currents for the stepping motors are provided by an 8 pin Cinch-Jones connector. Elaborate manual switch controls were built in so that the system could be run completely independently of the computer if necessary (See Fig. B3). For computer control two input BNC connectors are provided in each unit for "+" and "-" directions, and a DPST switch bypasses the manual controls.

3. Computer Interface

A D.E.C. Model 1709 Omnibus Interface Foundation module was used along with two Model 1703 Omnibus Input Interface cards. The circuit of Fig. B4 consisting of 6 monostable, 4 operational amplifier, 1 flip-flop and 1 inverter integrated circuits, as well as other indicated components and logic, was built onto the Model 1709 module using wire wrap as well as solder techniques. The four monostable operational amplifier combinations provide the -8 to -10 V, 50 μs pulses required by the motor translator. The flip-flop provides the "Scaler System Inhibit" level and the other two monostables provide the 1.5 μs "Advance In" and "Start In" pulses, all of the latter being TTL compatible.

One part of the hex inverter IC is used for an interrupt

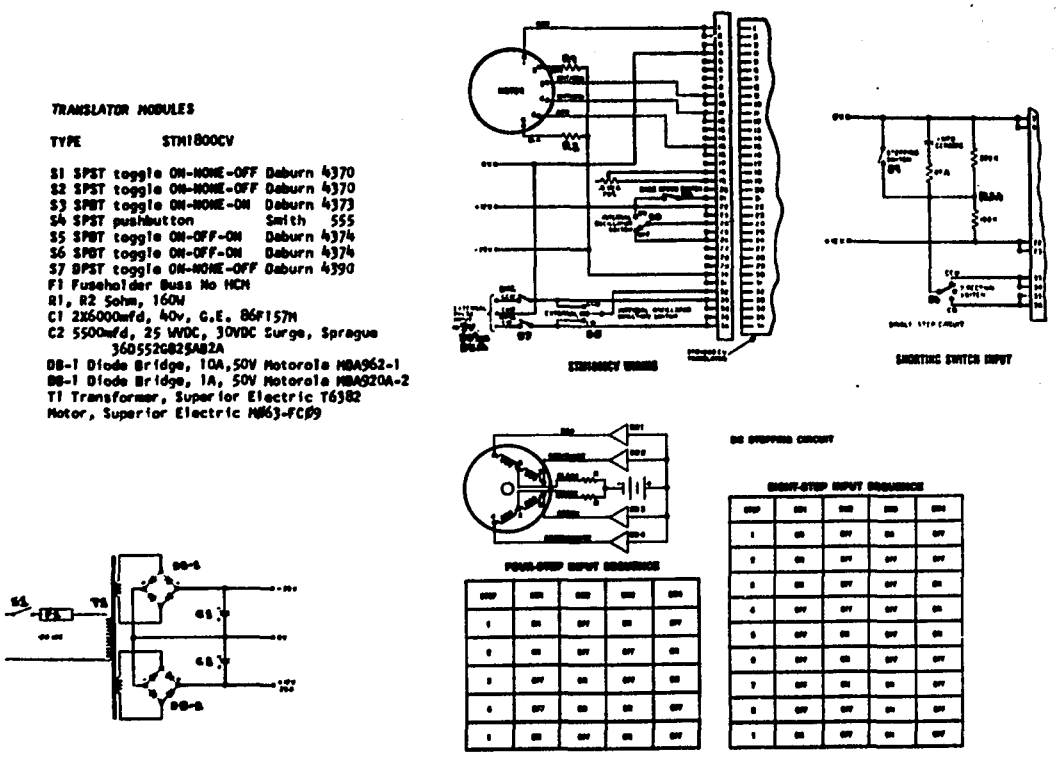

Figure B3. Schematic and parts list for power supply of motor translator module.

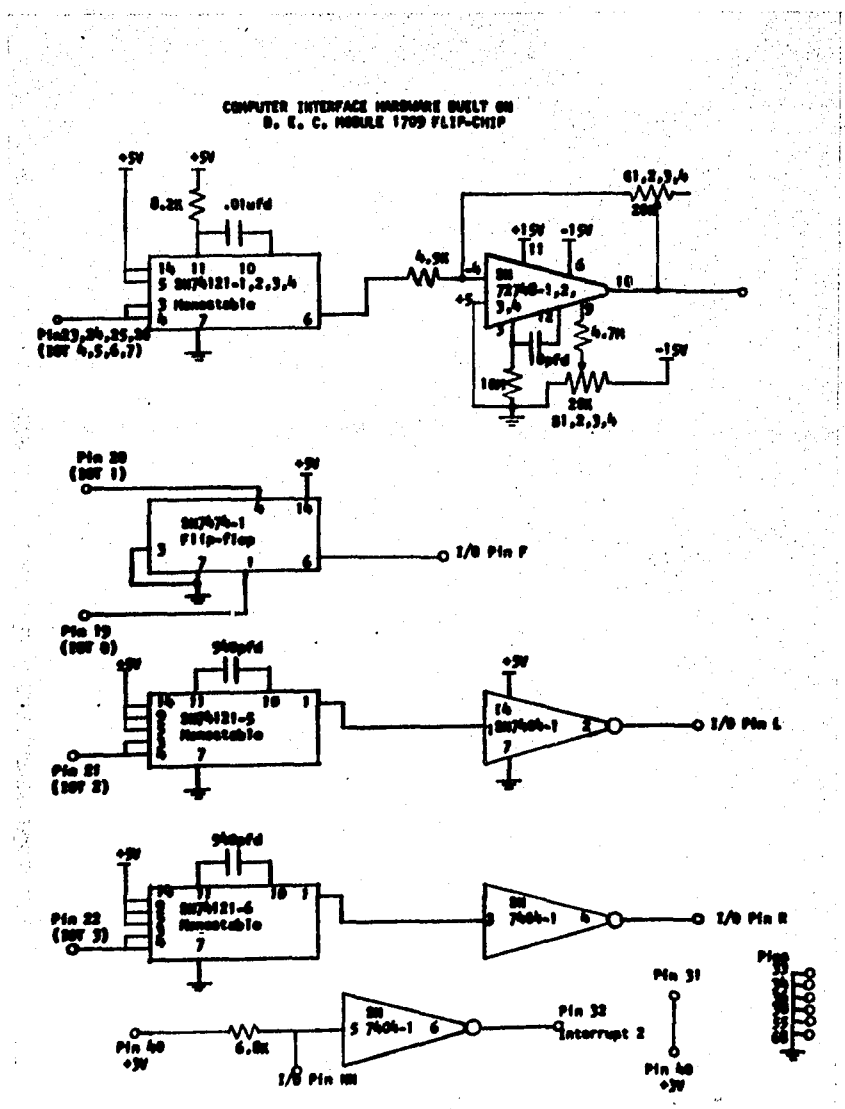

Figure B4. Schematic for computer interface built on a D.E.C. Model 1709 Interface Foundation.

induced by shorting leaf switches used to limit X and Y excursions of the traverse. Table B1 indicates the 18 new I/O commands created by the interface.

4. Connector Box

The connector box of Fig. B1 was built to allow convenient interconnection of the above devices as well as for access to the signals for trouble-shooting.

5. Software

The flow charts of Figs. B5 to B10 show a more detailed outline of the operation of the system. There are 7 subroutines including a program for dialing in a starting position where the scan should begin; a rectilinear scan subroutine; an anti-backlash, fly-back subroutine so that no scalloping will occur; and data read, binary to BCD conversion and print subroutines.*

* The PAL and machine language program was developed and assembled by P. Spetsieris.

TABLE B1

COMPUTER COMMANDS

COMMAND	FUNCTION
6140	Clear Scaler System Inhibit (High)
6141	Set Scaler System Inhibit (Low)
6142	Advance In
6143	Start In
6144	Motor Pulse 4
6145	Motor Pulse 5
6146	Motor Pulse 6
6147	Motor Pulse 7
6150	Disable Interrupt "0"
6151	Enable Interrupt "0"
6152	Clear All Flags, Device 15
6153	Skip If Device 15 Flag Set
6154	Read Data into Device 15
6160	Disable Interrupt "1"
6161	Enable Interrupt "1"
6162	Clear All Flags, Device 16
6163	Skip If Device 16 Flag Set
6164	Read Data into Device 16

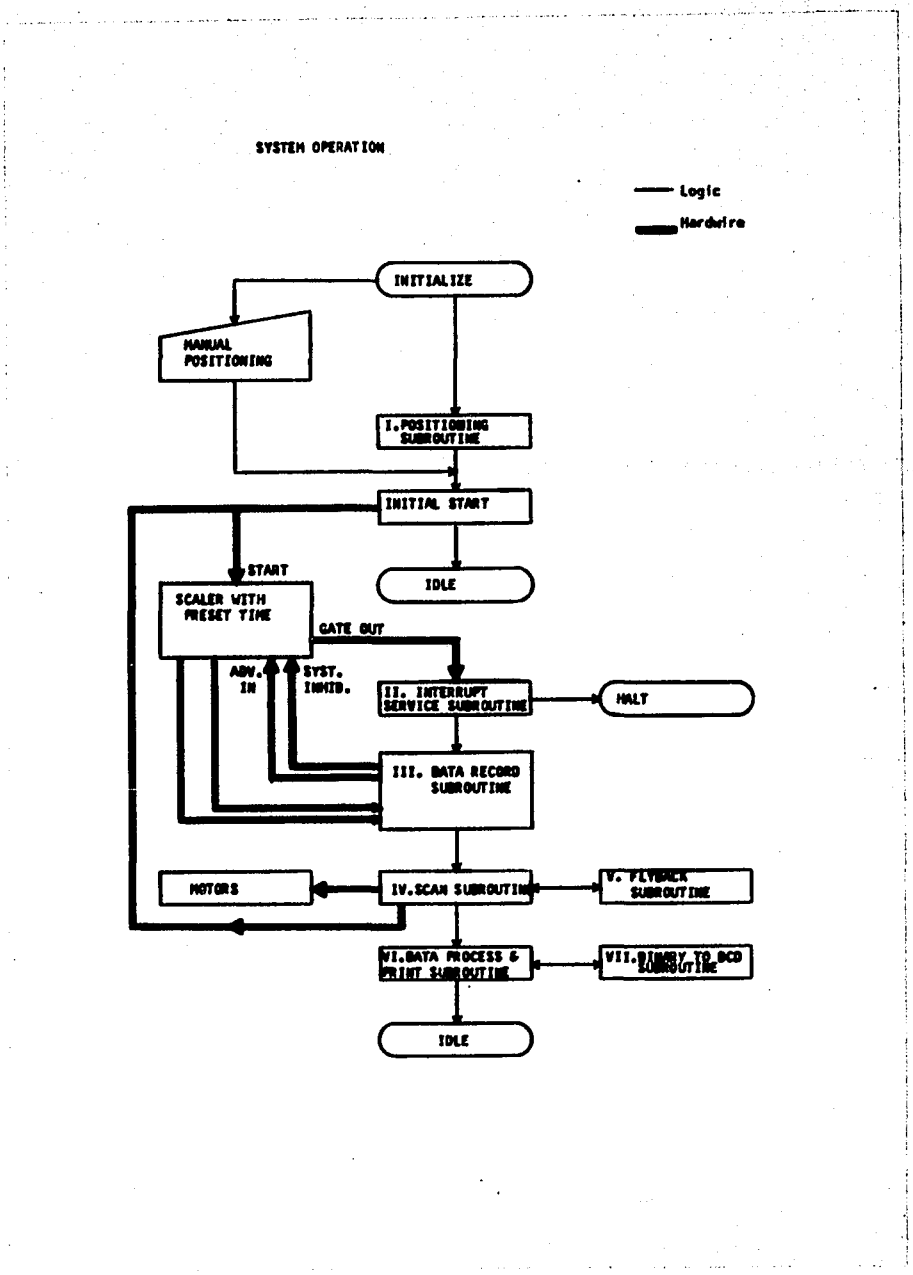

Figure B5. Block diagram of software used to run the computerized scanner.

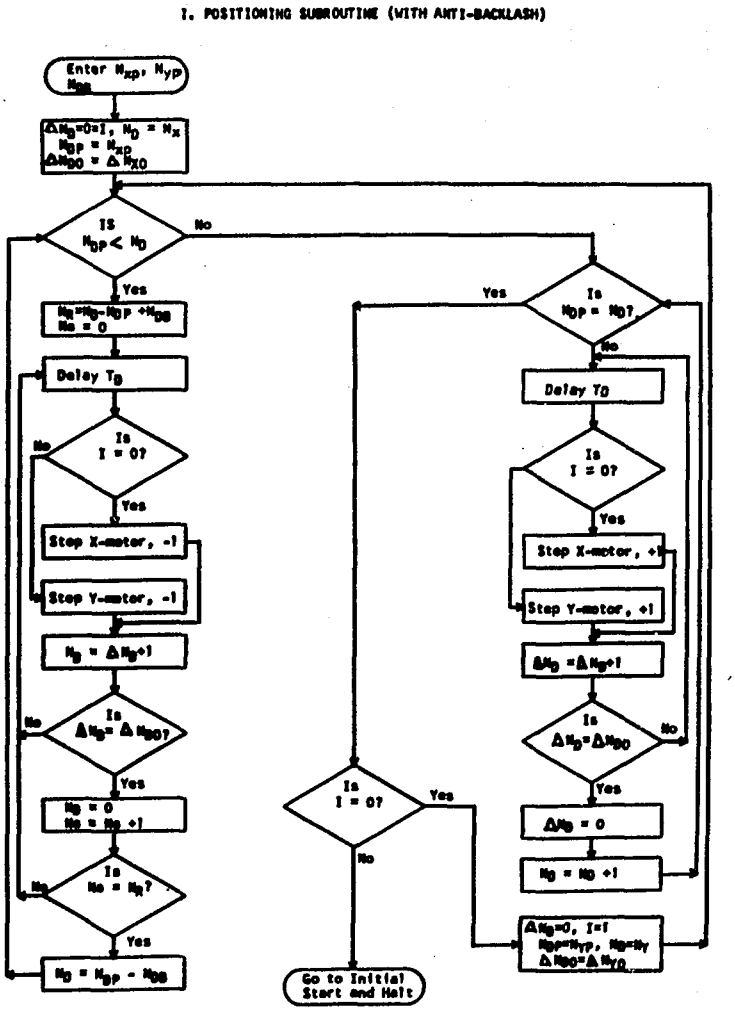

Figure B6. Positioning subroutine.

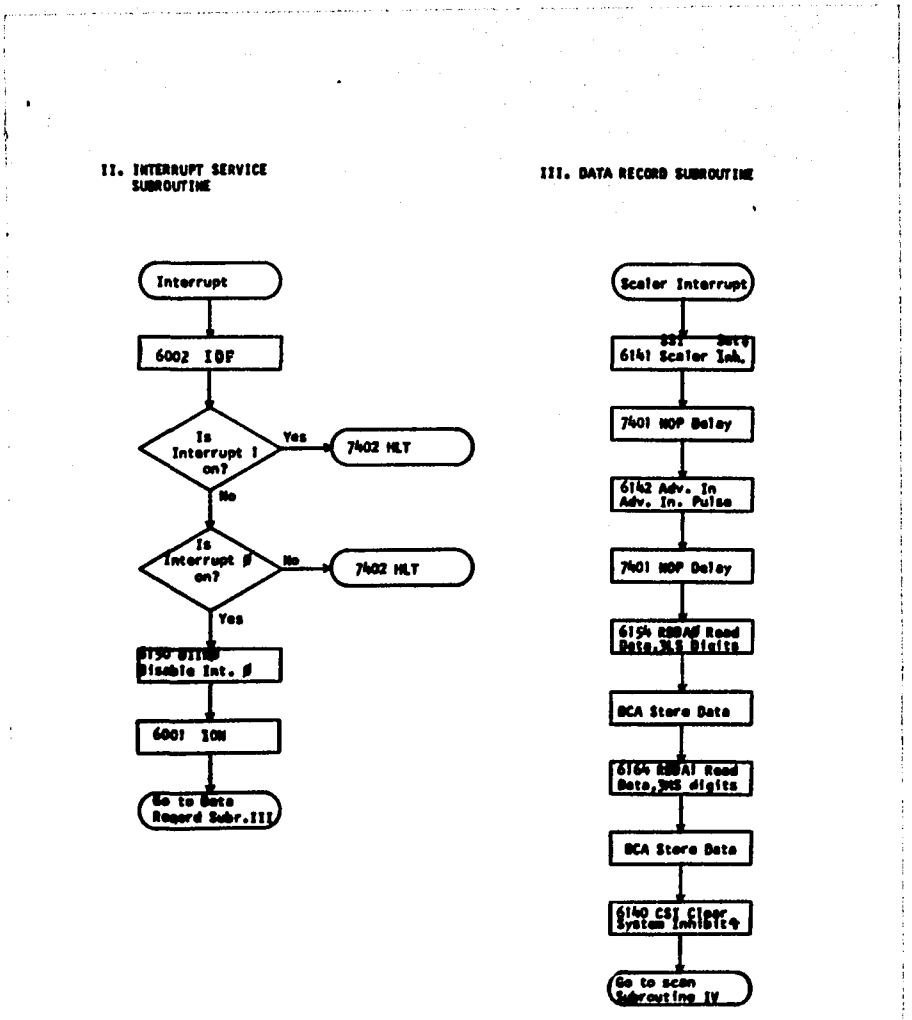

Figure B7. Interrupt service and data record subroutines.

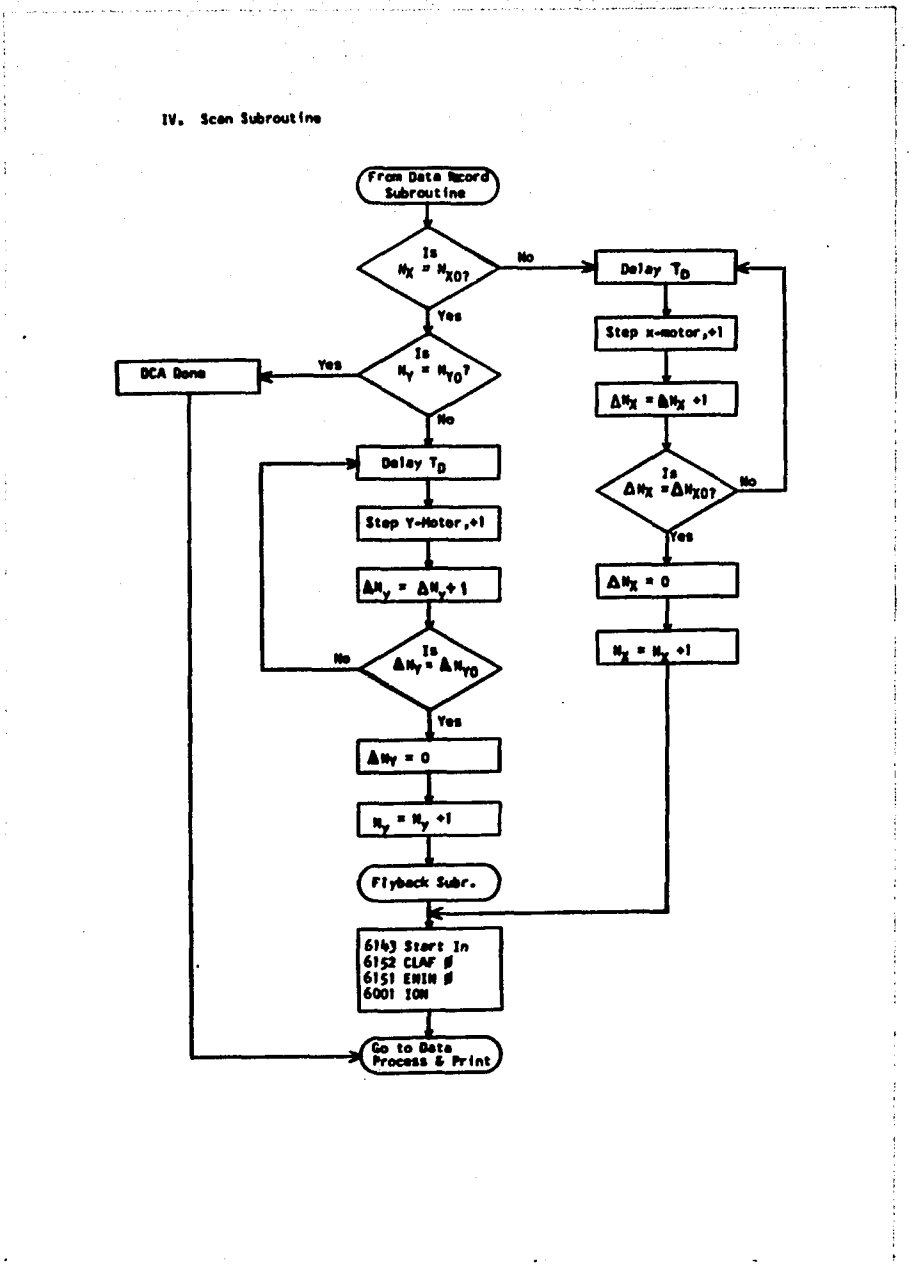

Figure B8. Scan subroutine.

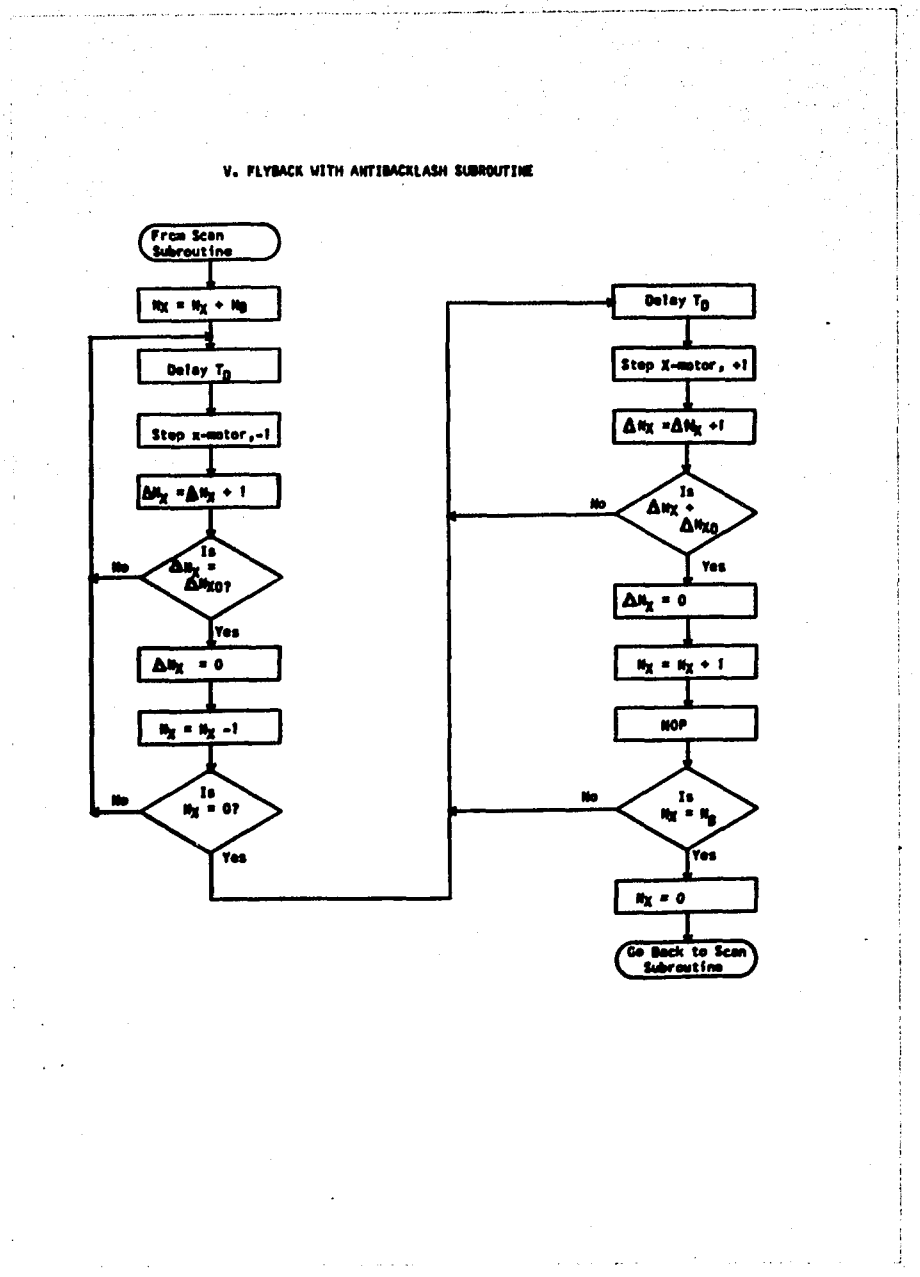

Figure B9. Flyback subroutine.

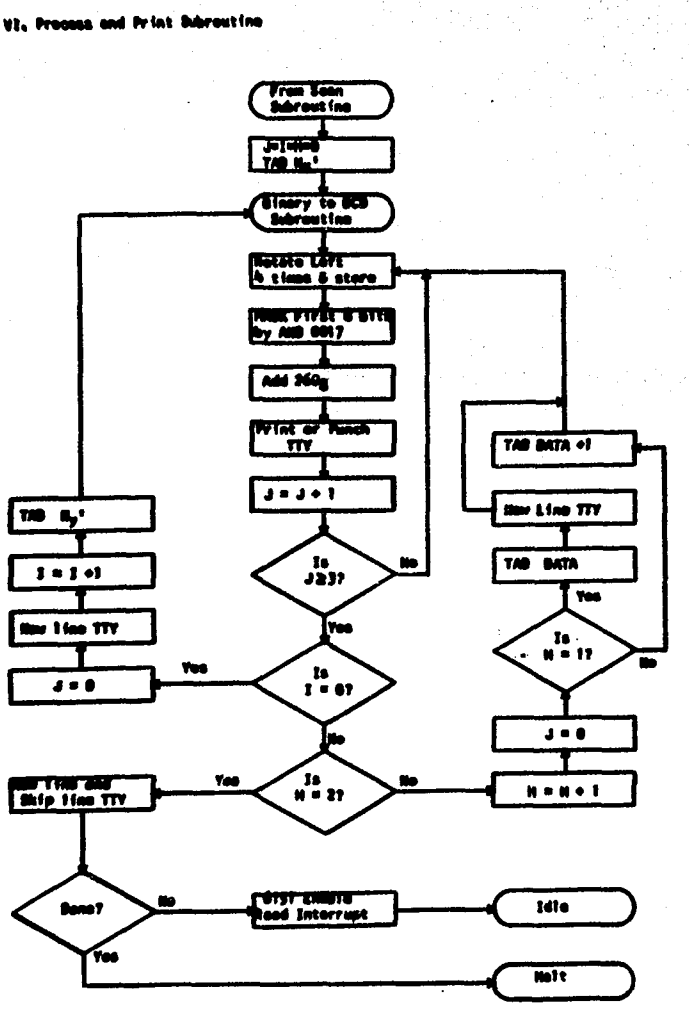

Figure B10. Process and print subroutine.

APPENDIX C

PROOF THAT SEPARABILITY AND ELLIPSOIDAL SYMMETRY IMPLY GAUSSIAN SHAPE

If F is a function of X, Y, and Z, and the dependencies on variables are separable, Eq. (C.1) holds.

$$F(X,Y,Z)=f(X)g(Y)h(Z) \tag{C.1}$$

Furthermore, if ellipsoidal symmetry is assumed then equation (C.2) holds.

$$F(X,Y,Z) = F(aX^2+bY^2+cZ^2);\ a,b,c > 0 \tag{C.2}$$

By differentiating F by X, Y and Z separately in equations (C.1) and (C.2), equations (C.3) result.

$$\begin{aligned} f'gh &= 2aXF' \\ fg'h &= 2bYF' \\ fgh' &= 2cZF' \end{aligned} \tag{C.3}$$

Equations (C.4) follow.

$$\frac{f'}{2aXf} = \frac{g'}{2bYg} = \frac{h'}{2cZh} = A \tag{C.4}$$

In the above equations, A must be a constant since each of the other terms are functions of only one variable. Taking the equations (C.4) separately and integrating, the desired result is proved.

$$\begin{aligned} \ln f &= (aX^2)\ A + \text{Const} \\ \ln g &= (bY^2)\ A + \text{Const} \\ \ln h &= (cZ^2)\ A + \text{Const} \end{aligned} \tag{C.5}$$

$$F(X,Y,Z) = fgh = (\text{Const})\exp\left[(aX^2+bY^2+cZ^2)A\right] \qquad (c.6)$$

APPENDIX D

CIRCULAR SYMMETRY OF TWO PROBE SYSTEM PSF NEAR FOCAL POINT IN Y-Z PLANES

Consider the two probe FCCS system in Fig. D1 where the two probe axes Q and P are at right angles. If $f_Q(p,q)$ and $f_P(p,q)$ are the single gamma PSFs of the Q and P probes respectively, then let us assume (1) the probes are identical (equations (D1) to (D3) and Eq. (D6)), (2) the single gamma PSFs near the focal point do not change much in a direction parallel to the probe axes (equations (D4) and (D5)), (3) the slopes of the PSFs as functions of transverse distances are zero (Eq. (D7)).

$$f_o \equiv f_Q(0,0) = f_P(0,0) \tag{D1}$$

$$f_o' \equiv f_Q'(0,0) = f_P'(0,0) \tag{D2}$$

$$f_o'' \equiv f_Q''(0,0) = f_P''(0,0) \tag{D3}$$

$$f_Q(p,q) = f_q(p,0) \tag{D4}$$

$$f_p(p,q) = f_p(0,q) \tag{D5}$$

If $p = q = x$,

$$f_Q(x,0) = f_p(0,x). \tag{D6}$$

$$f_o' = 0 \tag{D7}$$

The coincident gamma PSF, $F(p,q)$, is the product of the single gamma PSFs of the two probes.

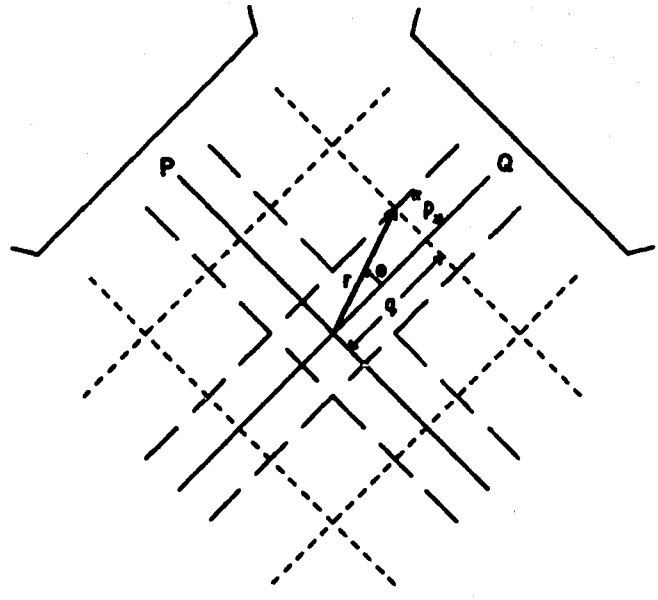

Figure D1. Single gamma isoresponse curves for two probes whose axes are confocal and perpendicular.

$$F(p,q) \equiv f_Q(p,q)\ f_p(p,q) \tag{D8}$$

If f_Q and f_p are expanded around the focal point Eq. (D9) results using equations (D4) and (D5).

$$F(p,q) = \left[f_Q(0,0) + qf'_Q(0,0) + \tfrac{1}{2}q^2 f''_Q(0,0) + \ldots\right] \times \left[f_p(0,0) + pf'_p(0,0) + \tfrac{1}{2}p^2 f''_p(0,0) + \ldots\right] \tag{D9}$$

Using equations (D1), (D2), (D3), and (D4) and neglecting third and higher order terms Eq. (D10) results.

$$F(p,q) = (f_o)^2 + (q + p)(f_o f'_o) + qp(f'_o)^2 + \tfrac{1}{2}(p^2 + q^2) \times f_o f''_o = f_o{}^2 + \tfrac{1}{2}(p^2 + q^2)(f_o f''_o) \tag{D10}$$

Changing to cylindrical coordinates and using $r^2 = q^2 + p^2$, Eq. (D11) results showing the circular symmetry of the coincident gamma PSF.

$$F(\theta,r) = f_o{}^2 + \tfrac{1}{2}(f_o f''_o)r^2 \tag{D11}$$

REFERENCES

1. Hart, H.E., Warshaw, B. and Stoller, H.I., IEEE Trans. on Bio. Med. Eng. BME-14,No. 2, pp. 96-102, April, 1967.

2. Beck, R.N., Zimmer, L.T., Charleston, D.B., Harper, P.V. and Hoffer, P.B., Advances in Fundamental aspects of imaging systems and techniques, to be published.

3. Beck, R.N., A theory of radioisotope scanning systems. Medical Radioisotope Scanning, IAEA, Vienna, I, pp. 35-56, 1964.

4. Beck, R.N. and Harper, P.V., Criteria for comparing radioisotope imaging systems, Chap.30 , pp. 348-384, in Fundamental Problems in Scanning, editors, Gottschalk, A. and Beck, R.N., Charles C. Thomas, Springfield, Illinois, 1968.

5. Beck, R.N., et al, Effects of scattered radiation on scintillation detector response, Medical Radioisotope Scintigraphy, IAEA, Vienna, I, pp. 595-616, 1969.

6. Rudin, S., Bardfeld, P.A. and Hart, H.E., Use of magnifying multihole collimators in the gamma-ray camera system, J. Nucl. Med. 12, pp. 831-834, December 1971.

7. Dewey, W.C. and Sinclair, W.K., Int. J. Appl. Radiation and Isotopes, 10, p. 1, 1961.

8. James, A.E. et al, Clinical experience in tomographic imaging with a Tomocamera, chap. 20, pp. 206-218 and Goldsmith, S.J., Clinical artifacts encountered using circular tomography, Chap. 22, pp. 229-233, both in Tomographic Imaging in Nuclear Medicine, editor, Freedman, G.S., Soc. Nucl. Med., New York, 1973.

9. Anger, H.O., Multiplane tomographic scanner, Chap. 1, pp. 2-15, in Tomographic imaging in nuclear medicine, editor, Freedman, G.S., Soc. Nucl. Med., New York, 1973.

10. Rudin, S., Rider, K.L. and Hart, H.E., Gamma camera tomographic magnifying collimator systems, Chap. 8, pp. 84-100, in Tomographic Imaging in Nuclear Medicine, editor, Freedman, G.S., Soc. Nucl. Med., New York, 1973.

11. Barrett, H.H., DeMeester, G.D., Wilson, D.T., and Farmelant, M.H., Tomographic imaging with a fresnel zone plate system, Chap. 10, pp. 106-120, in Tomographic Imaging in Nuclear Medicine, Soc. Nucl. Med., New York, 1973.

12. Budinger, T.F. and Gullberg, G.T., Three-dimensional reconstruction in nuclear medicine by iterative least-squares and fourier transform techniques, Lawrence Berkeley Laboratory Report No. LBL-2146, University of California, Berkeley, Calif.

13. Kuhl, D.E., Edwards, R.Q. and Ricci, A., Transverse section scanning at the University of Pennsylvania, Chap. 2, pp. 19-26, in Tomographic Imaging in Nuclear Medicine, editor, Freedman, G.S., Soc. Nucl. Med., New York, 1973.

14. Patton, J.A., Brill, A.B. and King, P.H., Transverse section brain scanning with a multicrystal cylindrical imaging device, Chap. 2, pp. 28-42, in Tomographic Imaging in Nuclear Medicine, editor, Freedman, G.S., Soc. Nucl. Med., New York, 1973.

15. Hounsfield, G.N., Computerized transverse axial scanning (tomography): part I, description of system, Brit. J. Rad. 46,No. 552, pp. 1016-1022, December 1973.

16. Cho, Z.H., General views on 3-D image reconstruction and computerized transverse axial tomography, IEEE Trans. on Nucl. Sci., No. 3, vol. NS-21, pp. 44-71, June 1974.

17. Brownell, G.L. and Burnham, C.A., Recent developments in positron scintigraphy, Chap. 4, pp. 135-159, in Instrumentation in Nuclear Medicine,volume 2, editors, Hine, G.J. and Sorenson, J.A., Academic Press, New York, 1974.

18. Chesler, D.A., Positron tomography and three-dimensional reconstruction techniques, Chap. 16, pp. 176-183, in Tomographic imaging in nuclear medicine, editor, Freedman, G.S., Society of Nuclear Medicine, New York, 1973.

19. Chesler, D.A., Hales, C., Hnatowich, D.J. and Hopp, B., Three dimensional reconstruction of lung perfusion image with positron detection, J. Nucl. Med., 16, No. 1, pp. 80-82, January 1975.

20. Ter-Pogossian, M.M., et al, A positron emission transaxial tomograph for nuclear imaging (PETT), Radiol. 114, pp. 89-98, 1975.

21. Phelps, M.E., et al, Application of annihilation coincidence detection to transaxial reconstruction tomography, J.Nucl.Med. 16, pp. 210-224, March 1975.

22. Llacer, J. and Cho, Z.H., Preliminary study of a Ge three dimensional camera for positron emitting radioisotopes, IEEE Trans. on Nucl. Sci, NS-20, No. 1,pp. 282-293, February 1973.

23. Alberi, J.L., Kraner, H.W., Bradley-Moore, P. and Atkins, H.L., Transmission scanning II, IEEE Trans. on Nucl. Sci., NS-21, No. 1, pp. 635-644, February 1973.

24. Hoffer, P.B., Bekerman, C., Stark, V. and Peck, T., Excitation thyroid laminography: theoretical and practical considerations, chap. 5, pp. 57-65, in Tomographic Imaging in Nuclear Medicine, editor, Freedman,G.S., Soc. Nucl. Med., New York, 1973.

25. Hart, H.E. Focusing collimator coincidence scanning, Radiology, 84, No. 1, p. 126, January 1965.

26. Schmitz-Feuerhake, I., Studies on three-dimensional scintigraphy with gamma-gamma coincidences, Phys. Med. Biol. 15, No. 4, pp. 649-656, October 1970.

27. Monahan, W.G. and Powell, M.D., Three-dimensional imaging of radionuclide distributions by gamma-gamma coincidence detection, Chap. 15, pp. 165-174, in Tomographic Imaging in Nuclear Medicine, editor, Freedman, G.S., Soc. Nucl. Med., New York, 1973.

28. Hart, H.E. Comparative resolution of single gamma counting and coincidence counting in focusing collimator scanning systems, Trans. N.Y. Acad. of Sci. Series II, Vol. 30, No. 4, pp. 580-599, 1968.

29. Hart, H.E., Warshaw, B. unpublished work, 1968.

30. Hart, H.E. and Rudin, S. Three dimensional imaging of multi-millimeter sized cold lesions by focusing collimator coincidence scanning (FCCS), submitted for publication.

31. Dillman, L.T., Radionuclide decay schemes and nuclear parameters for use in radiation dose estimation, J. Nucl. Med. Suppl. No. 2, MIRD Pamphlet No. 4, 1969, p. 20.

32. Richards, P., Atkins, H.L., A collimator system for scanning at low energies, J. Nucl. Med. 8, pp. 142-152, February 1967.

33. Miraldi, F. and DiChiro, G., Tomographic techniques in radioisotope imaging with a proposal of a new device: the tomoscanner, Radiology, 94, pp. 513-521, March 1970.

34. Muehllehner, G. and Hashmi, Z., Quantification of the depth effect of tomographic and section imaging devices, Phys. Med. Biol. 17, No. 2, pp. 251-260, 1972.

35. Hart, H.E., Rudin, S. and Zacuto, P., to be submitted for publication.

36. Hart, H.E., et al, to be submitted for publication.

37. Beck, R.N., Current status of diagnostic counting and imaging techniques used in nuclear medicine: a sketch, IEEE Trans. on Nucl. Sci., NS-21, No. 2, pp. 15-32, April 1974.

38. Gottschalk, A. and Beck, R.N., editors, Fundamental Problems in Scanning, Charles C. Thomas, Springfield, Illinois, 1968.

39. Zacuto, P., et al, work in progress.